Deriving Properties of Magnetic Fields in Solar Photosphere

Maria D. Kazachenko

University of Colorado, Boulder — National Solar Observatory

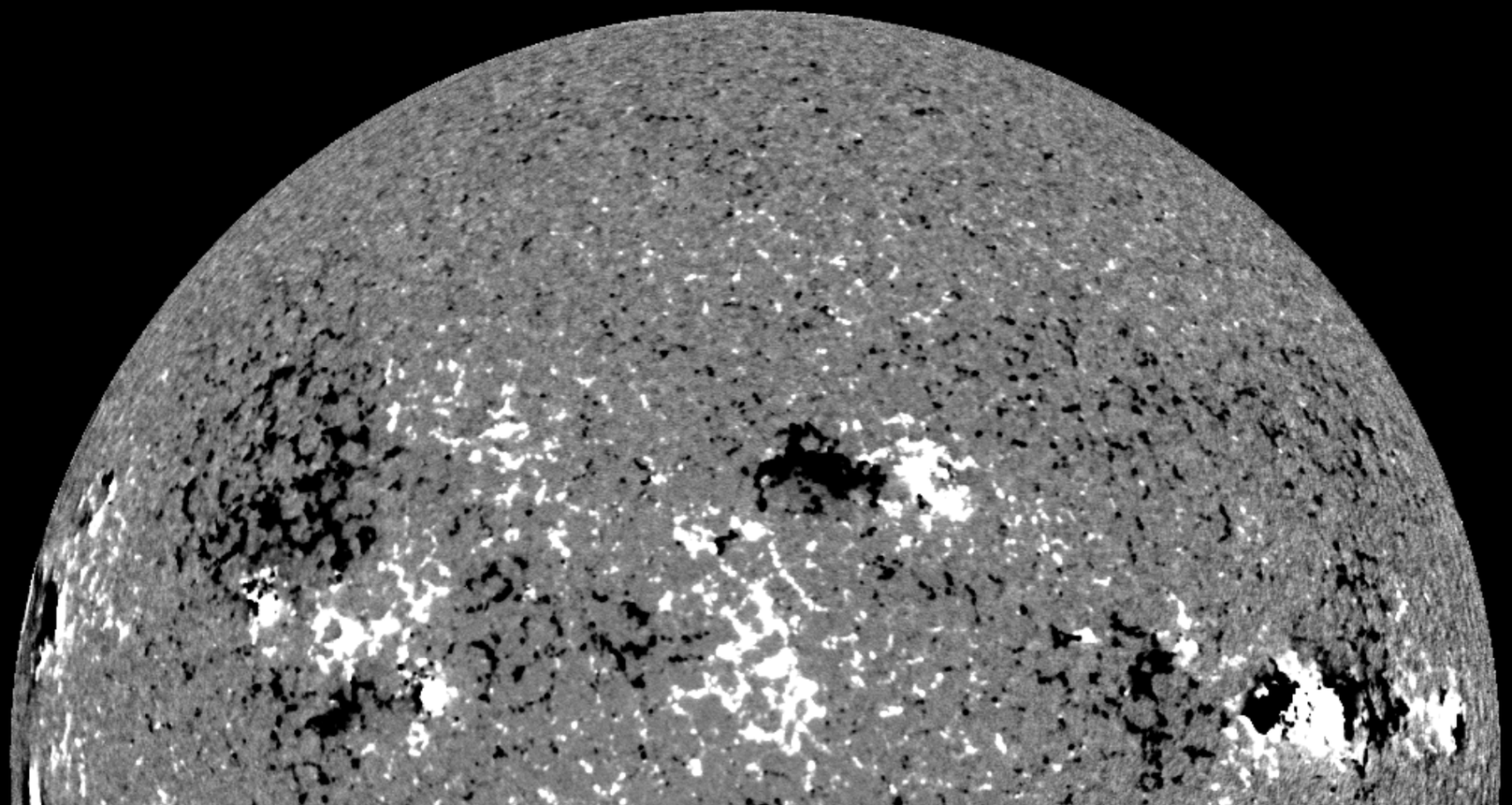

Photosphere BLOS from HMI/SDO

COLLAGE, April 7 2020

Last time: we reviewed some early electric/velocity field inversion methods: tracking and inductive.

- ☆ Non-inductive or **Tracking approaches to find V**: e.g. Local Correlation Tracking (LCT, November & Simon 1988), Fourier Local Correlation Tracking (FLCT, Fisher & Welsch 2008).

- ☆ **Inductive methods** that implement some form of induction equation: e.g. Minimum energy fit (MEF, Longcope 2004), DAVE (Schuck 2006),

$$\frac{\partial \boldsymbol{B}}{\partial t} = -(\nabla \times c\boldsymbol{E}),$$

- ☆ Comparison of early methods using MHD simulation output: *Welsch et al. 2007.*

  - ☆ Horizontal velocity: all methods did poorly, IM, FLCT, and MEF performed similarly; DAVE did slightly better;

  - ☆ Electric fields: DAVE, FLCT, ILCT, MEF did OK.

  - ☆ Energy and helicity fluxes: MEF was the best; could be because it is most suitable physically to ANMHD test case.

Today: we will go over some latest methods to derive electric fields and will look at some recent examples how **B** could help us learn new things about the Sun

Inspired by availability of routine B measurements

- DAVE4VM (Schuck 2008)
- PDFI (Kazachenko et al. 2014, Fisher et al. 2020)
- Non physics-based approaches: Machine-learning methods
- Show examples of how we could use **B** to learn about solar activity

DAVE4VM: DAVE for vector magnetograms

- DAVE4VM (Schuck 2008): modified version of previously discussed Differential Affine Velocity Estimator (DAVE, Schuck 2006);
  - Main advantage: DAVE only uses Bz; DAVE4VM uses Bh and Bz. Jz!
  - The error metric

$$\begin{aligned} C_{\mathrm{SSD}} = \int dt\, dx^2 w(\boldsymbol{x}-\boldsymbol{x},\ t-\tau)\{&\partial_t B_z(\boldsymbol{x},t) \\ &+ \nabla_h \cdot [B_z(\boldsymbol{x},t)\boldsymbol{v}_h(\boldsymbol{P},\boldsymbol{x}-\boldsymbol{\chi}) \\ &- v_z(\boldsymbol{P},\boldsymbol{x}-\boldsymbol{\chi})\boldsymbol{B}_h(\boldsymbol{x},t)]\}^2, \\ = \boldsymbol{\eta}\cdot\langle \mathbf{S}\rangle \cdot \boldsymbol{\eta} & \end{aligned}$$

  - Solution for **P** is derived using least squares solution to minimize the error metric. Final V_h and V_z satisfy $(\ldots)_z$ component of the induction equation.
  - Main disadvantage: approximates induction equation with Least Sq.

PDFI Electric Field Inversion Method

PDFI method is based on Poloidal-Toroidal Decomposition (PTD)

Fisher et al. 2012,

$$\overbrace{-c\nabla\times\mathbf{E}=\dot{\mathbf{B}}}^{\text{Faraday's Law}}=\underbrace{\nabla\times\nabla\times\dot{\mathcal{B}}\hat{\mathbf{z}}}_{\text{poloidal}}+\underbrace{\nabla\times\dot{\mathcal{J}}\hat{\mathbf{z}}}_{\text{toroidal}}=\underbrace{\nabla_h\frac{\partial\dot{\mathcal{B}}}{\partial z}+\nabla\times\dot{\mathcal{J}}\hat{\mathbf{z}}}_{\text{horizontal}}-\underbrace{\nabla_h^2\dot{\mathcal{B}}}_{\text{vertical}}\ \mathbf{z}.$$

Uncurling Faraday's law we get

$$c\mathbf{E}=-\nabla\times\dot{\mathcal{B}}\hat{\mathbf{z}}-\dot{\mathcal{J}}\hat{\mathbf{z}}-\nabla\psi=c\mathbf{E}^P-\nabla\psi=\underbrace{cE^P}_{PTD(inductive)\ solution}+\underbrace{\underbrace{cE_x^{Doppler}}_{Doppler\ included}+\underbrace{cE_h^{FLCT}}_{FLCT\ included}}_{Non-inductive\ solution}-\underbrace{\nabla\psi'}_{Potential\ function}$$

To find $\mathbf{E^P}$ (**inductive** electric field), we need to find the Poloidal and Toroidal potentials

$$\nabla_h^2\dot{\mathcal{B}}=-\dot{B}_z$$

$$\nabla_h^2\dot{\mathcal{J}}=-\frac{4\pi}{c}\dot{j}_z=-\mathbf{z}\cdot\left(\nabla\times\dot{\mathbf{B}}_h\right)$$

$$\nabla_h^2\frac{\partial\dot{\mathcal{B}}}{\partial z}=\nabla_h\cdot\dot{\mathbf{B}}_h \Rightarrow \dot{\mathcal{B}},\dot{\mathcal{J}} \Rightarrow c\mathbf{E^P}$$

To find **non-inductive** electric field and potential function, we use Doppler velocities and transverse FLCT velocities. The full electric field that includes **P**TD, **D**oppler, **F**LCT and **I**deal contribution is called **PDFI** electric field.

Kazachenko et al. 2014

$$c\mathbf{E} = -\nabla \times \dot{\mathcal{B}}\hat{\mathbf{z}} - \dot{\mathcal{J}}\hat{\mathbf{z}} - \nabla\psi = c\mathbf{E}^{P} - \nabla\psi = \underbrace{cE^{P}}_{\substack{PTD(inductive)\\ solution}} + \underbrace{\underbrace{cE_{\chi}^{Doppler}}_{\substack{Doppler\\ included}} + \underbrace{cE_{h}^{FLCT}}_{\substack{FLCT\\ included}}}_{\substack{Non-inductive\\ solution}} - \underbrace{\nabla\psi'}_{\substack{Potential\\ function}}$$

Non-inductive component turns out to be important in AR energetics.
How do we evaluate it?

PDFI: Estimating **Non-Inductive** **E** from Doppler shifts

If **E** is non-inductive, i.e.

$$c\mathbf{E}_{\mathbf{h,non-ind}} = -\nabla_h \psi$$

Then this E does not affect dB_r/dt

$$c\nabla \times \mathbf{E}_{\mathbf{h,non-ind}} = -\frac{dB_r}{dt} = 0$$

Example: At PIL: may be substantial electric fields related to flux emergence:

$$c\mathbf{E} = -\mathrm{v}_z \hat{z} \times \mathbf{B}_\mathbf{h} \text{ yet } \frac{dB_z}{dt} = \nabla \times E = 0.$$

We find ψ that gives correct E near PIL.

$$\nabla^2 \psi = -\nabla \cdot \mathbf{E} = \nabla \cdot (\mathbf{V} \times \mathbf{B})$$

Similar approach is used for V_{hor}-potential

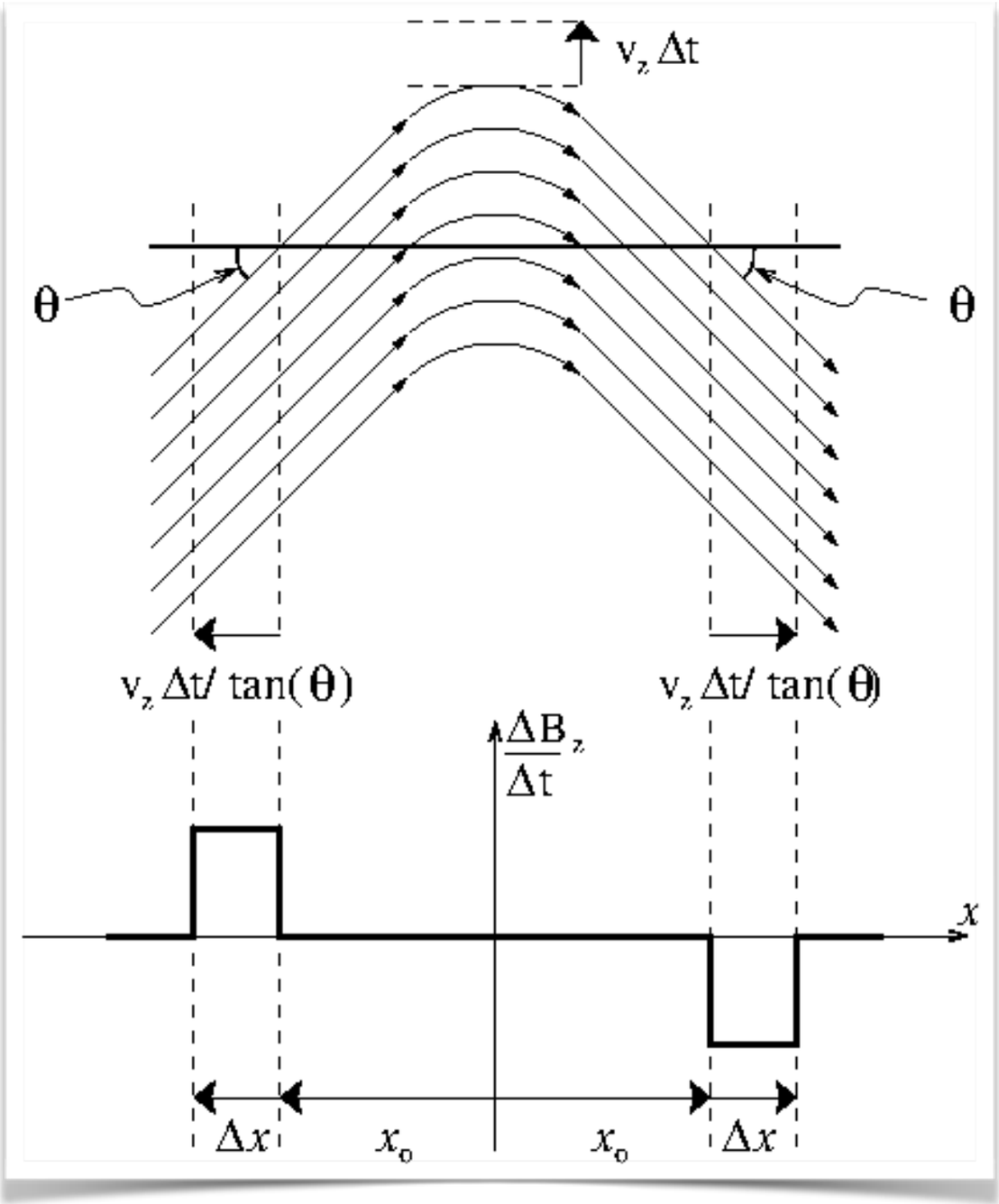

Fisher, Welsch, Abbett, 2011

PDFI: Notation of all different electric field contributions

The full **P**TD **D**oppler **F**LCT **I**deal (PDFI), where the potential function is defined from ideal MHD assumption:

$$E_{PDFI} = \underbrace{cE^{I}}_{\substack{PTD(inductive)\\ solution}} + \underbrace{\underbrace{cE_{\chi}^{Doppler}}_{\substack{Doppler\\ included}} + \underbrace{cE_{h}^{LCT}}_{\substack{FLCT\\ included}}}_{\substack{Non-inductive\\ solution}} - \underbrace{\nabla\psi}_{\substack{Potential\\ function}}$$

$$\nabla\psi \cdot B = (cE^{I} + cE_{\chi}^{Doppler} + cE_{h}^{LCT}) \cdot B$$

Summary of Electric Field Notation

Name	Denoted	Equation for **E**	Input Data / Constraints
P solution[a]	$\mathbf{E^P}$	$c\mathbf{E} = c\mathbf{E^P}$	$\dot{B}_z$, $\dot{J}_z$ (generally, $\mathbf{E}\cdot\mathbf{B} \neq 0$)
PI solution[b]	$\mathbf{E^{PI}}$	$c\mathbf{E} = c\mathbf{E^P} - \nabla\psi^I$	$\dot{B}_z$, $\dot{J}_z$, $\mathbf{E}\cdot\mathbf{B} = 0$
PFI solution[c]	$\mathbf{E^{PFI}}$	$c\mathbf{E} = c\mathbf{E^P} + c\mathbf{E_t^{FLCT}} - \nabla\psi^I$	$\dot{B}_z$, $\dot{J}_z$, $\mathbf{E}\cdot\mathbf{B} = 0$, FLCT output
PDI solution[d]	$\mathbf{E^{PDI}}$	$c\mathbf{E} = c\mathbf{E^P} + c\mathbf{E^D} - \nabla\psi^I$	$\dot{B}_z$, $\dot{J}_z$, $\mathbf{E}\cdot\mathbf{B} = 0$, Dopp. data
PDFI solution	$\mathbf{E^{PDFI}}$	$c\mathbf{E} = c\mathbf{E^P} + c\mathbf{E^D} + c\mathbf{E_t^{FLCT}} - \nabla\psi^I$	$\dot{B}_z$, $\dot{J}_z$, $\mathbf{E}\cdot\mathbf{B} = 0$, Dopp. & FLCT
FI solution	$\mathbf{E^{FI}}$	$c\mathbf{E} = -\mathbf{V_h} \times \mathbf{B^e}$	FLCT data, $V_{LOS} = 0$
DI solution	$\mathbf{E^{DI}}$	$c\mathbf{E} = -\mathbf{V_{LOS}} \times \mathbf{B^e}$	Dopp. data, $V_h = 0$
DFI solution	$\mathbf{E^{DFI}}$	$c\mathbf{E} = -\mathbf{V} \times \mathbf{B^e}$	Dopp. & FLCT data

P for PTD, **I** for ideal, **F** for FLCT, **D** for Doppler, **PI, PFI, PDI, PDFI** are combinations of **P**, **I**, **F** and **D,** for **FI**, **DI**, and **DFI**, we do not include ∇ψ because the total electric field is already ideal.

Kazachenko, Fisher, Welsch (2014)

Advantages of PDFI vs. other methods

- Uses dB/dt to find **E**.
- Satisfies induction equation up to numerical errors.
- Uses Vdopp (contains information about emergence)
- Does not primarily rely on ideal MHD assumption: **E**=-**V** x **B**
- Does not primarily rely on inversions of horizontal velocity using local correlation tracking, but tracking methods (ILCT, DAVE4VM) can provide extra information.

Recent methods to find photospheric electric field

From Faraday's law, ideal MHD and observed **B** (and V_{Dopp})

(1) $\nabla \times \mathbf{E} = -\frac{\partial \mathbf{B}}{\partial t}$ $\qquad \mathbf{E} = -\mathbf{V} \times \mathbf{B}$

Tested with ANMHD

DAVE4VM (Differential Affine Velocity Estimator for Vector Magnetograms, Schuck, 2008):

Input: Full **B**

$$\begin{cases} \frac{\partial B_z}{\partial t} + \nabla_h \cdot (B_z \mathbf{V}_h - V_z \mathbf{B}_h) = 0 \\ \mathbf{E} = -\mathbf{V} \times \mathbf{B} \end{cases}$$

PDFI (PTD-Doppler-FLCT-Ideal) method (Kazachenko, Fisher, Welsch 2014)

Input: Full **B**, Vdopp

$$\begin{cases} \mathbf{E} = \mathbf{E}_I - \nabla\psi & \text{inductive} \\ \nabla \times \mathbf{E}_I = -\frac{\partial \mathbf{B}}{\partial t} & \text{non-inductive} \\ \nabla^2 \psi = -\nabla \cdot \mathbf{E} = \nabla \cdot (\mathbf{V} \times \mathbf{B}) \end{cases}$$

Cheung et al. 2012, 2015
Mackay et al. 2014 etc.

B_z only / Full **B**

$$\begin{cases} \nabla\psi = 0 & (0) \\ \nabla_h^2 \psi = -\nabla_h \cdot \mathbf{E}_h = -\Omega B_z & (1) \\ \nabla_h^2 \psi = -\nabla_h \cdot \mathbf{E}_h = -U (\nabla \times \mathbf{B}) \cdot \hat{\mathbf{z}} & (2) \end{cases}$$

free parameters

Yeates et al. 2017 — B_z only — $(1)_z$

Tremblay et al. 2015, 2017 — MEF-R generalization of MEF (Longcope 2004)

Courtesy Erkka Lumme

PDFI & DAVE4VM

Validation

PDFI validation using ANMHD simulations

- Evolution of vector magnetic field in small "sunspot" emerging through convective zone
- Both **V** & **B** are known
- Common test case for validation of velocity inversions

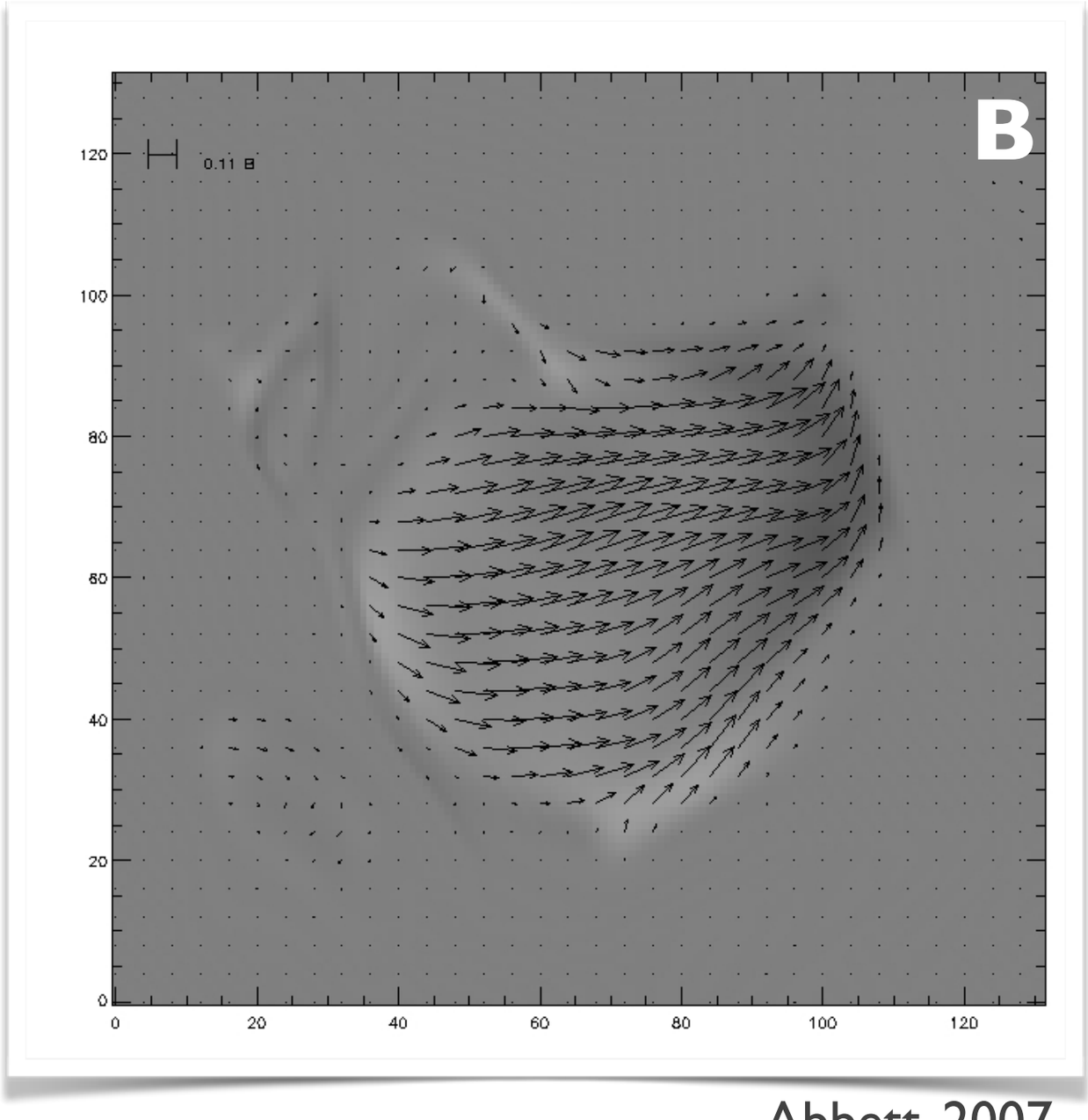

Abbett, 2007

PDFI Electric field validation

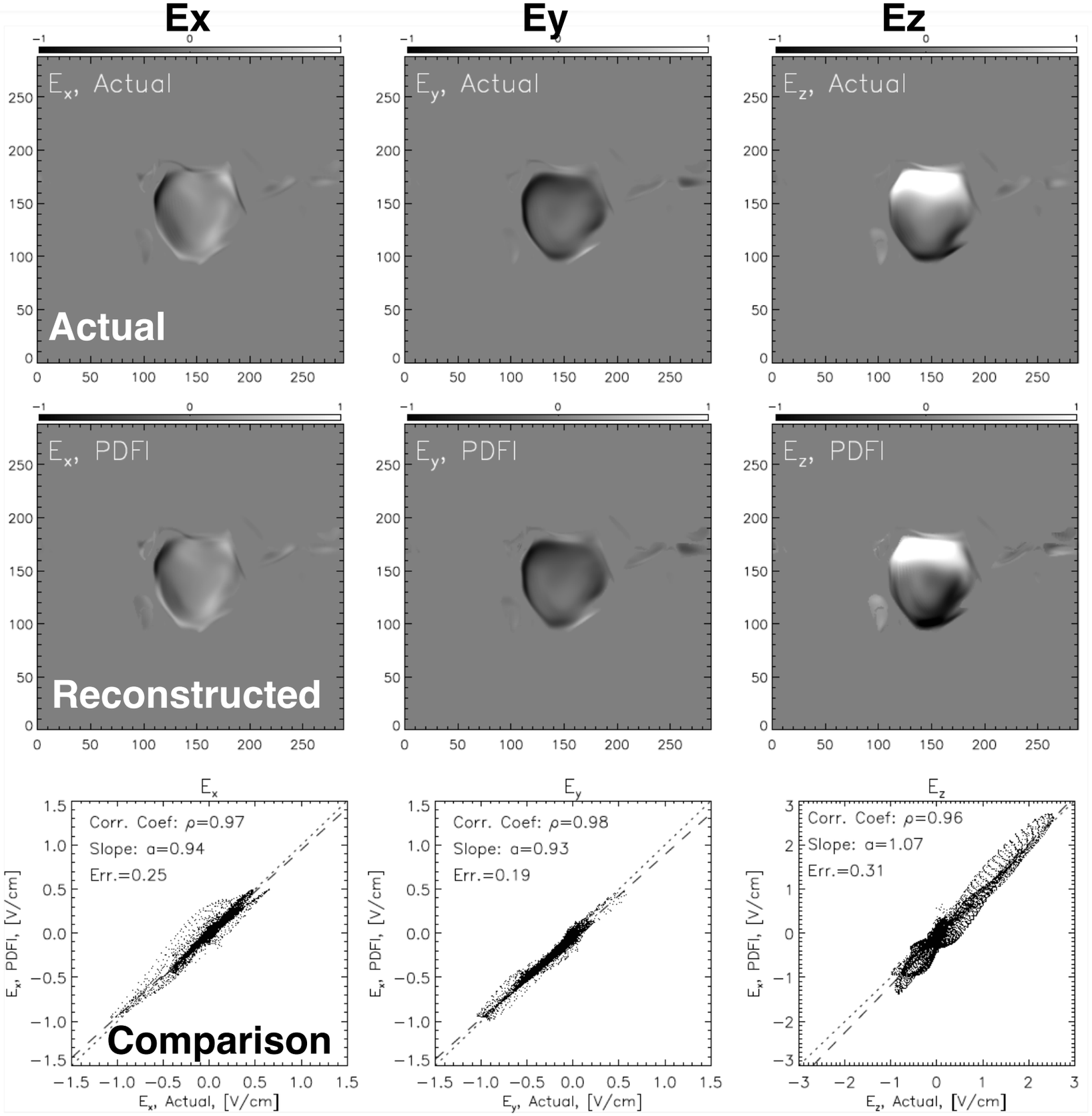

- Actual electric fields **[Ex, Ey, Ez]** from ANMHD test simulation
- Reconstructed **[Ex, Ey, Ez]** from the PDFI method
- Scatter plots of inverted versus actual electric field components

Kazachenko, Fisher, Welsch (2014)

PDFI Poynting flux validation

$$S_z = \frac{c}{4\pi}(E_x B_y - E_y B_x)$$

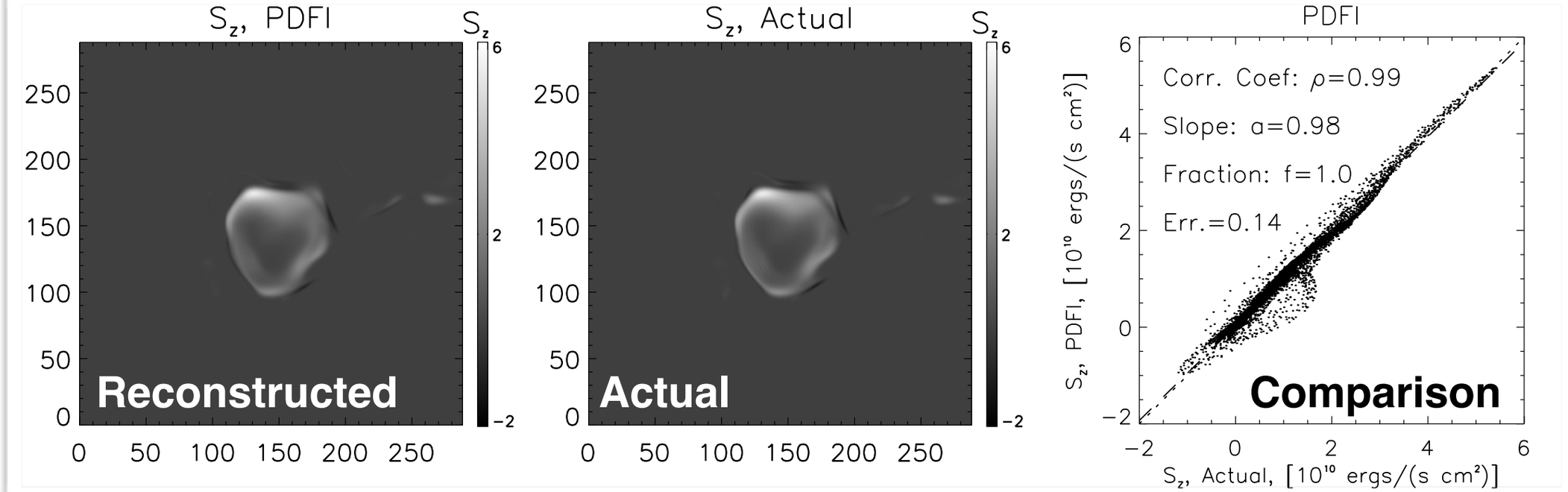

Validation conclusion: qualitative and quantitative comparisons show **excellent recovery** of the electric field and vertical Poynting flux

PDFI Poynting flux validation: importance of non-inductive **E**

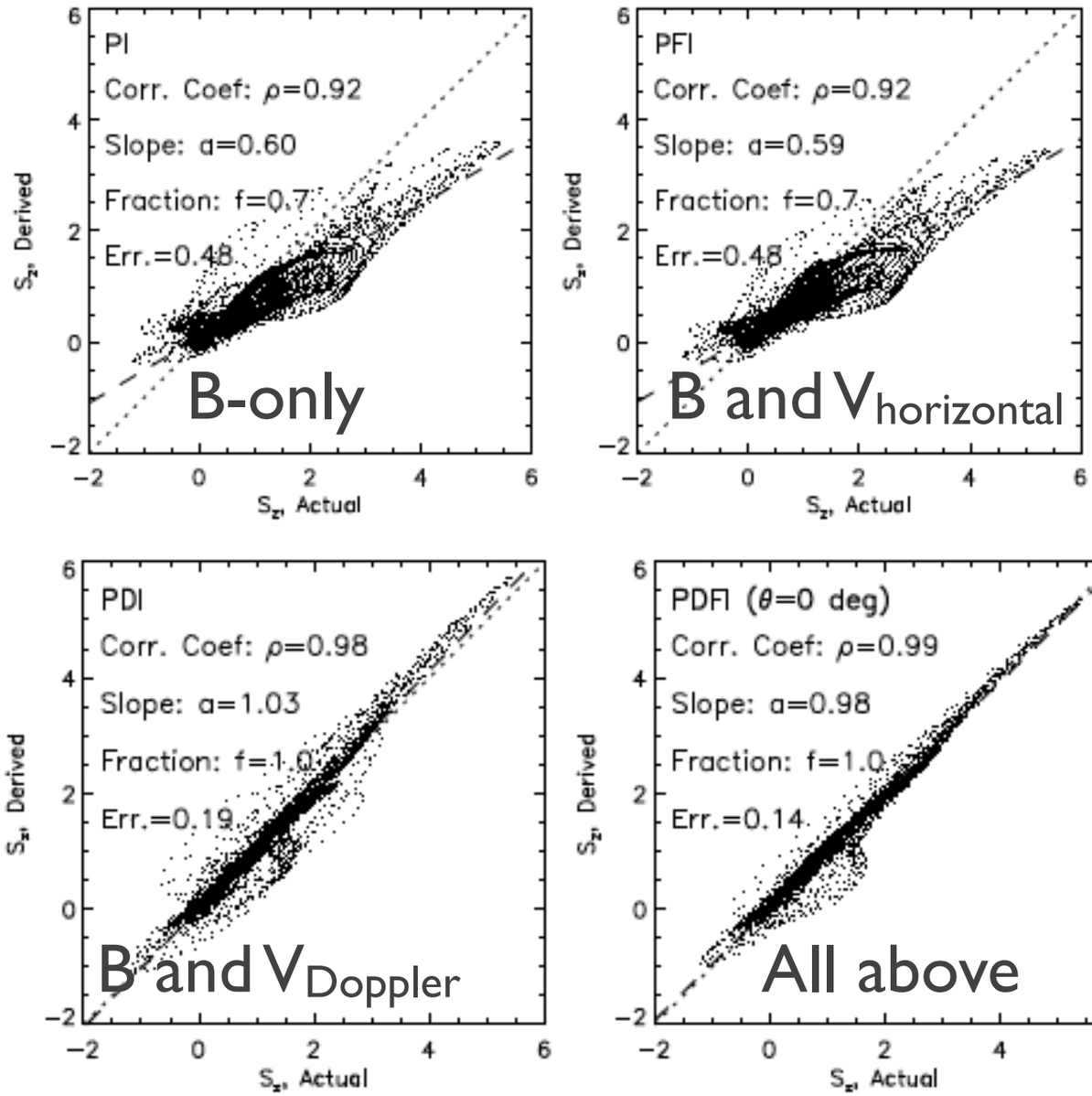

Kazachenko, Fisher, Welsch 2014

- Scatter plots of ANMHD model inverted versus actual energy flux derived from B-only, B+ $V_{horizontal}$, B+ $V_{Doppler}$ and their combination

- Here without non-inductive components we miss ~**30%** of the energy flux

Comparison of different inversion methods: Poynting Flux Estimates

Kazachenko, Fisher, Welsch (2014)

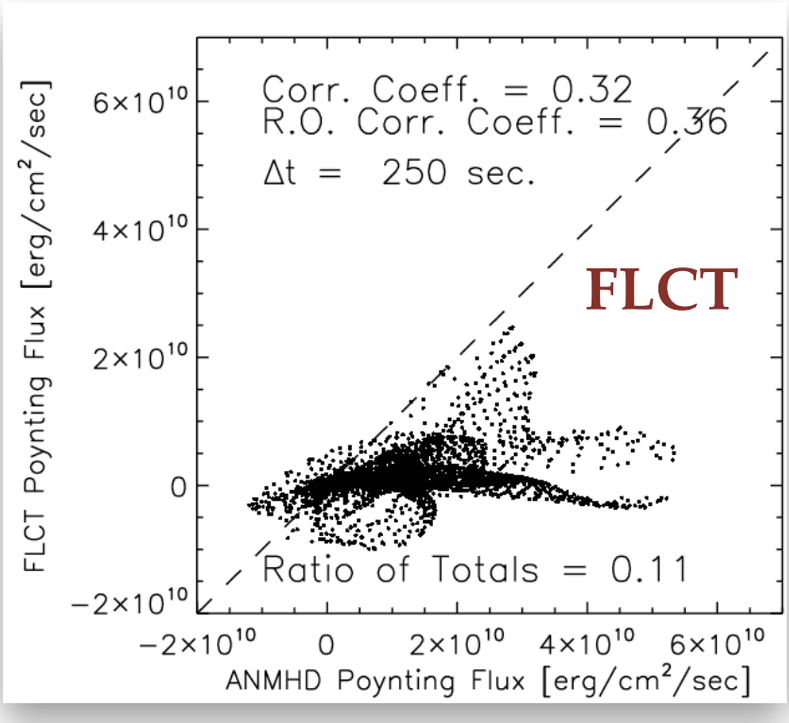

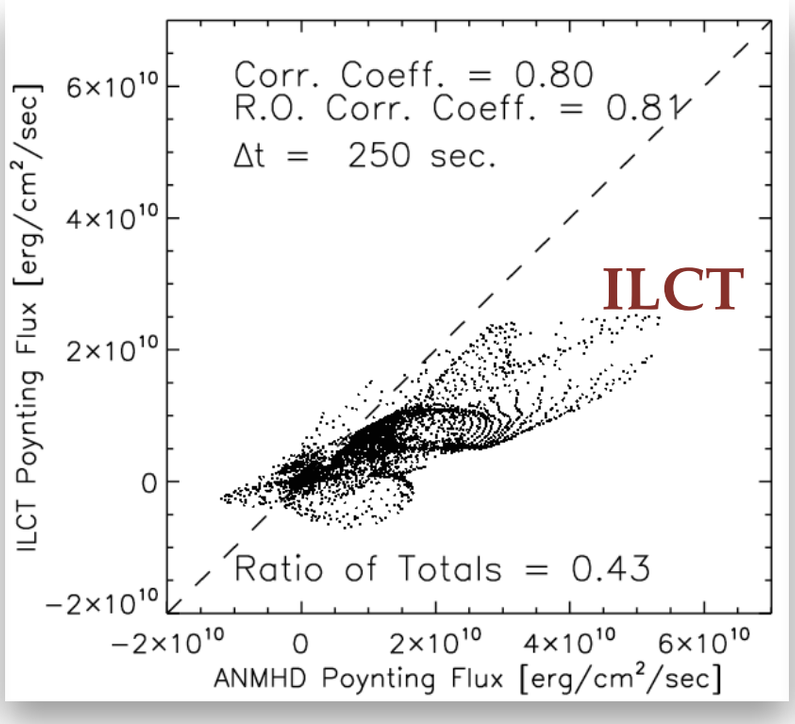

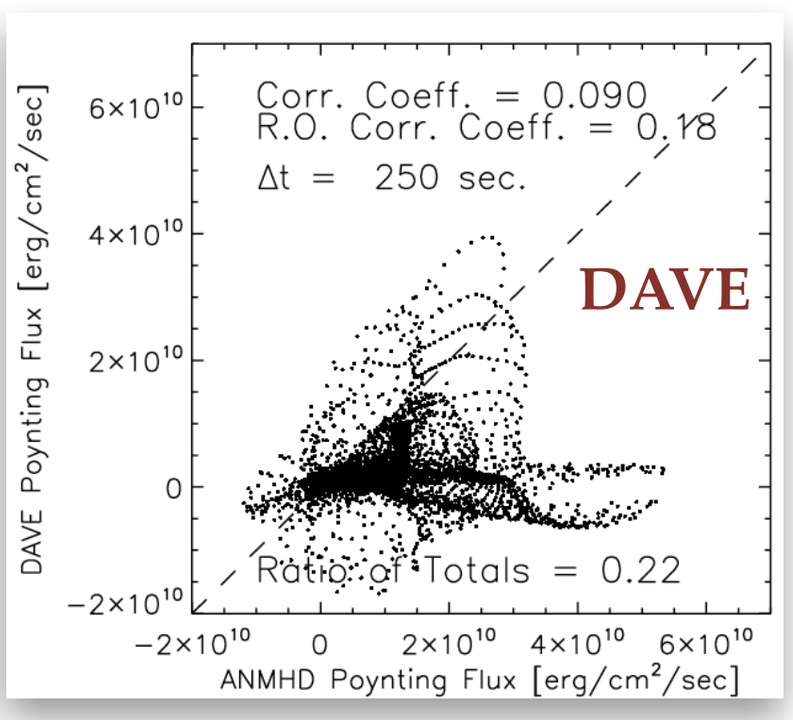

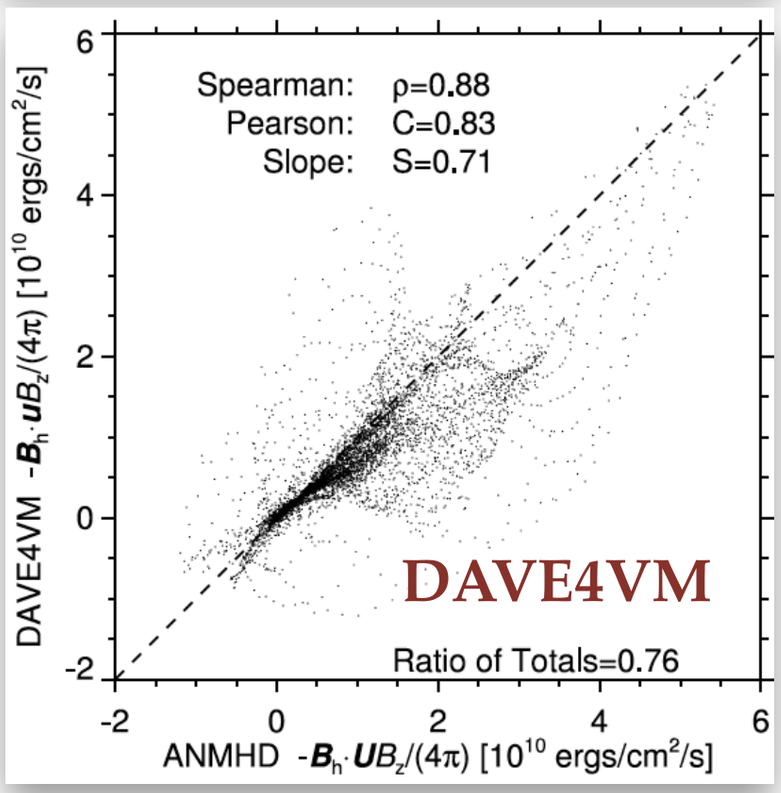

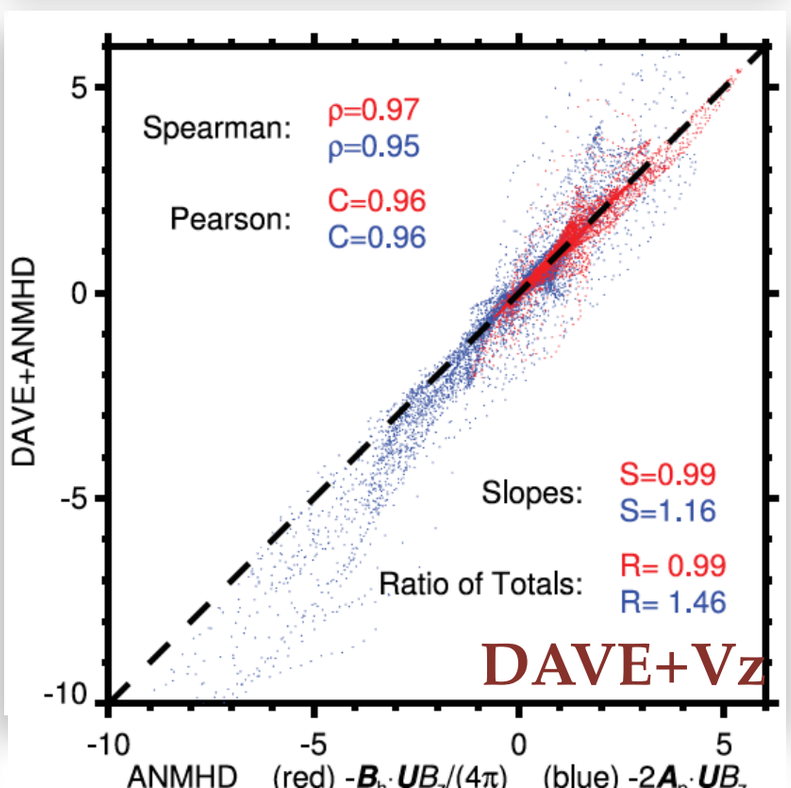

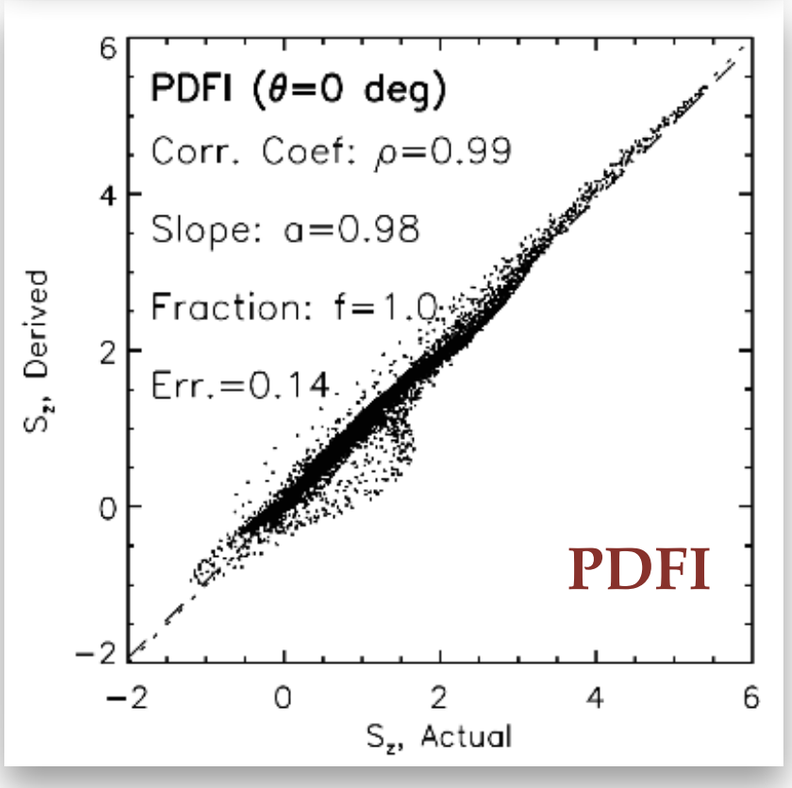

Accuracy of PDFI vs DAVE, DAVE4VM

Comparison of Accuracy of Poynting and Rate of Relative Helicity Fluxes Estimates between the PDFI, PFI, DAVE+ANMHD, and DAVE4VM (Schuck 2008) over $|B_z| > 370$ G

	PFI	DAVE4VM	PDFI	DAVE+ANMHD	PFI	DAVE4VM	PDFI	DAVE+ANMHD
	Poynting flux, S_z				Helicity flux rate, dH_R/dt			
Slope, a	0.92	0.71	0.99	0.99	0.96	0.9	0.99	1.16
Corr. coef., ρ	0.59	0.83	0.98	0.96	0.95	0.94	1.08	0.96
Fraction, f	0.7	0.76	1.0	0.99	1.0	0.94	1.1	1.46

Notes. An ideal reconstruction satisfies $a = 1$, $\rho = 1$, $f = 1$.

Kazachenko, Fisher, Welsch (2014)

- Poynting flux: PDFI performs better than DAVE4VM and similar to DAVE+ANMHD in reconstructing Poynting flux.
- Helicity flux: PDFI is slightly better than DAVE4VM and better than DAVE+ANMHD in reconstructing helicity fluxes.

Examples of Poynting Fluxes Derived From Observations

In active regions:

Will show in the class

- Kusano et al. (2002): analysis of MDI Bz and NAOJ Bh observations in AR8100.
- Welsch et al. (2004): analysis of IVM observations for AR 8210 using IFLCT method.
- Tan et al. (2007): analysis of "proxy" Poynting fluxes (Bz=Bh): in 160 ARs
- Liu & Schuck 2014: analysis of B and Vz HMI/SDO data in AR11158 & AR11072 using DAVE4VM (Liu & Schuck 2014)
- Kazachenko et al. (2015): analysis of HMI/SDO data in AR 11158 using PDFI method

In plage:

- Welsch et al. 2014, Yeates et al. 2014

Poynting Flux in Plage

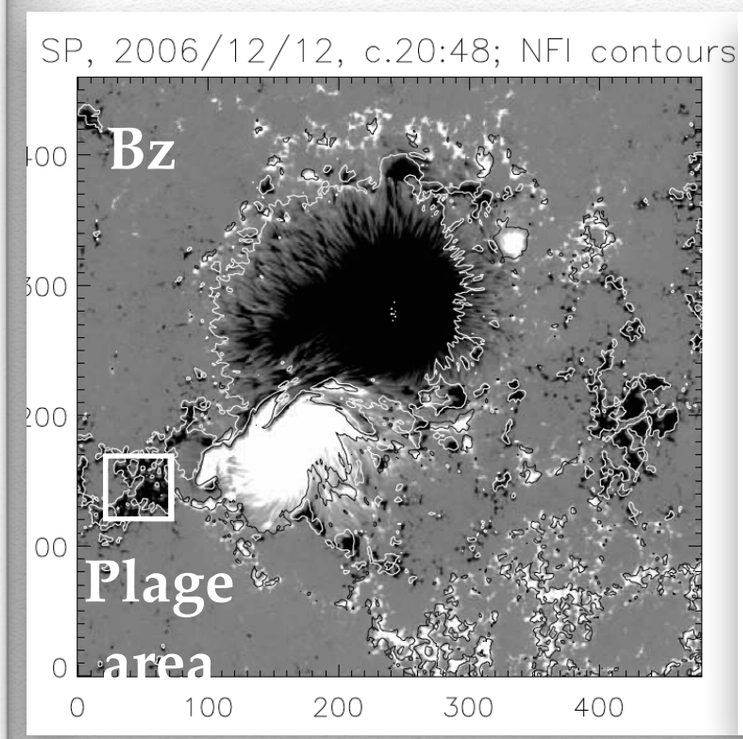

Bz snapshot

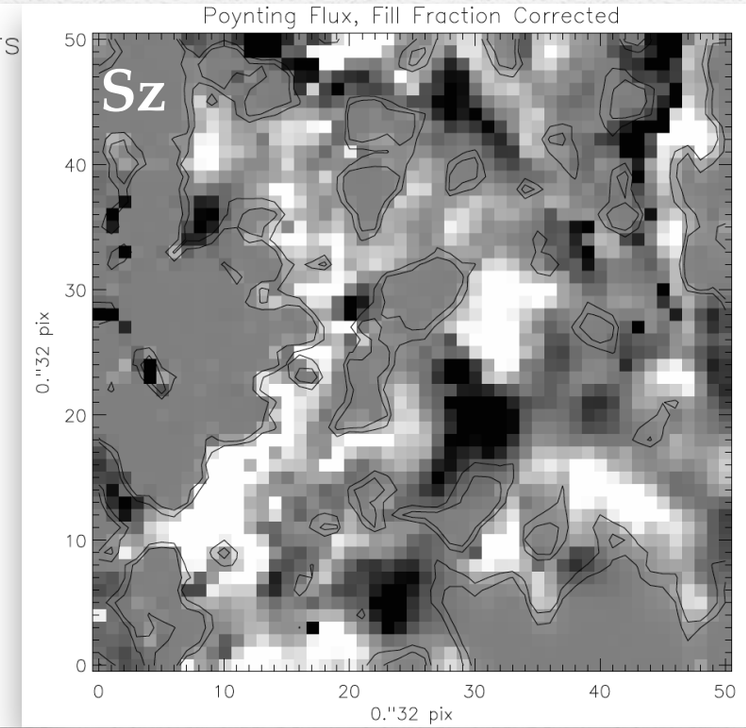

Sz ranges from within [-4, 4]*10^8 erg $cm^{-2}s^{-1}$

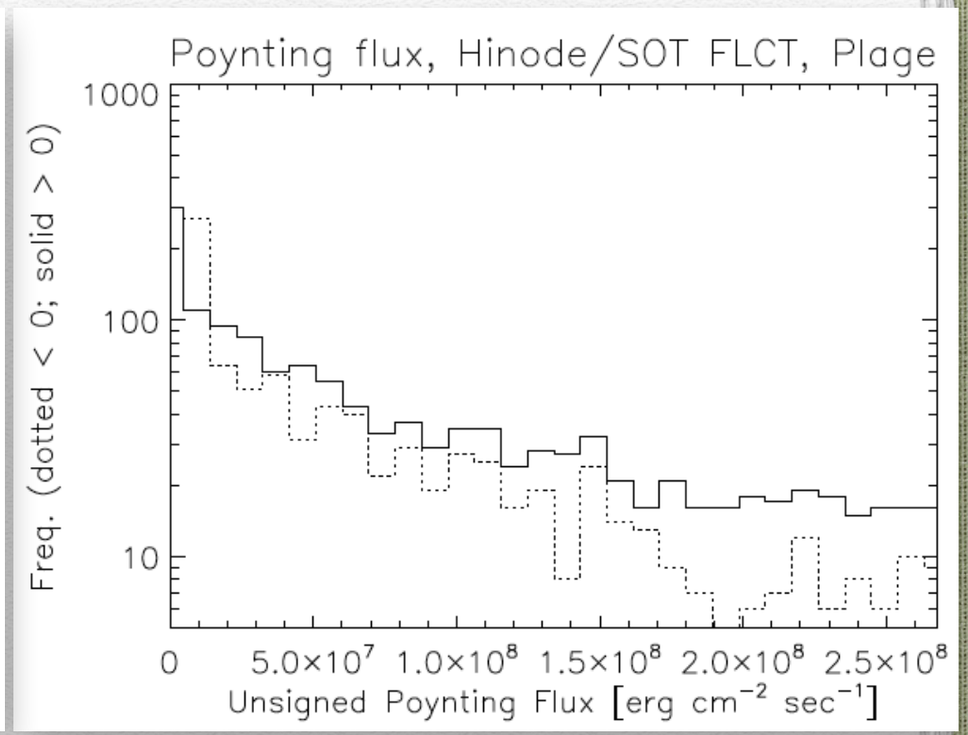

Sz histograms for Plage pixels

- Plage: Mostly vertical B; can neglect Bh

$$S_z = [v_z B_h^2 - (\mathbf{v_h} \cdot \mathbf{B_h}) B_z]/4\pi = -(\mathbf{v_h} \cdot \mathbf{B_h}) B_z/4\pi$$

- Vh from FLCT velocities, Bh and Bz from Hinode
- Found that Sz is overall positive
- Sz (plage) ~ (2.6-2.8) 10^7 ergs cm-2 s-1

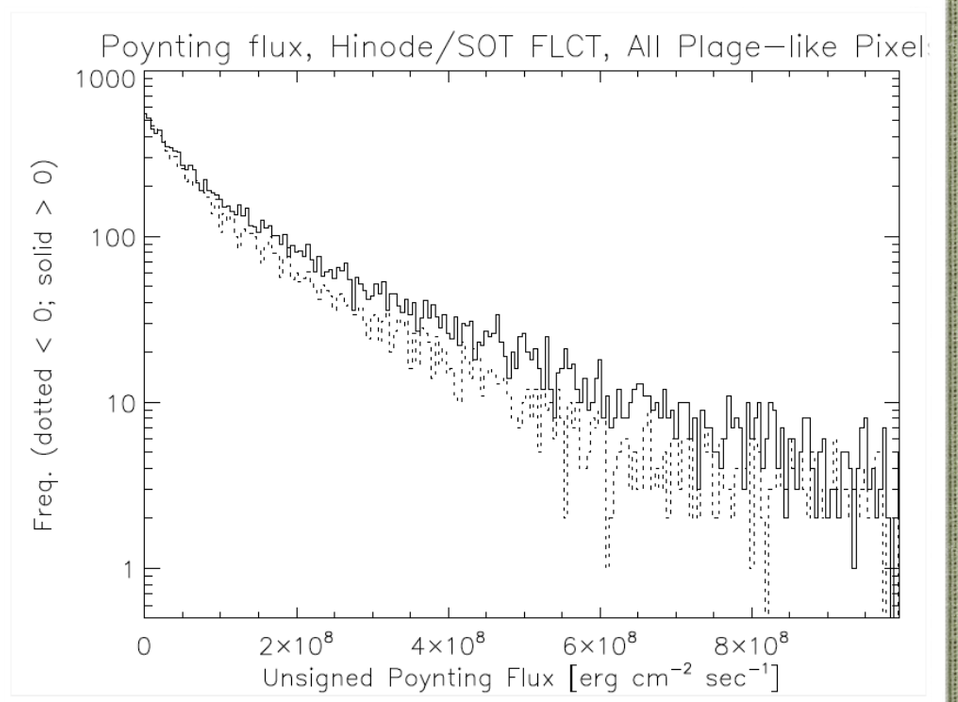

Sz histograms for all plage-like pixels

Welsch 2014

Poynting fluxes in ARs: Used HMI/SDO B and Vz in AR11158 To Find High Cadence **E** and Sz

- Applied the PDFI method to evolution of AR 11158.
- Data cube: Bx, By, Bz, Vz during 7 days;
- dt=12 minute, dx=360 km
- Dataset dimensions: 665*645*768
- Corrected for 180-degree ambiguity errors
- Applied absolute scale Doppler shift corrections
- Re-projected data to disk center.
- Transformed to Cartesian centered grid using Mercator De-projection
- Corrected fluxes for distortion of pixel areas from re-projection.

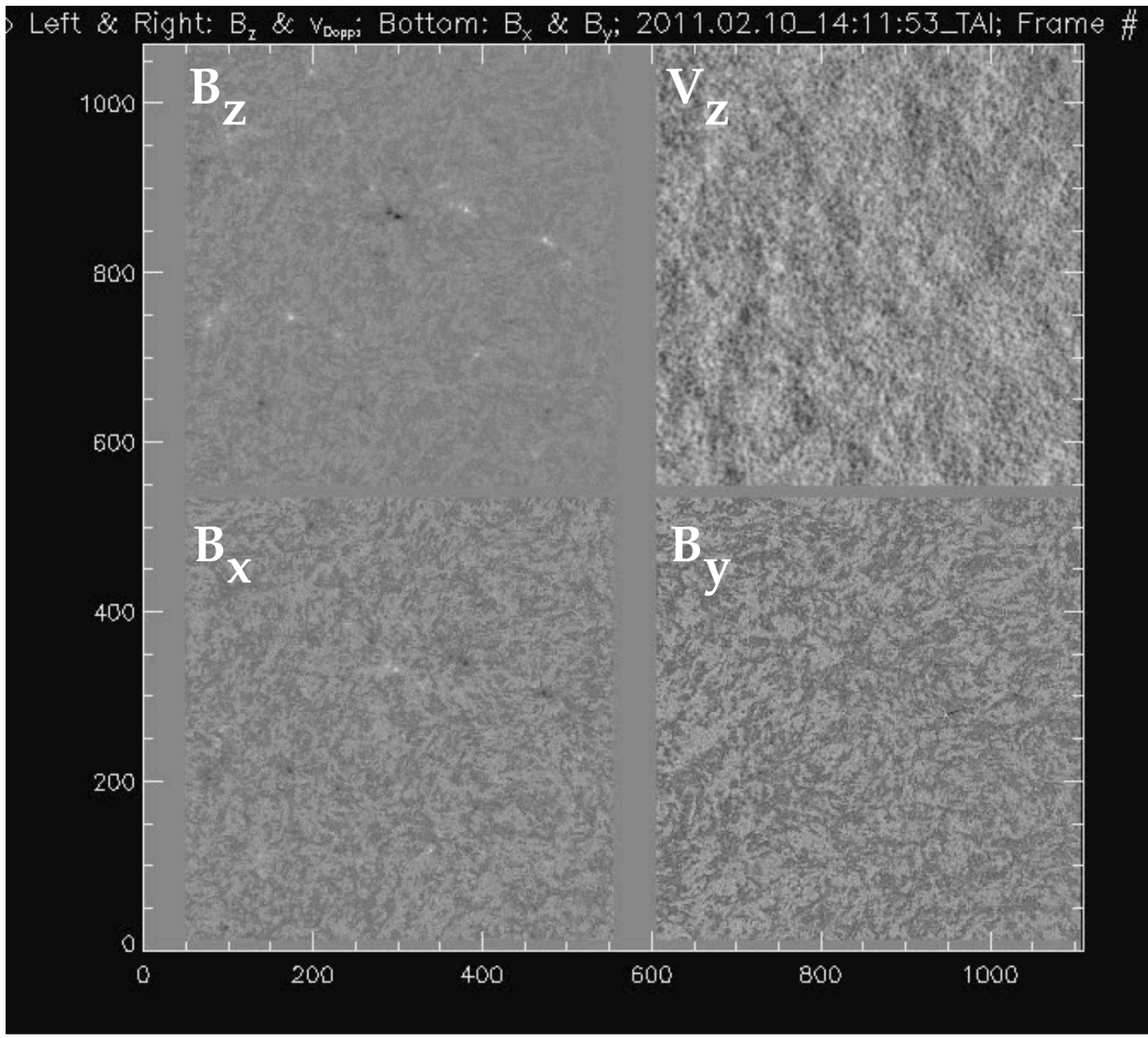

Welsch, Fisher, Sun (2012); Kazachenko, Fisher, Welsch, Liu, Sun (2015)

Observed Magnetogram and PDFI Electrogram during 6 days of AR evolution

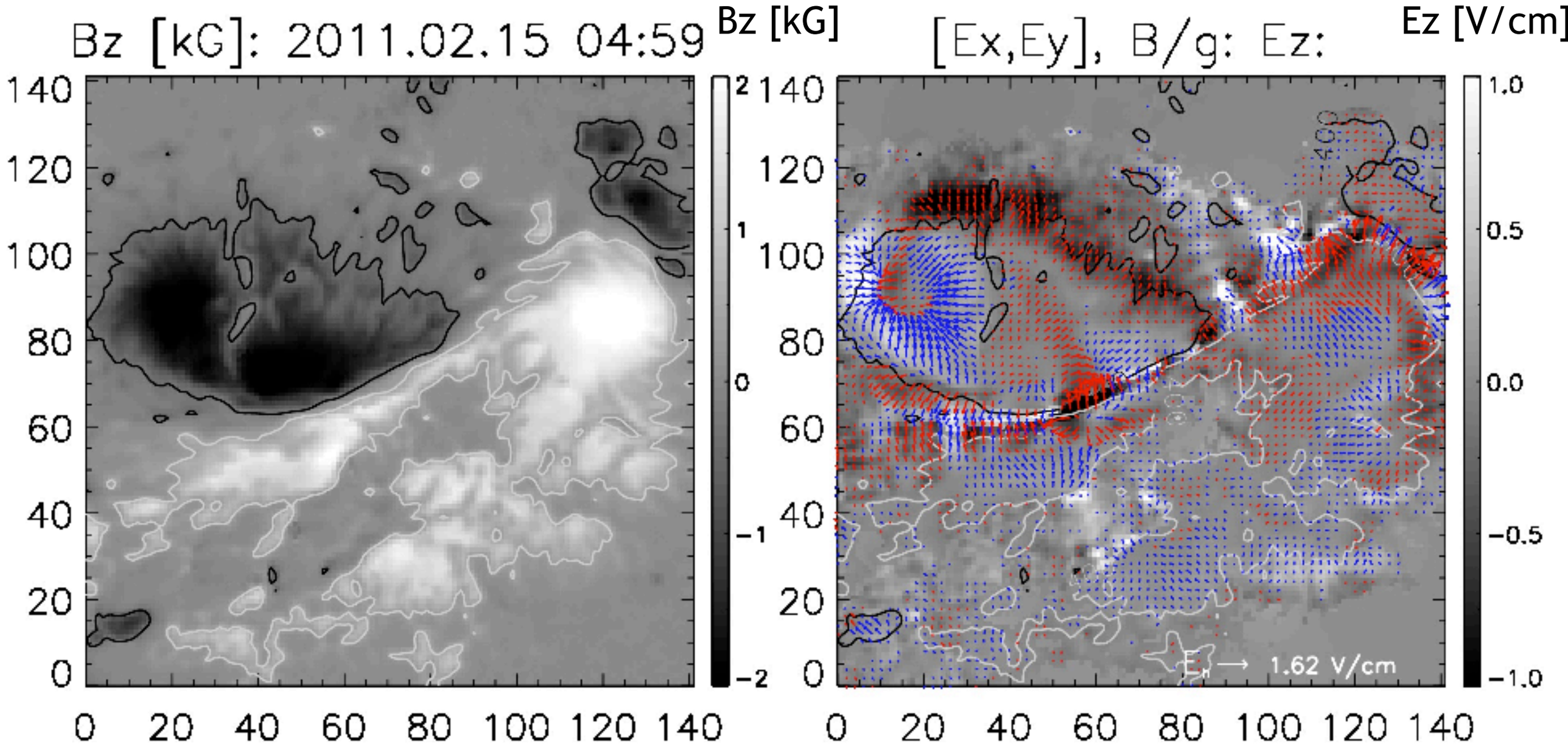

Kazachenko, Fisher, Welsch, Liu, Sun et al. 2015

Single Snapshot of B and E

Magnetogram

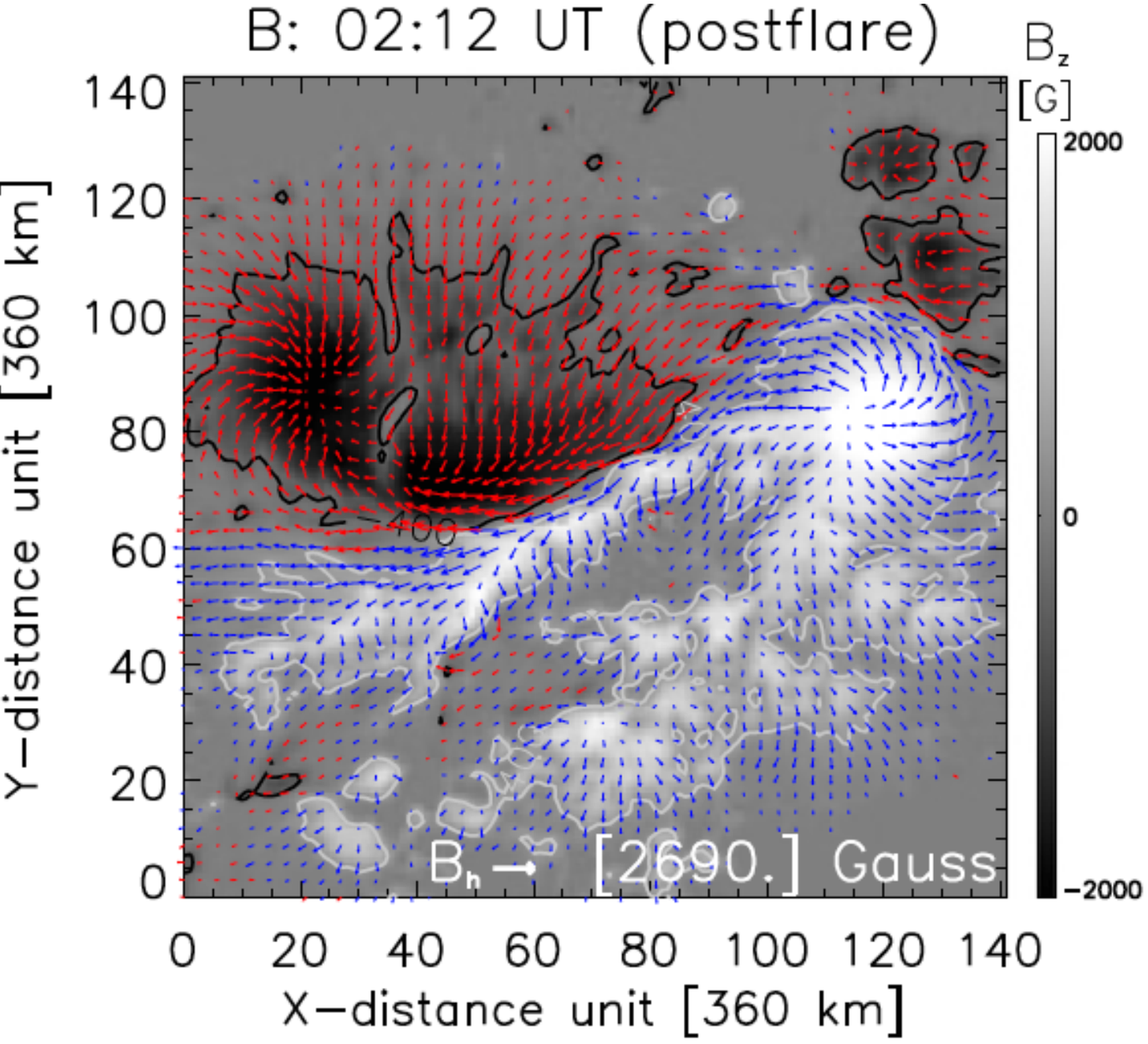

PDFI electrogram

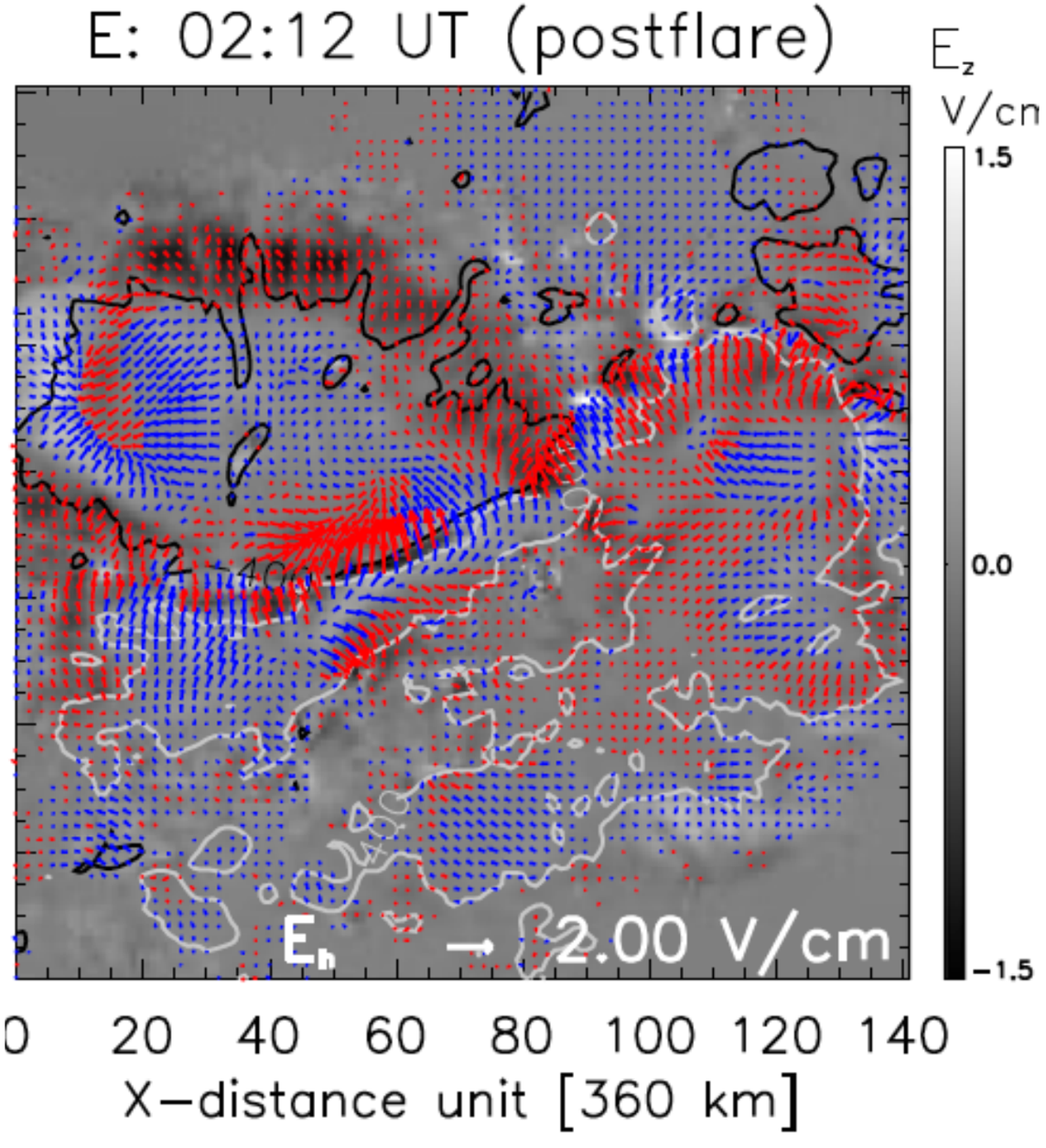

Kazachenko et al. 2015

Observed Magnetogram and Derived Energy Flux during 6 days of AR evolution

Vertical magnetic field

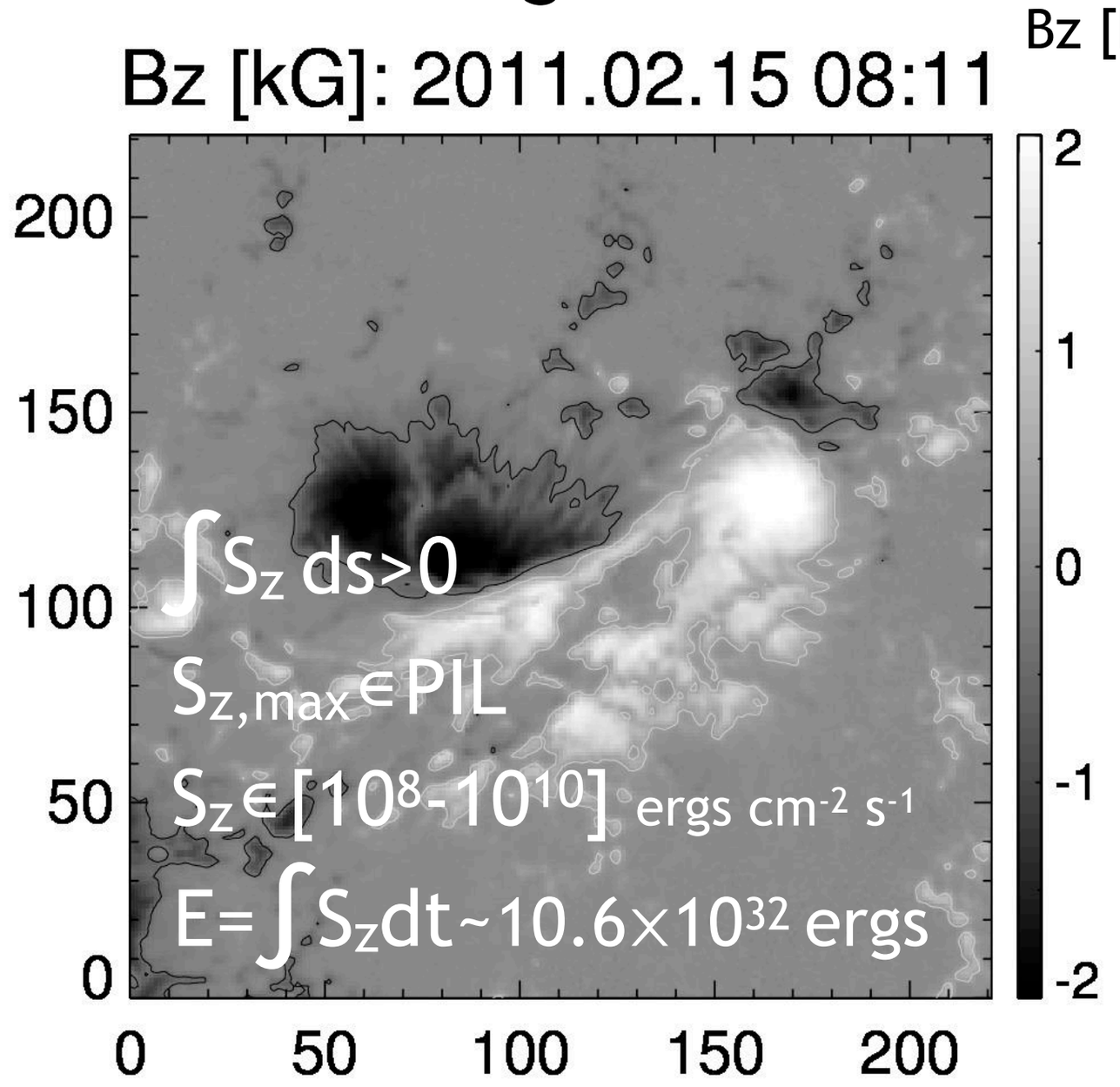

Vertical Poynting flux

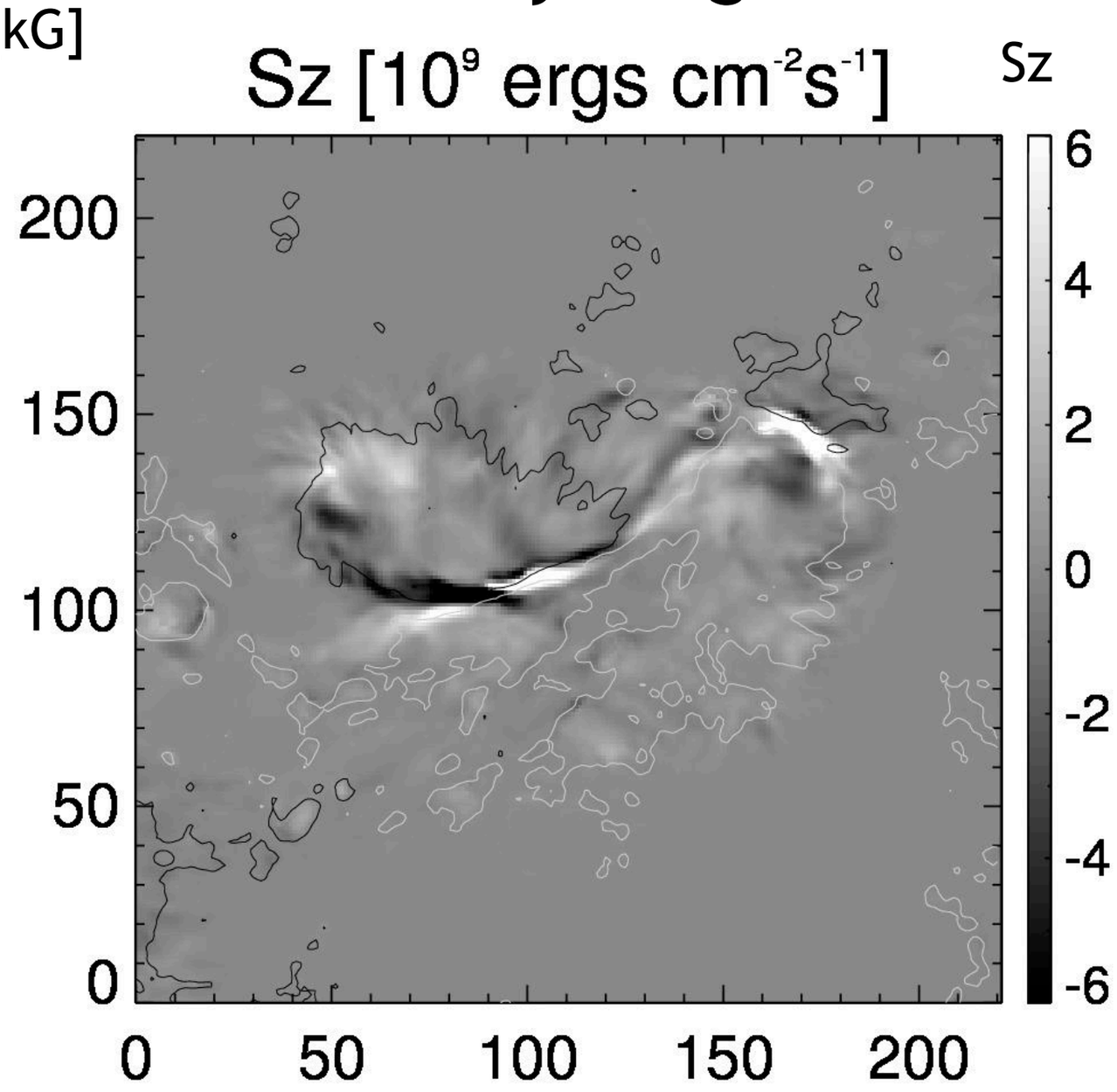

Kazachenko et al. 2015

PDFI: Cumulative Energy and helicity fluxes in AR 11158

- **Right:** magnetic flux (top), integrated Poynting flux (middle) and GOES flux (bottom) evolution in AR 11158.
- **Bottom:** helicity flux flux evolution in AR 11158 (from DFI (VxB) and **PDFI** approaches)

$|Bz|$

Sz

GOES flux

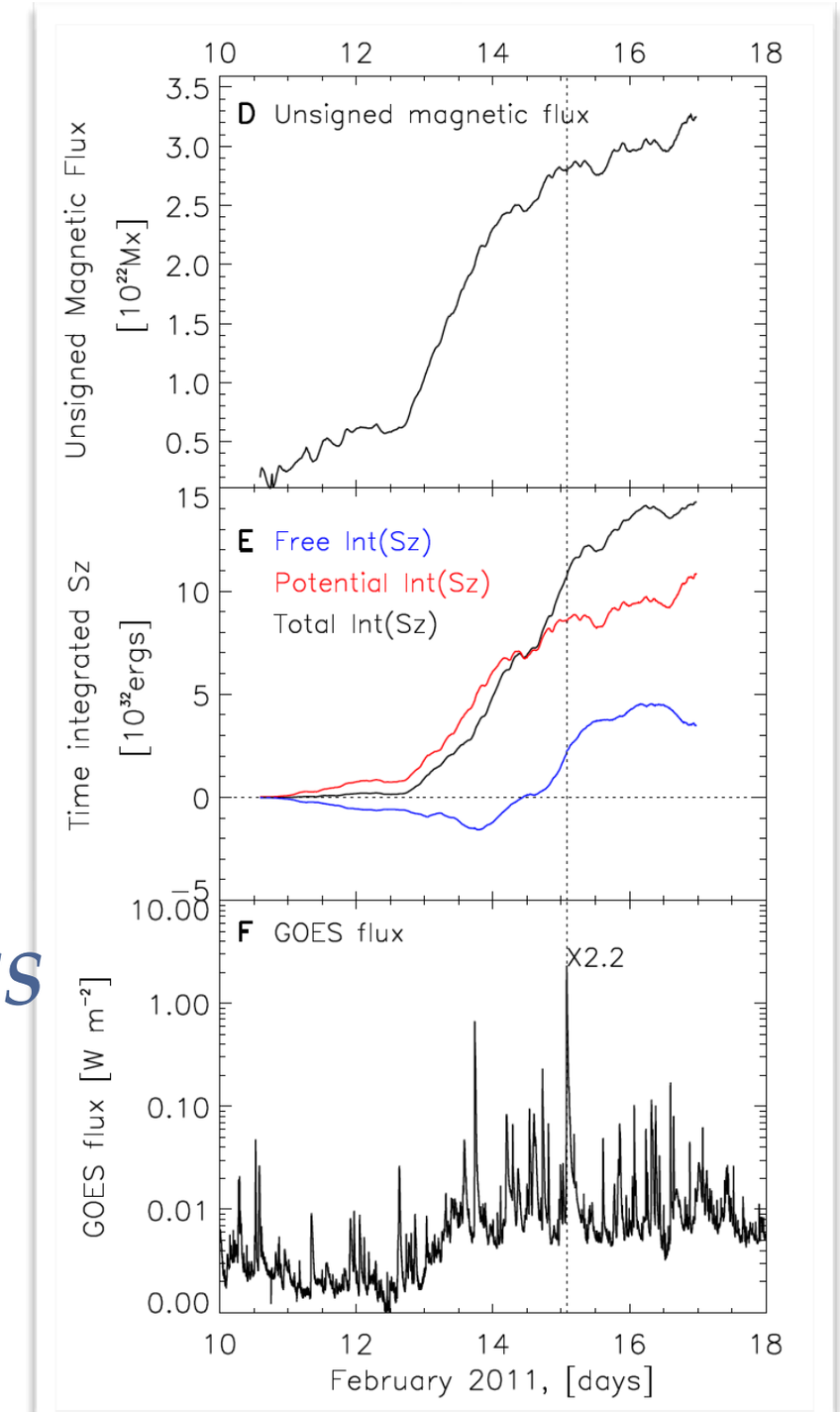

Kazachenko, Fisher, Welsch, Liu, Sun (2015)

H_R: PDFI vs DFI

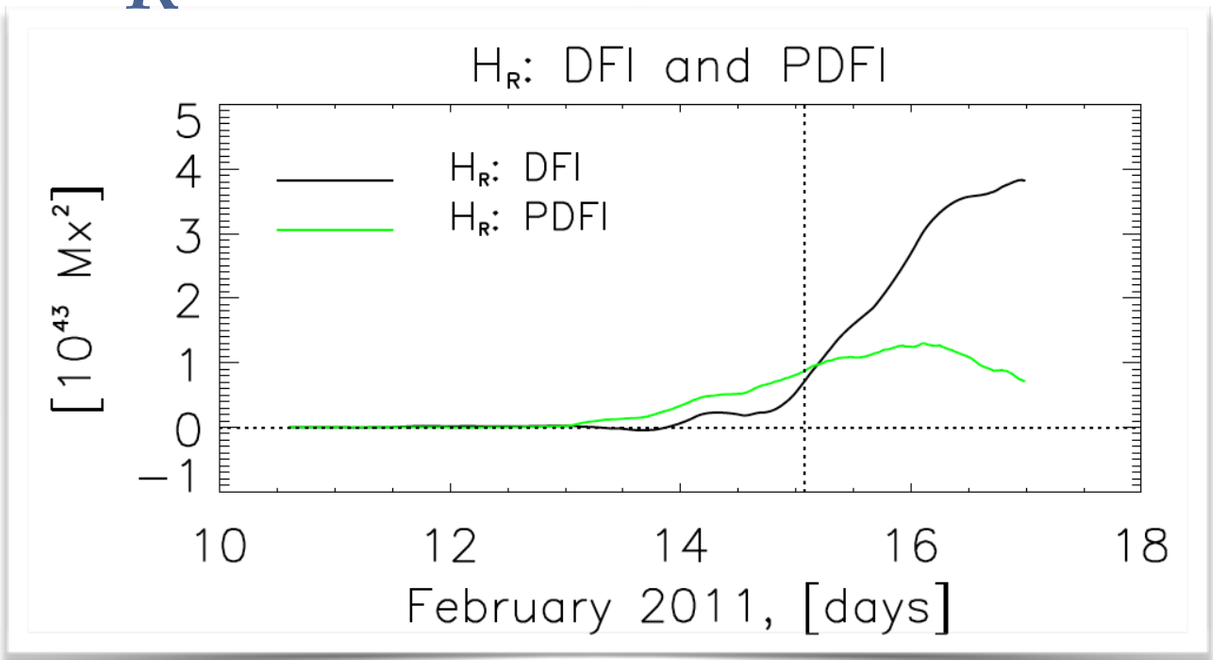

Cumulative energy fluxes in AR 11158: DAVE4VM method

- Liu and Shuck 2012: energy flux analysis in AR 11158 using DAVE4VM and **B**.
- Analyzed emerging (from Vn) and shearing (from Vt) terms of Sz: found that emerging term slightly dominates shearing term
- Compared DAVE and DAVE4VM outputs: Found that energy flux from DAVE4VM is significantly larger than from DAVE4VM.

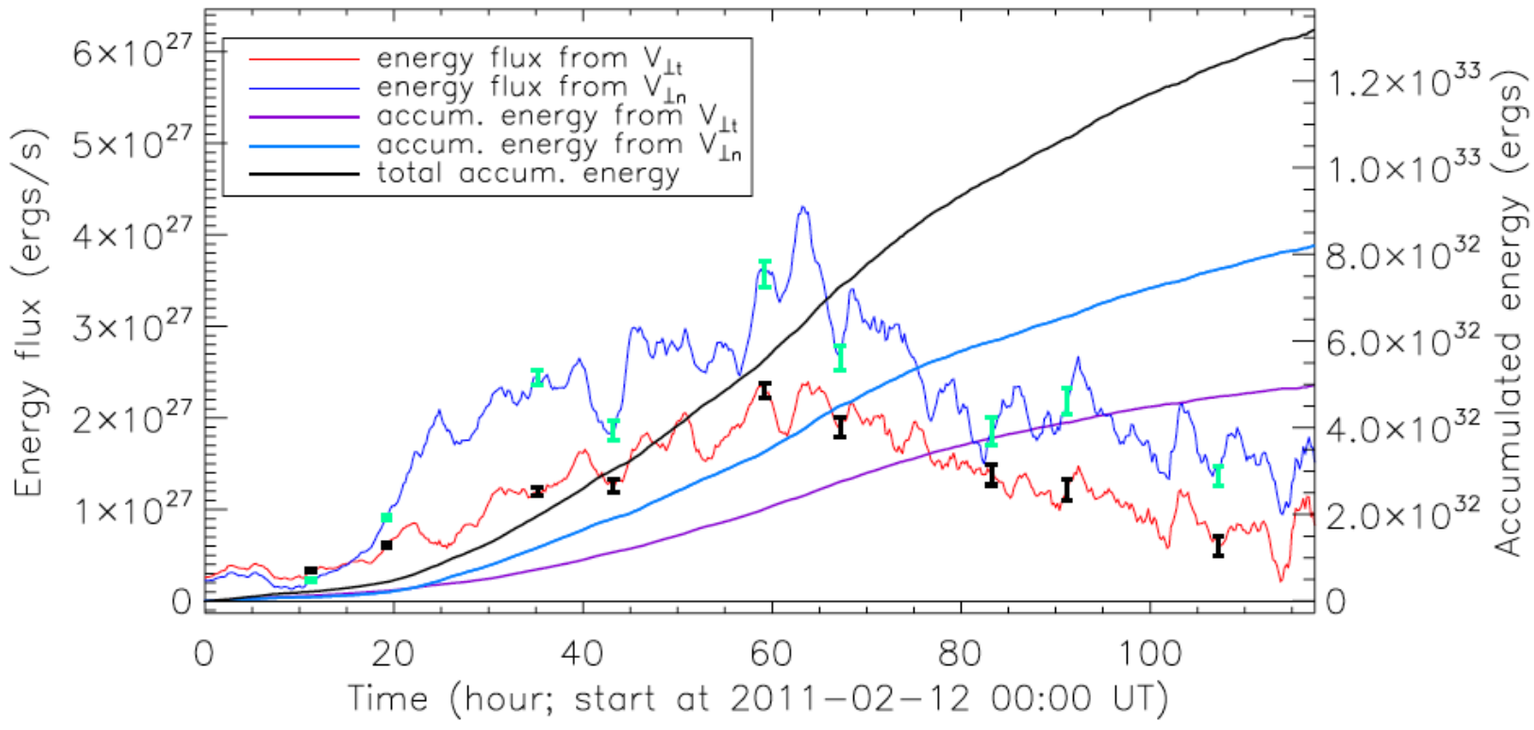

Liu and Shuck 2012

AR11158: Comparison of different energy E and helicity H_R estimates

Paper	Method	Data	Free energy dE	Potential energy E_f	Potential energy E_p	Total energy E	Total helicity H_R
			10^{32} ergs				10^{42} Mx^2
Photospheric Estimates							
This paper	**PDFI Method**	$\mathbf{B}, \mathbf{V_z}$	–	**2.0**	**8.6**$^{(d)}$	**10.6**	**8.5**
...	DFI method	$\mathbf{B}, V_z$	–	–	–	–	7.8
Tarr et al. (2013)	MCC model	B_{LOS}	1.7	2.9	5.6$^{(d)}$	8.5	–
Liu et al. (2012b)	DAVE4VM	$\mathbf{B}, V_z$	–	–	–	8.8	6.5
Tziotziou et al. (2013)	DAVE4VM	$\mathbf{B}, V_z$	–	–	–	8.0	8.5
Vemareddy et al. (2012b)	DAVE	$\mathbf{B}$	–	–	–	–	6.0
Jing et al. (2012)	DAVE	$\mathbf{B}$	–	–	–	–	5.5
Coronal Estimates							
Malanushenko et al. (2014)	Coronal NLFF$^{(a)}$	B_{LOS}	1	1.2	4.8$^{(e)}$	6	–
Aschwanden et al. (2014)	Coronal NLFF$^{(a)}$	B_{LOS}	0.6	1.0	7.6$^{(f)}$	8.6	–
Sun et al. (2012)	NLFFF method$^{(b)}$	$\mathbf{B}$	0.3	2.6	8.0$^{(d)}$	10.6	–
Tziotziou et al. (2013)	NLFFF method$^{(c)}$	$\mathbf{B}$	0.8	–	–	12	13
Jing et al. (2012)	NLFFF method$^{(b)}$	$\mathbf{B}$	–	–	–	–	5.2

NLFFF method: $^{(a)}$ – EUV loops instead of B_t are used as a constraint, $^{(b)}$ – Wiegelmann (2004), $^{(c)}$ – Georgoulis et al. (2012). *Potential field methods:* $^{(d)}$ – Green's function, Sakurai (1989), $^{(e)}$ – Alissandrakis (1981), $^{(f)}$ – Aschwanden and Sandman (2010).

Kazachenko, Fisher, Welsch, Liu, Sun (2015)

Estimating energies and helicities on the Sun is a messy business!

- The total Poynting flux injected before the flare is (10.6+-3.0) 1032 ergs, consistent with E from DAVE4VM, MCC and NLFFF methods, and larger than that from the coronal NLFF estimates.
- The relative magnetic helicity is consistent with photospheric helicity methods (e.g. DAVE4VM), but disagrees with Hr from coronal methods (NLFFF).
- |E| varies from 0 to 1.5 V/cm ; Eh is mostly concentrated along the PIL, while Ez is largest at PIL and penumbrae.
- Sz ranges from 0 to 10^{10} ergs cm-2s-1 with mean values of $10^{8\text{-}9}$ ergs cm-2s-1 and maximum at the PIL.
- The PDFI errors are estimated redoing PDFI analysis for the HMI data with artificial noise;

Pre- And Postflare Magnetic Fields

Kazachenko et al. 2015

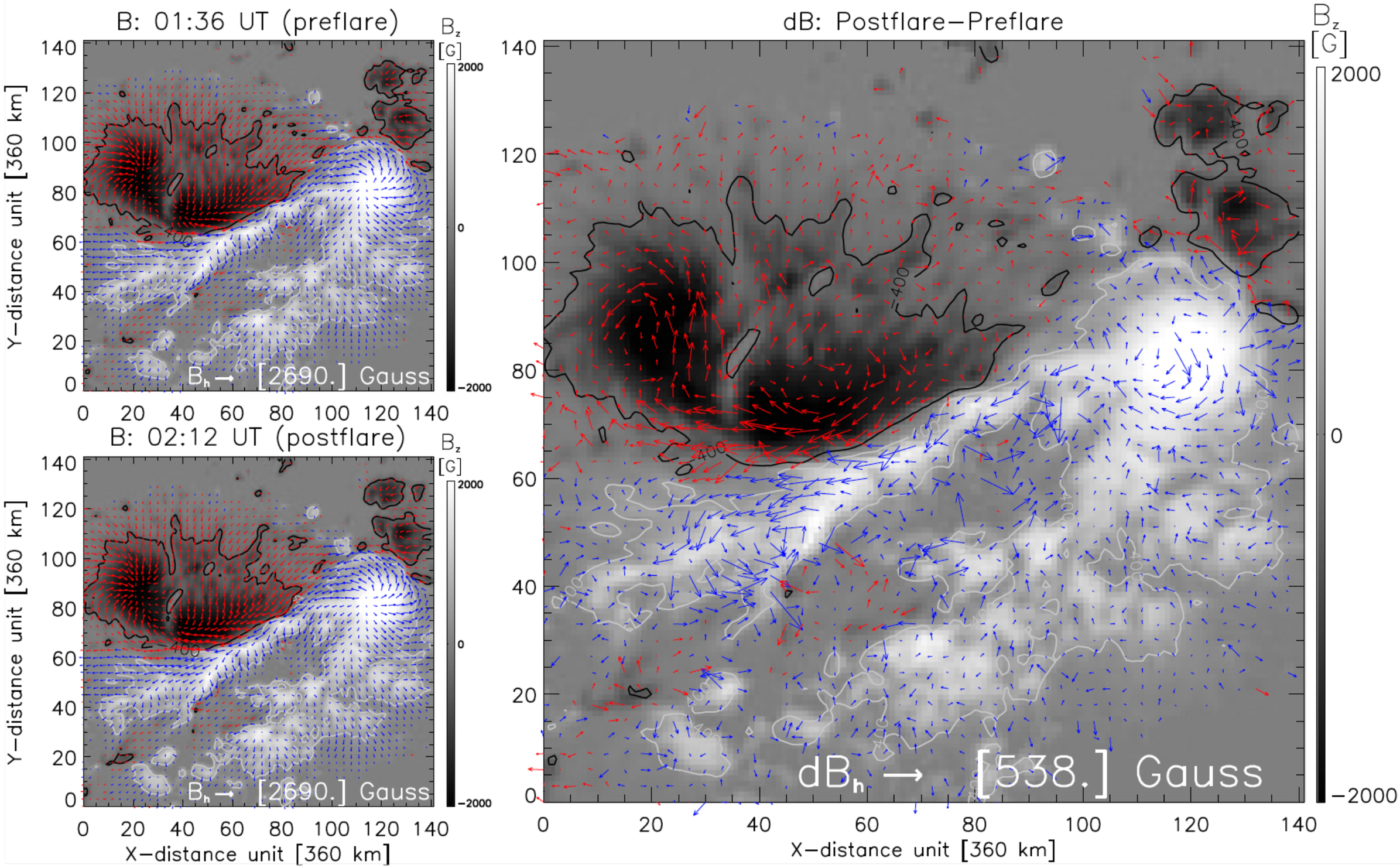

Pre- And Postflare Electrograms

Kazachenko et al. 2015

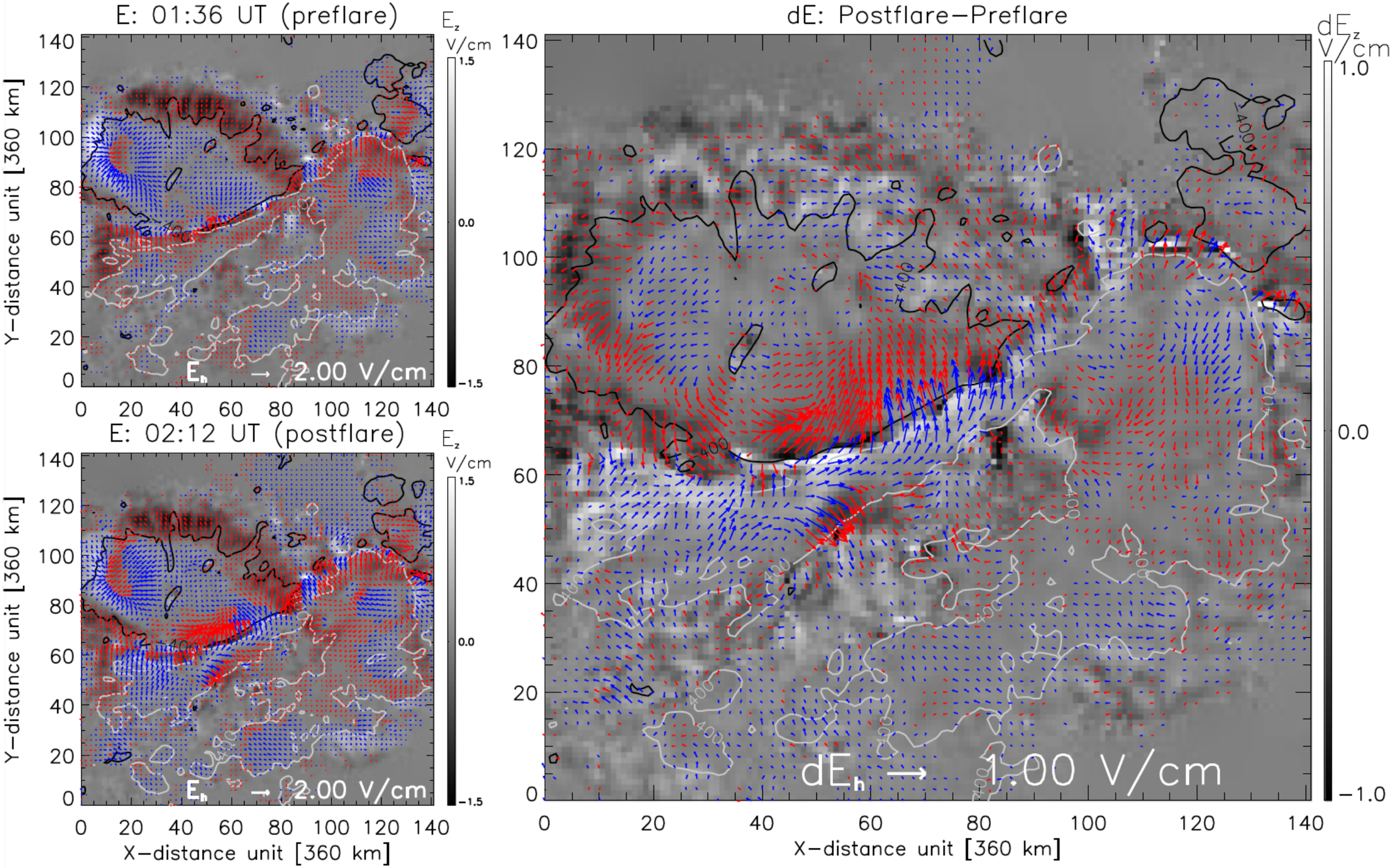

Pre- And Postflare Poynting Fluxes

Kazachenko et al. 2015

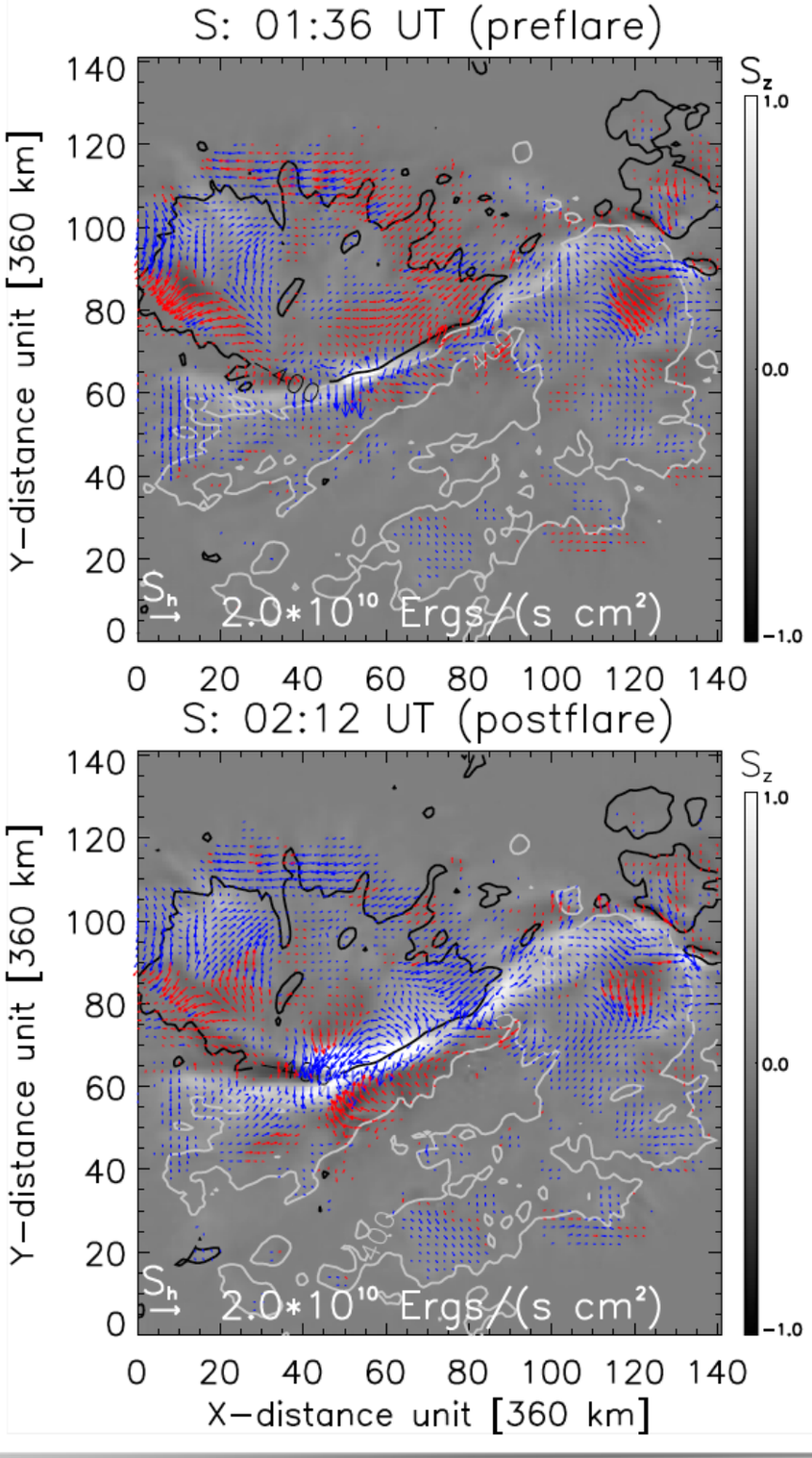

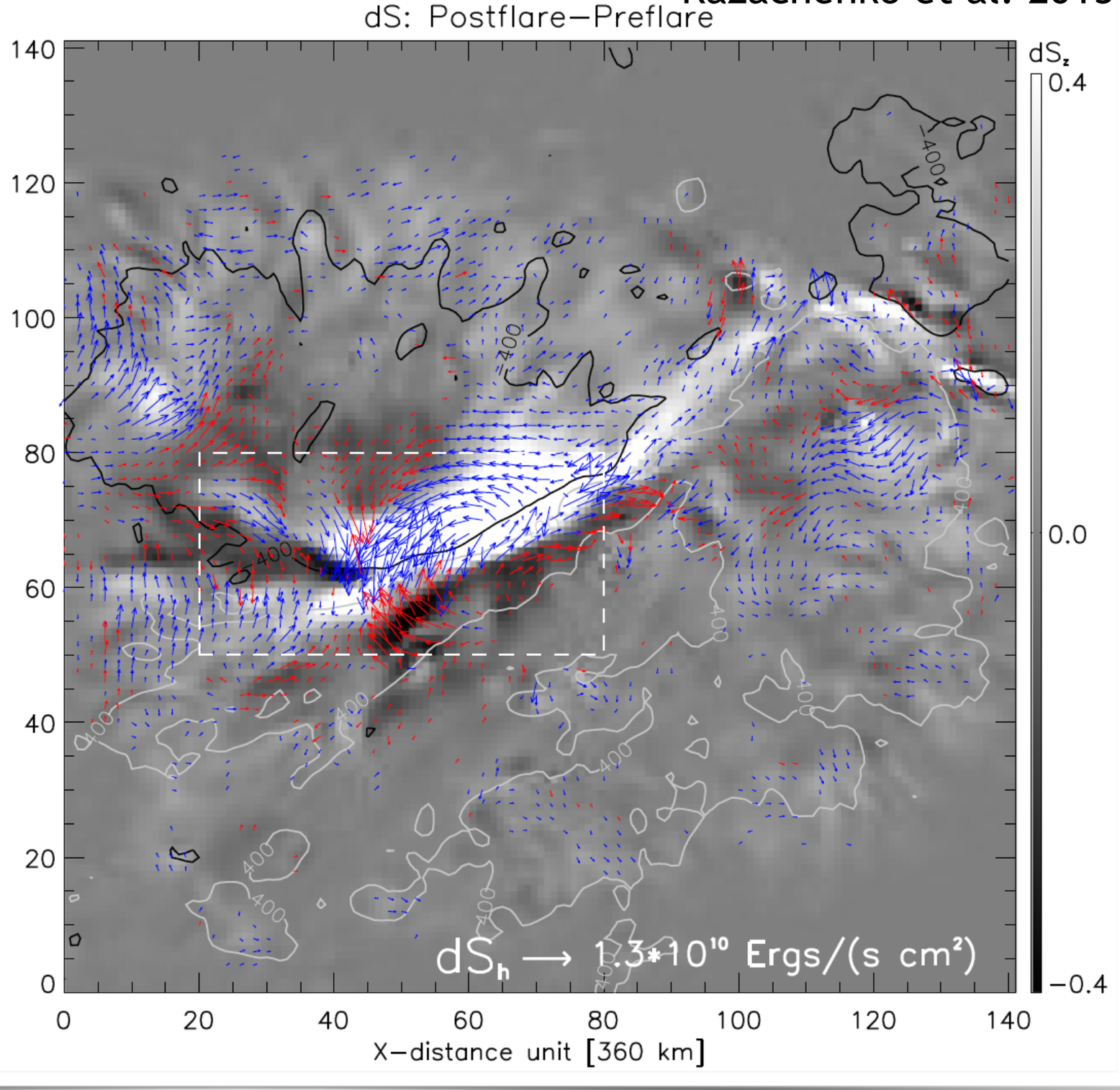

Pre- and post- flare properties: Bz, Bh, Eh, Sz

preflare

postflare

both

B_z ~ [-2; 2] KG; does not exhibit any significant changes.

B_h ~[0-2.5] KG; increases at the PIL by several hundred gauss (see Bh-panel, right column).

E_h~ [0-1.5] V/cm; increase close to PIL by up to 0.5 V/cm and by almost 1 V/cm in some locations away from the PIL

S_z~ [0-2.0] 10^{10} Ergs $cm^{-2}s^{-1}$
Increases from 1.25 to 2.25 *10^9 Ergs cm-2s-1

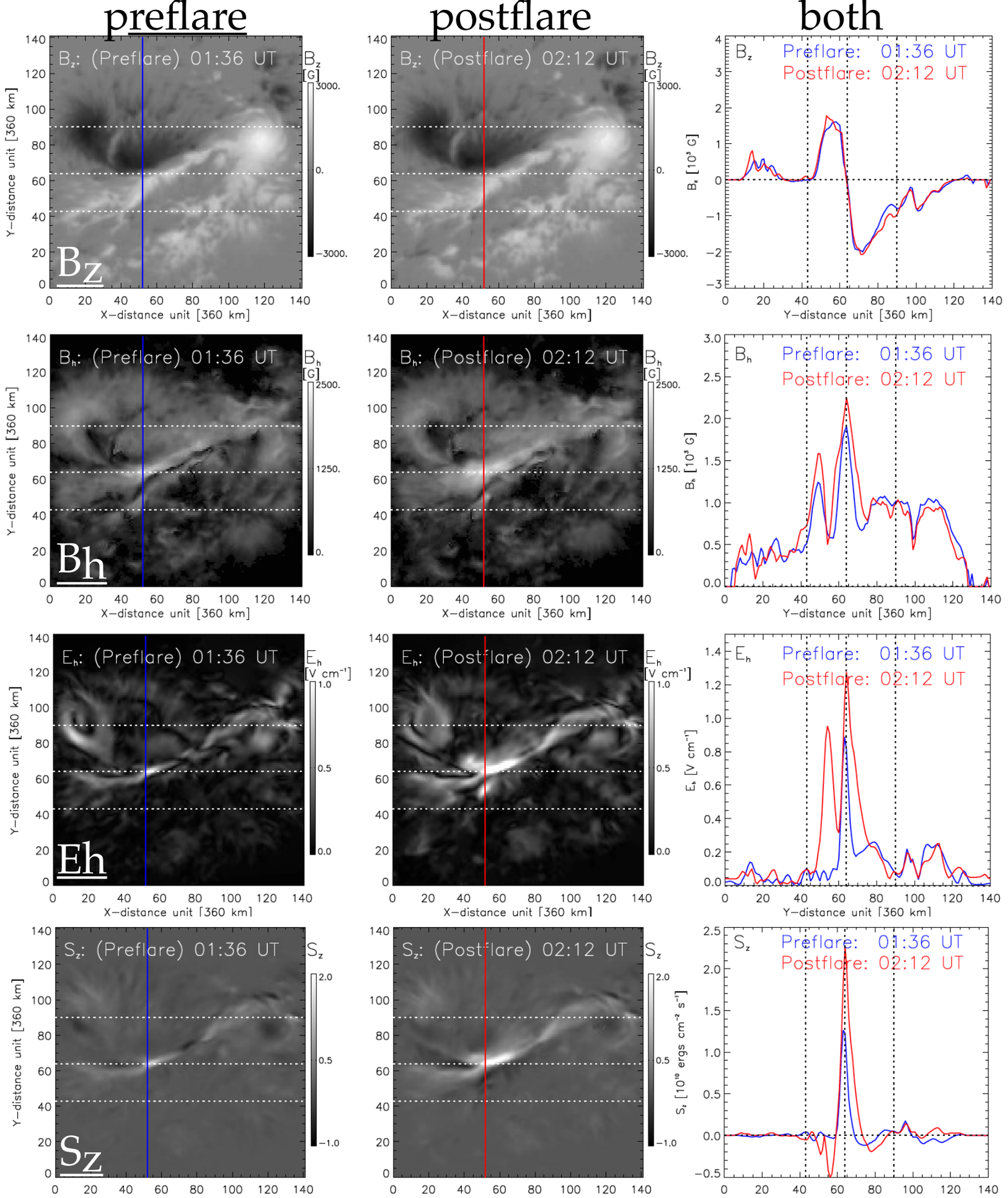

What aspects in the **E** inversion and the HMI observations affect the total magnetic energy Em?

$$E_m(t) = \int_0^t dt' \int_A dA \; \frac{1}{\mu_0} (\mathbf{E} \times \mathbf{B}) \cdot \hat{\mathbf{z}}$$

1. How does omission of the non-inductive component in the E-field inversion affects the energy flux?
2. How does the Doppler velocity inversion affect the energy flux?
3. How does the noise in the magnetic fields measurements affect the energy flux?
4. How does the HMI cadence (e.g. 2 min vs 12 min) affect the energy flux?

All these aspects demonstrated using AR 11158 as an example.

Courtesy Erkka Lumme

Ignoring Non-inductive E-fields: Does It Affect Total Energy? Yes!

If **E** is non-inductive, i.e.

$$c\mathbf{E}_{\mathbf{h,non-ind}} = -\nabla_h \psi$$

Then this E does not affect dB_r/dt

$$c\nabla \times \mathbf{E}_{\mathbf{h,non-ind}} = -\frac{dB_r}{dt} = 0$$

But it does affect the energy flux!

Cheung et al. 2012

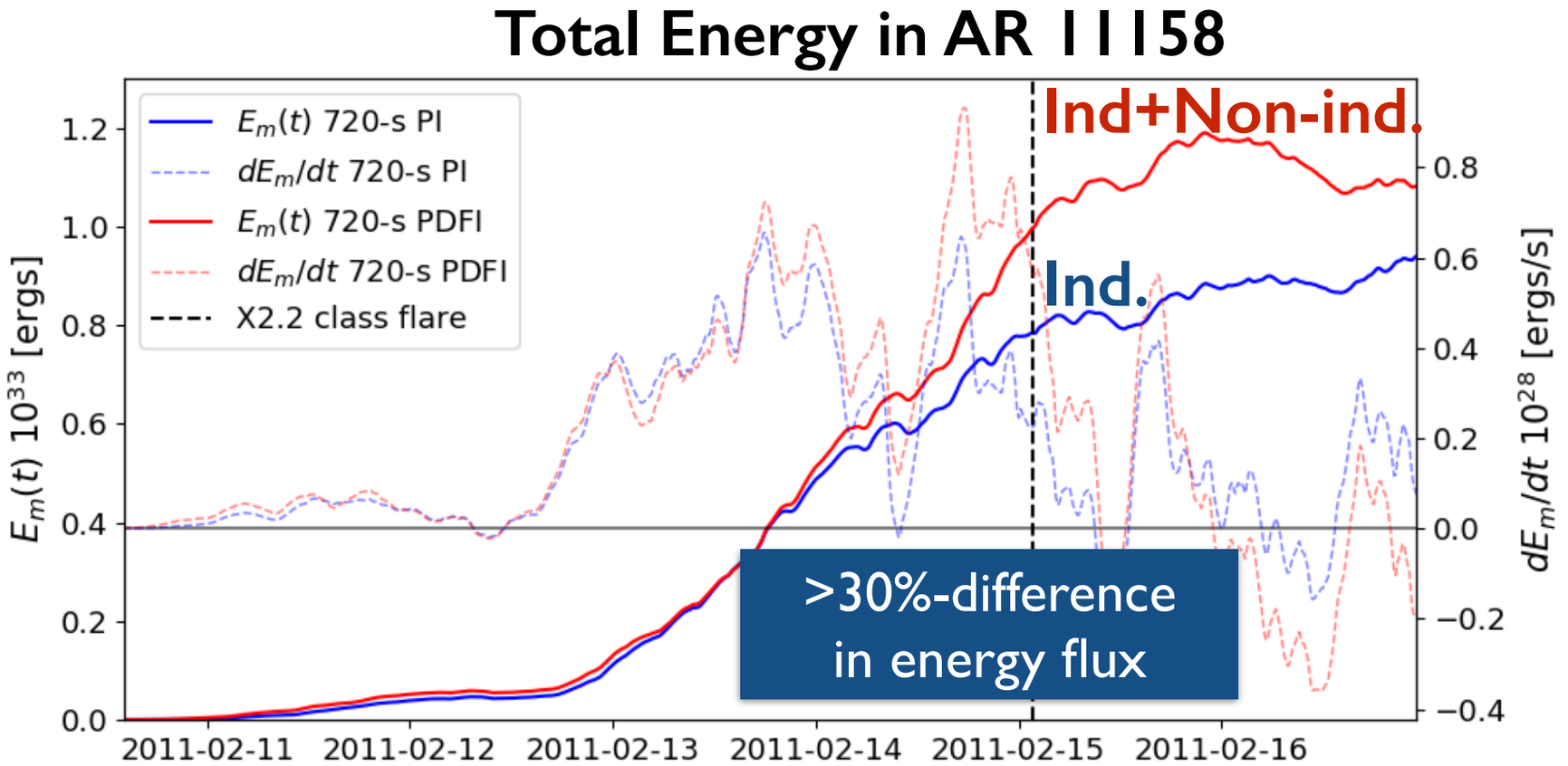

Courtesy Erkka Lumme

Type of Doppler velocity inversion and the energy flux

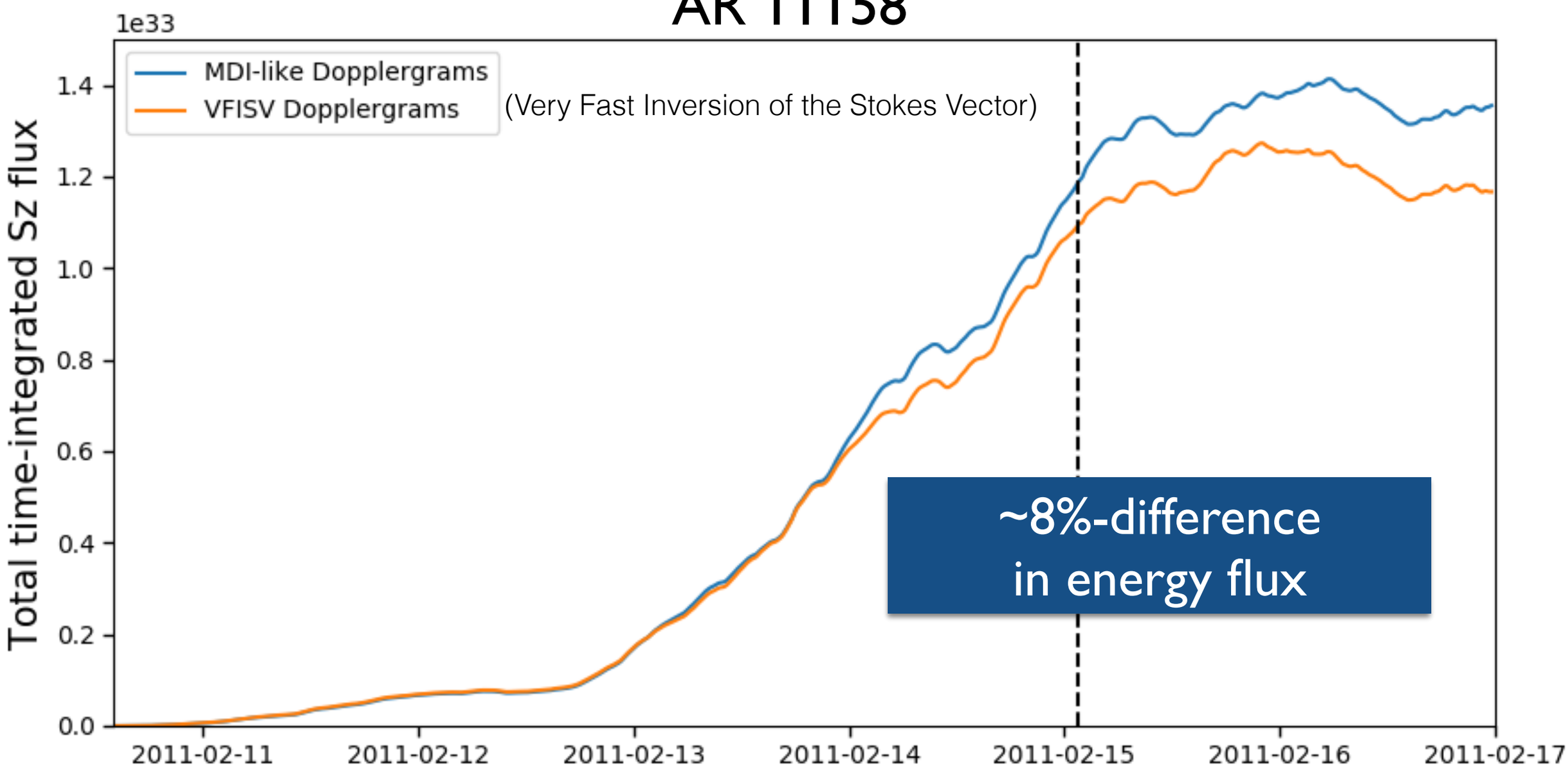

Courtesy Erkka Lumme

HMI noise and the energy flux

Estimated HMI noise levels in Bx, By and Bz as a function of time

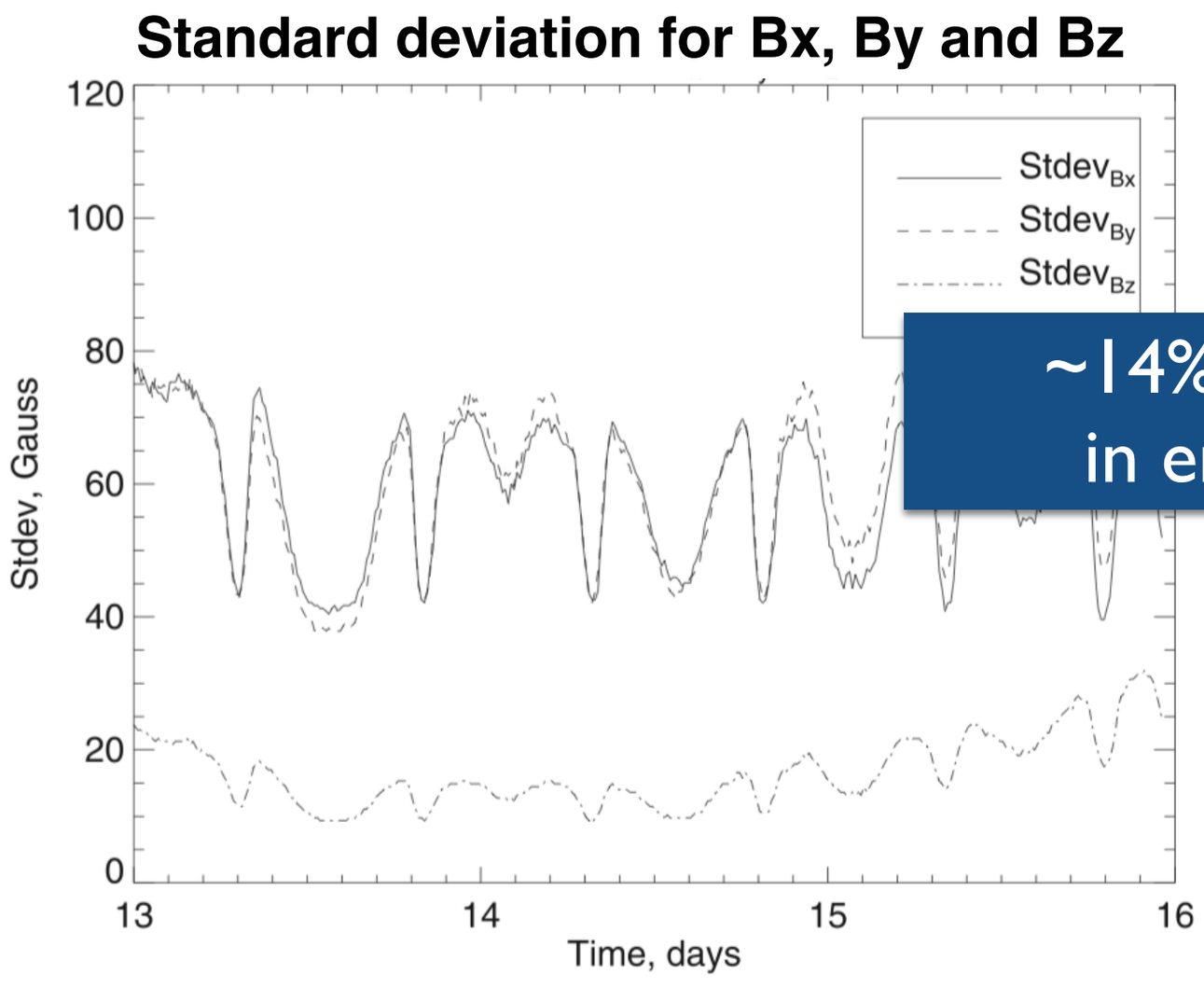

Pixel-by-pixel comparison between perturbed and non-perturbed E-field (x-component)

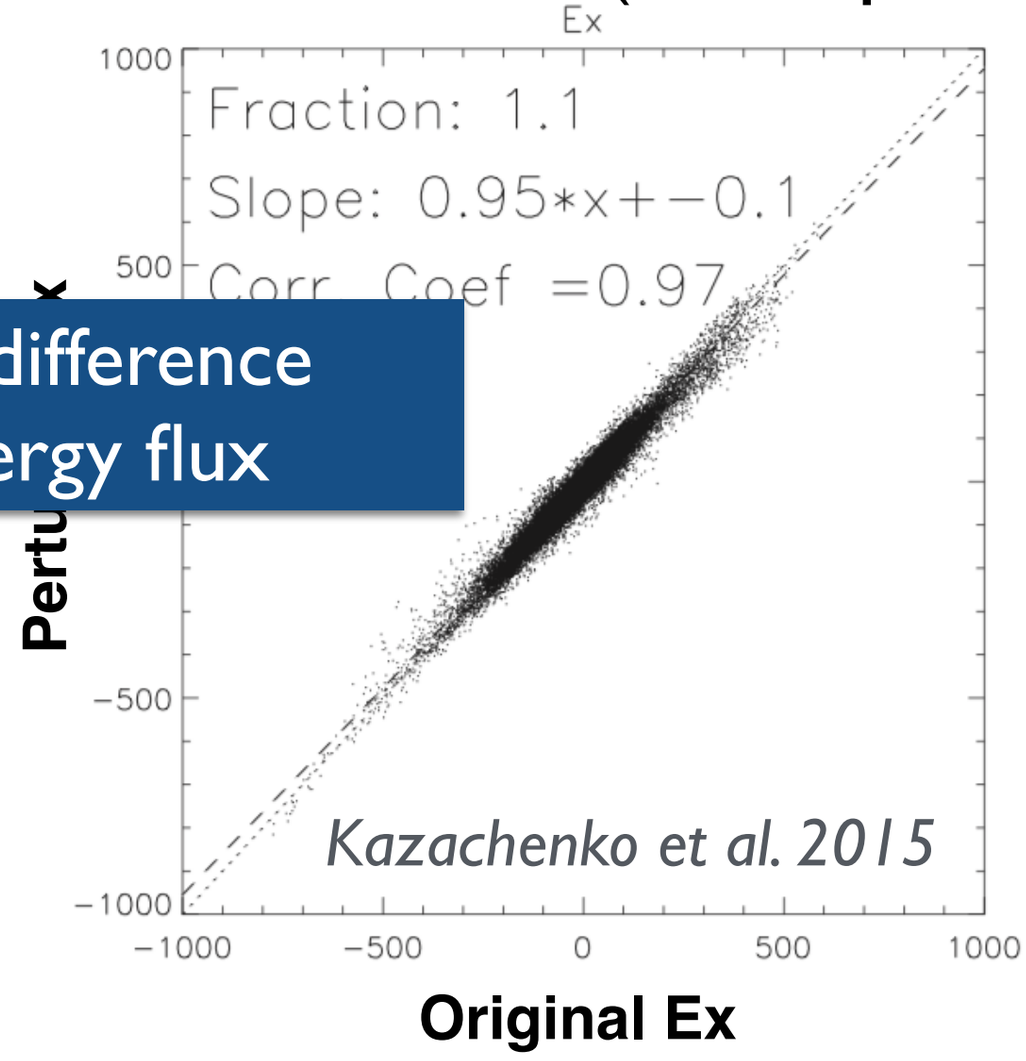

~14%-difference in energy flux

[14,13,18,14]%-difference in [Ex, Ey, Ez, Sz]

HMI cadence and the **PDFI** energy flux

Is the available input data for the inversion (e.g. SDO/HMI) of sufficient cadence (e.g., Leake et al., 2017)?

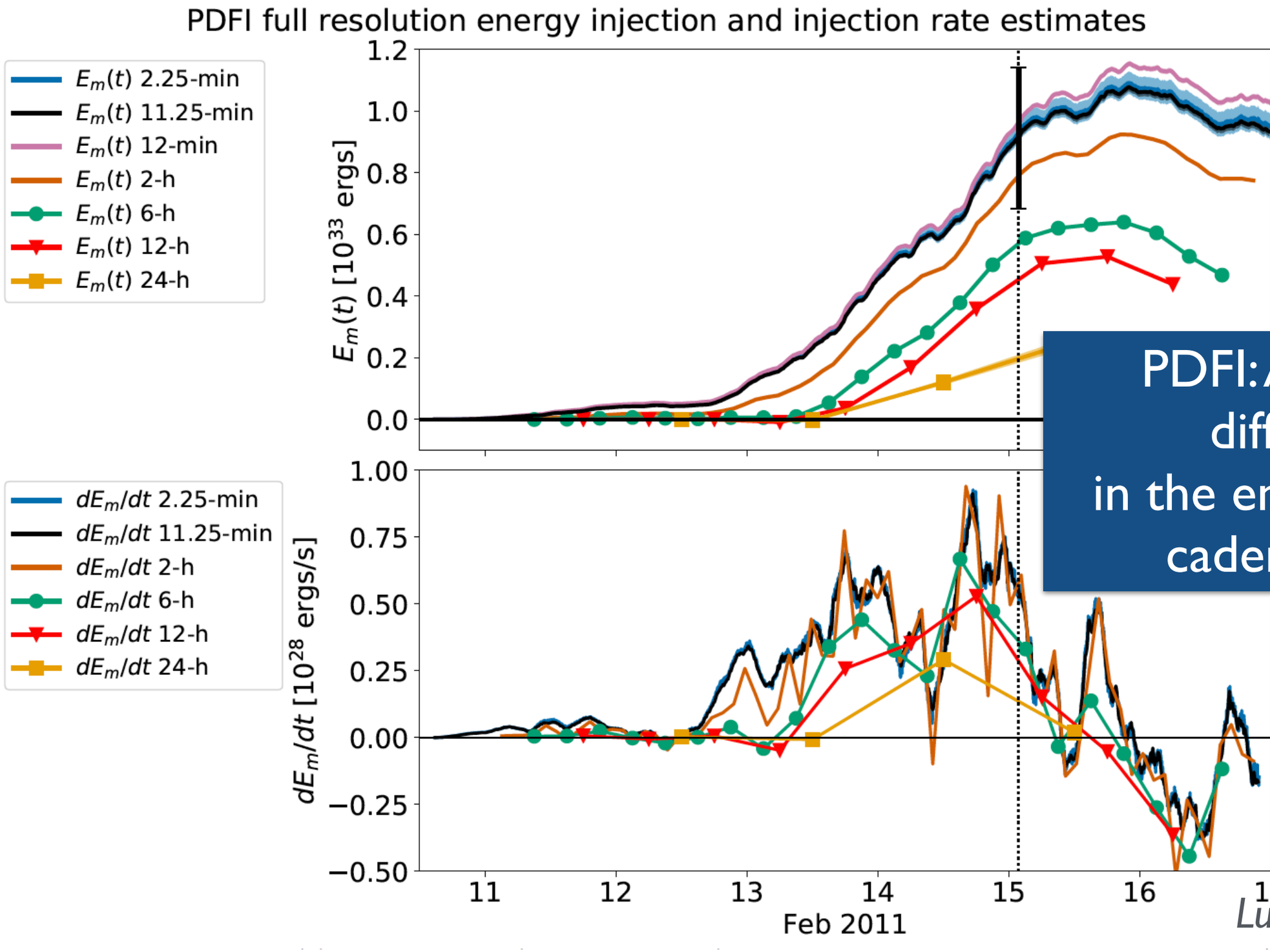

PDFI: Almost no difference in the energy flux till cadence of 2h

Lumme et al. 2019

HMI cadence and the **DAVE4VM** energy flux

$$\mathbf{E} = -\mathbf{V}_{DAVE4VM} \times \mathbf{B}$$

$$E_m(t) = \int_0^t dt' \, \frac{dE_m}{dt'} = \int_0^t dt' \int_A dA \; S_z = \int_0^t dt' \int_A dA \; \frac{1}{\mu_0}(\mathbf{E} \times \mathbf{B}) \cdot \hat{\mathbf{z}}$$

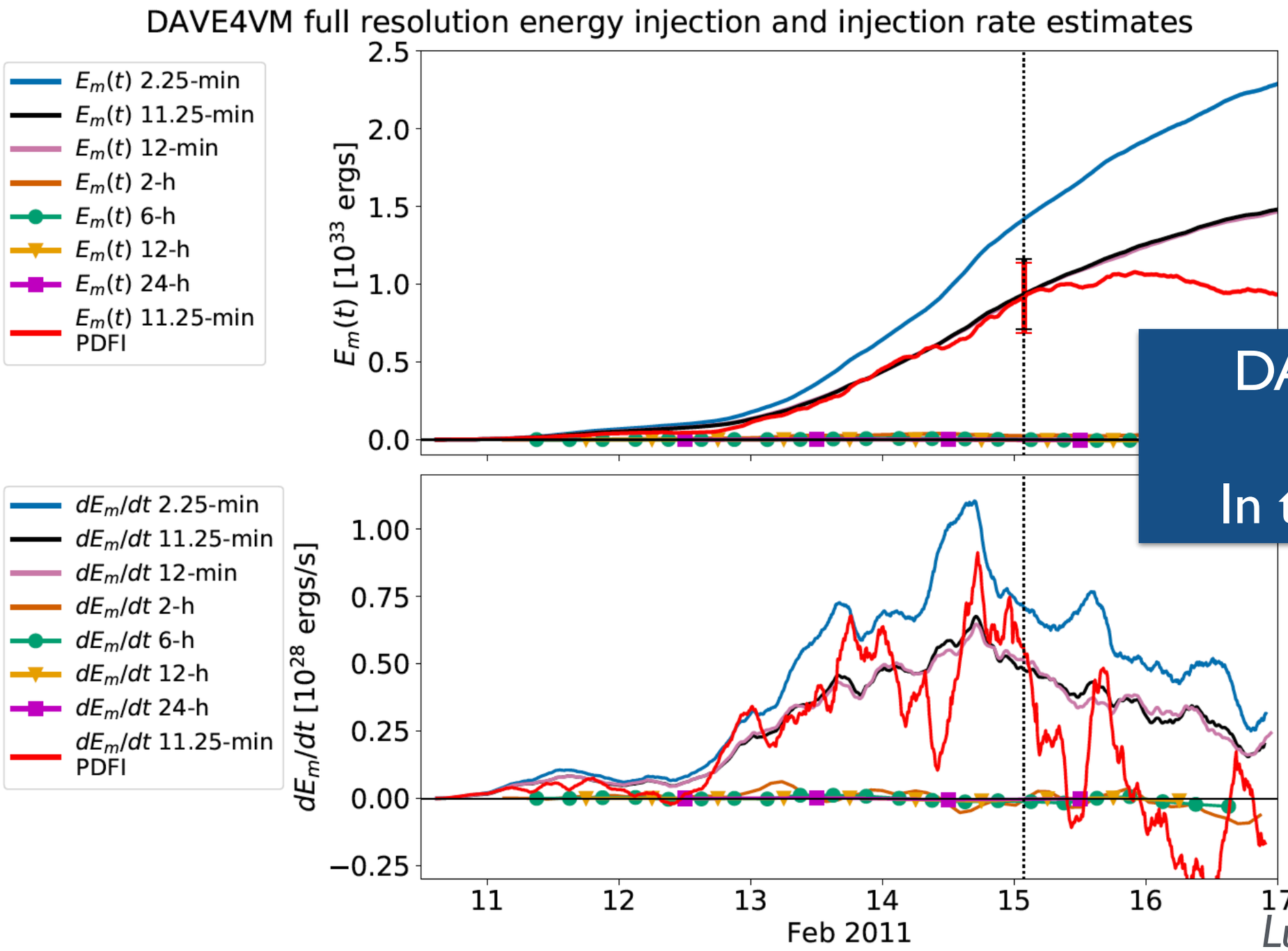

DAVE4VM: ~50% difference
In the energy flux

Lumme et al. 2019

HMI cadence and the **PDFI** helicity flux

$$H_R(t) = \int_0^t dt' \, \frac{dH_R}{dt'} = -2 \int_0^t dt' \int_A dA \, (\mathbf{A}_p \times \mathbf{E}) \cdot \hat{\mathbf{z}}$$

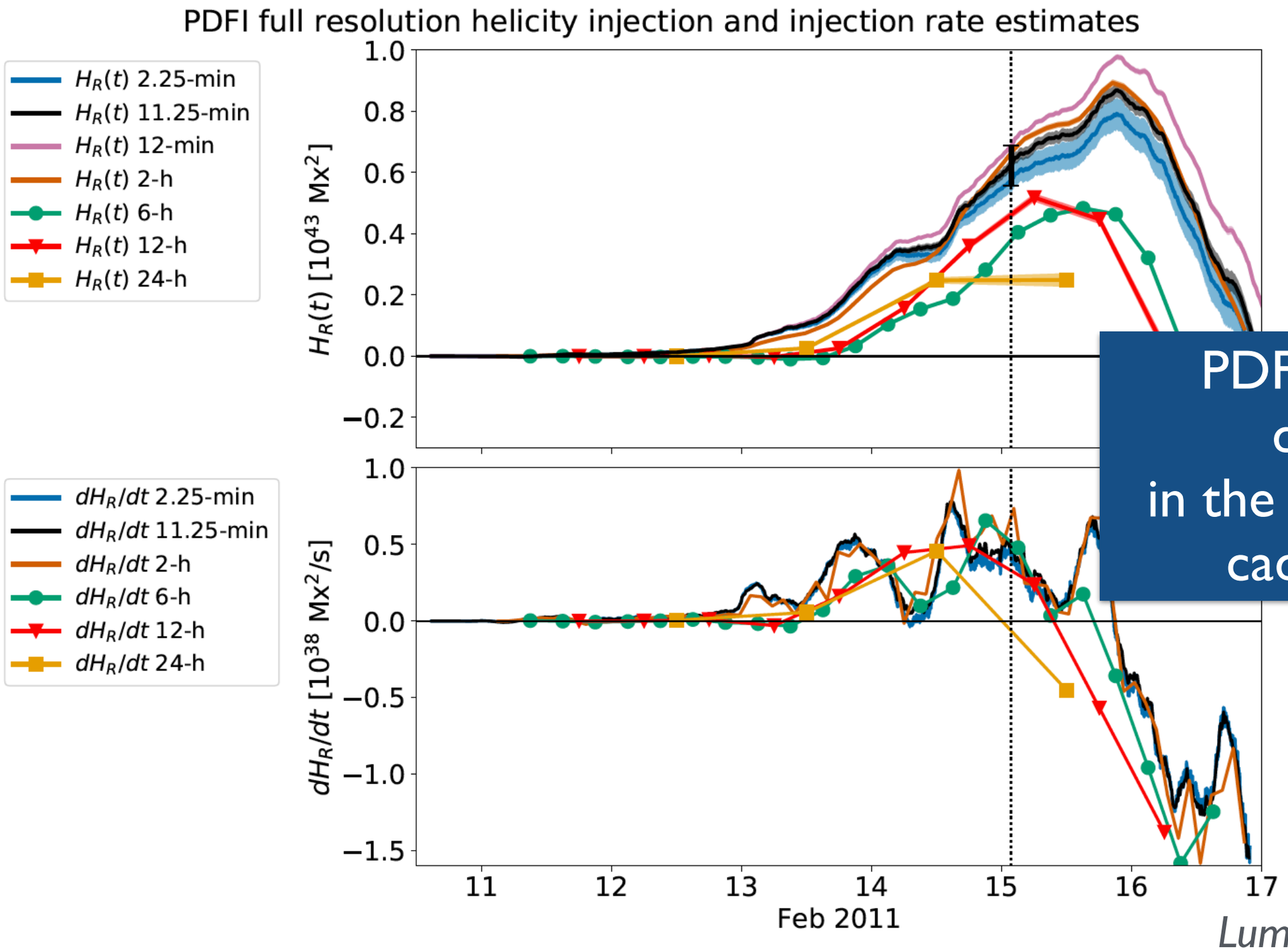

PDFI: Almost no difference in the helicity flux till cadence of 6h

Lumme et al. 2019

HMI cadence and the **DAVE4VM** helicity flux

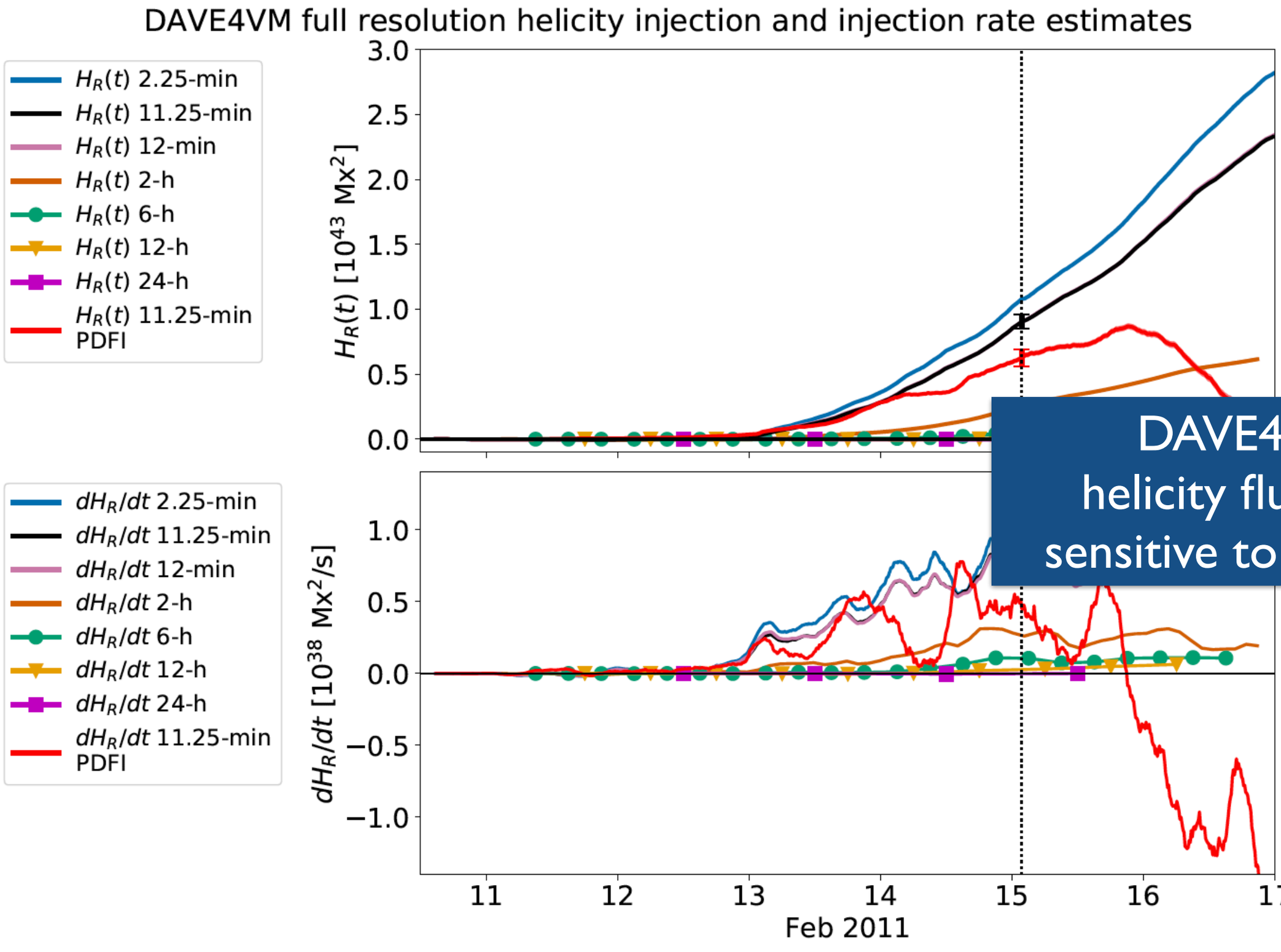

DAVE4VM:
helicity flux very sensitive to cadence

Lumme et al. 2019

What aspects in the **E** inversion and the HMI observations affect the AR11158 **energy fluxes**?

1. How does omission of the non-inductive component in the E-field inversion affect the total energy flux? >**30%**
2. How does the noise in the magnetic fields measurements affect the energy flux? **~14%**
3. How does the HMI cadence (e.g. 2 min vs 12 min) affect the energy flux? **tiny for PDFI, worse for e.g. DAVE4VM**

Take home message:

1. Non-inductive **E**-components are important
2. HMI input data should be carefully calibrated

PDFI: Importance of the grid choice

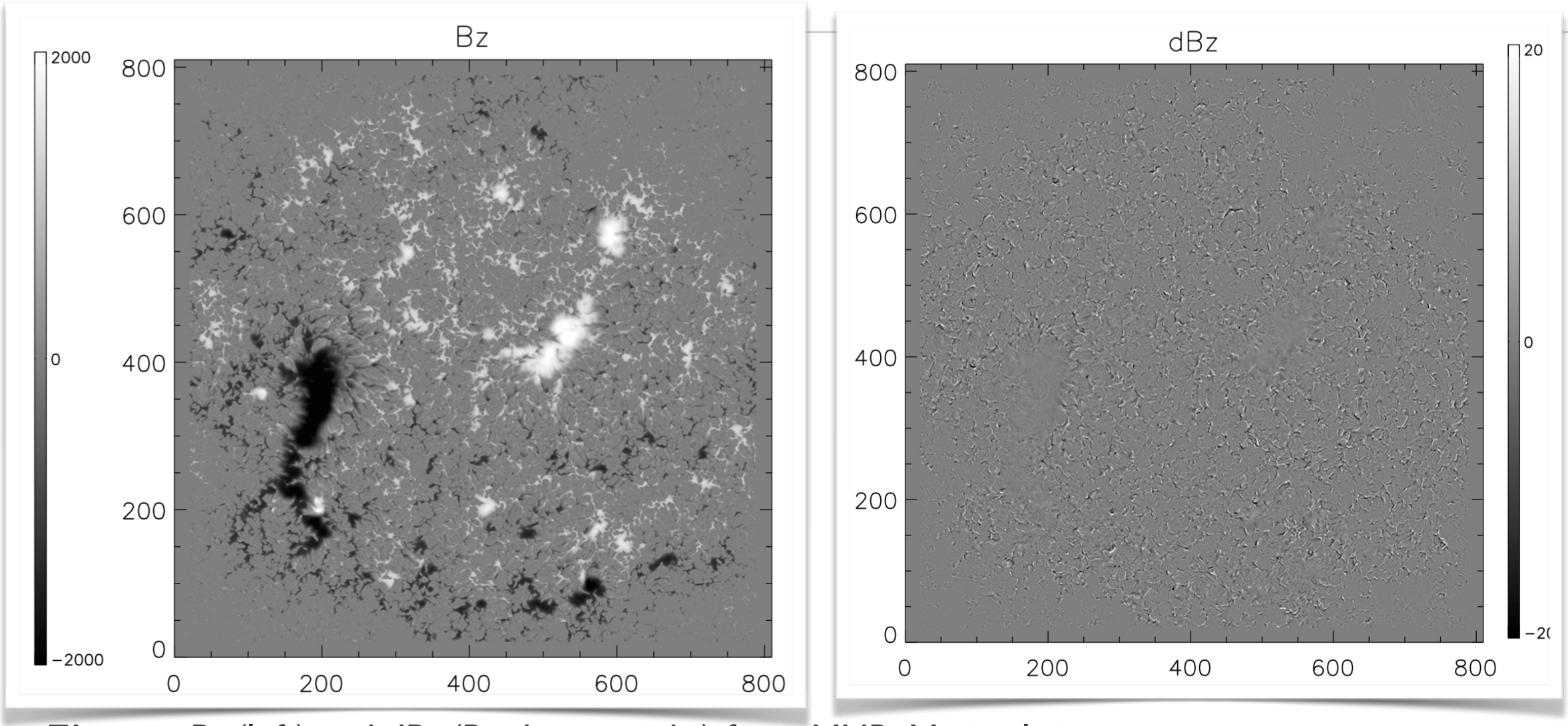

- **Figure:** B_z (left) and dB_z (B_z change, right) from MURaM simulations
- **Problem:** Using centered grid we found discrepancies between MURaM **E** and **E** from PDFI inversions.
- **Cause:** small-scale, highly structured fields are sensitive to numerical formalism.
- **Solution:** go from central to staggered grid.

PDFI: Importance of the grid choice

PDFI looks for solutions E that satisfy Faraday's Law:

$$\frac{\partial \boldsymbol{B}}{\partial t} = -(\nabla \times c\boldsymbol{E}),$$

In large-scale **B** structures, e.g. ARs, derived **E** satisfy this condition very well

However, when we deal with weaker Es, especially on smaller spatial scales, there is some scatter

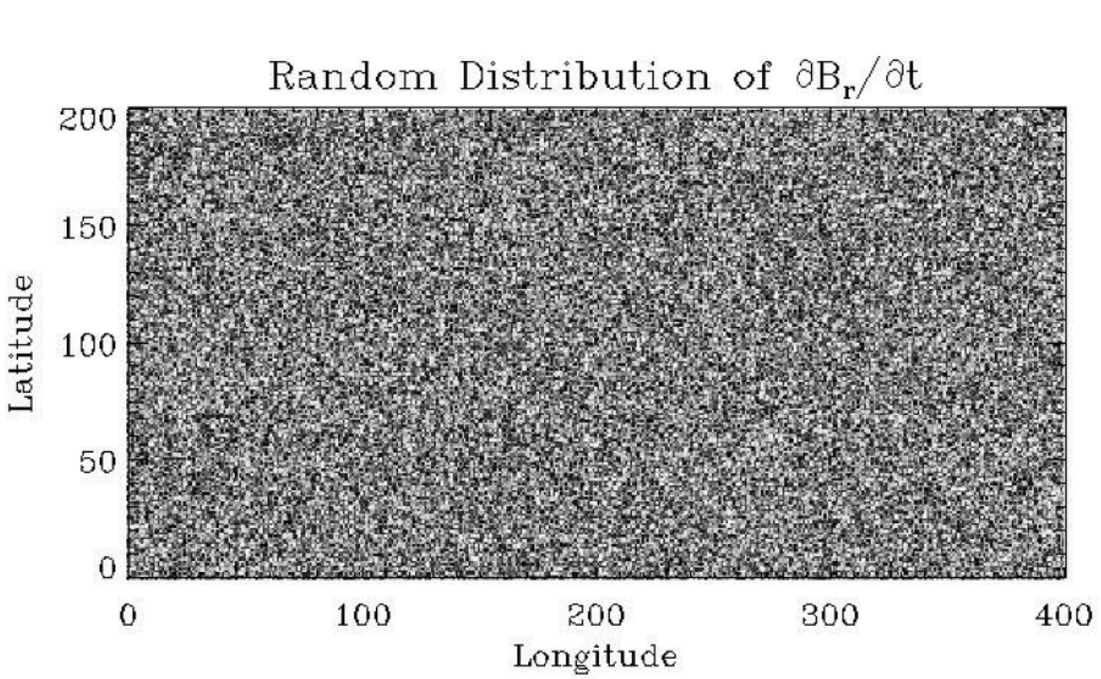

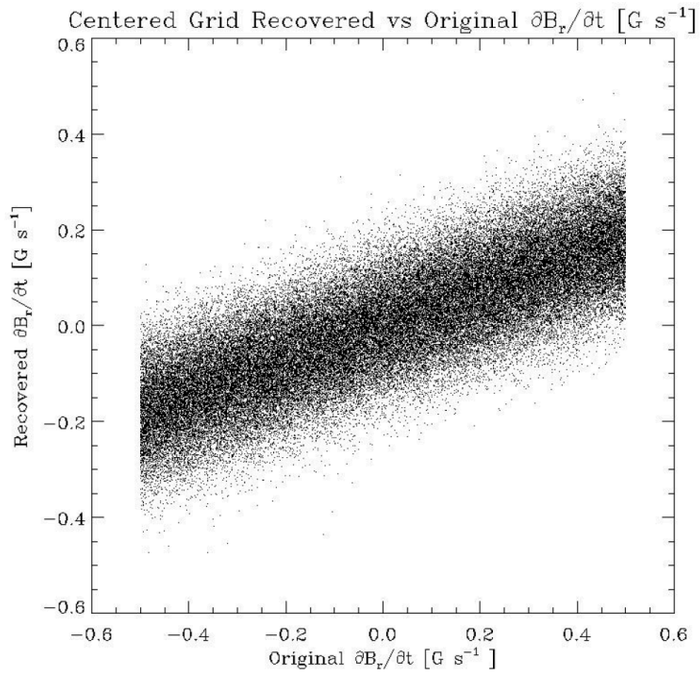

Recovered dB/dt (from derived ***∇*** *x E) vs. original dB/dt*

Why? Due to use of centered grid that is not fully consistent: d (d/dx) /dx ≠ d^2 /dx

Solution: need a fully consistent grid! Staggered Yee grid!

PDFI: Importance of the grid choice

Solution: Rewrote PDFI from centered to staggered grid, see Fisher et al. 2020.

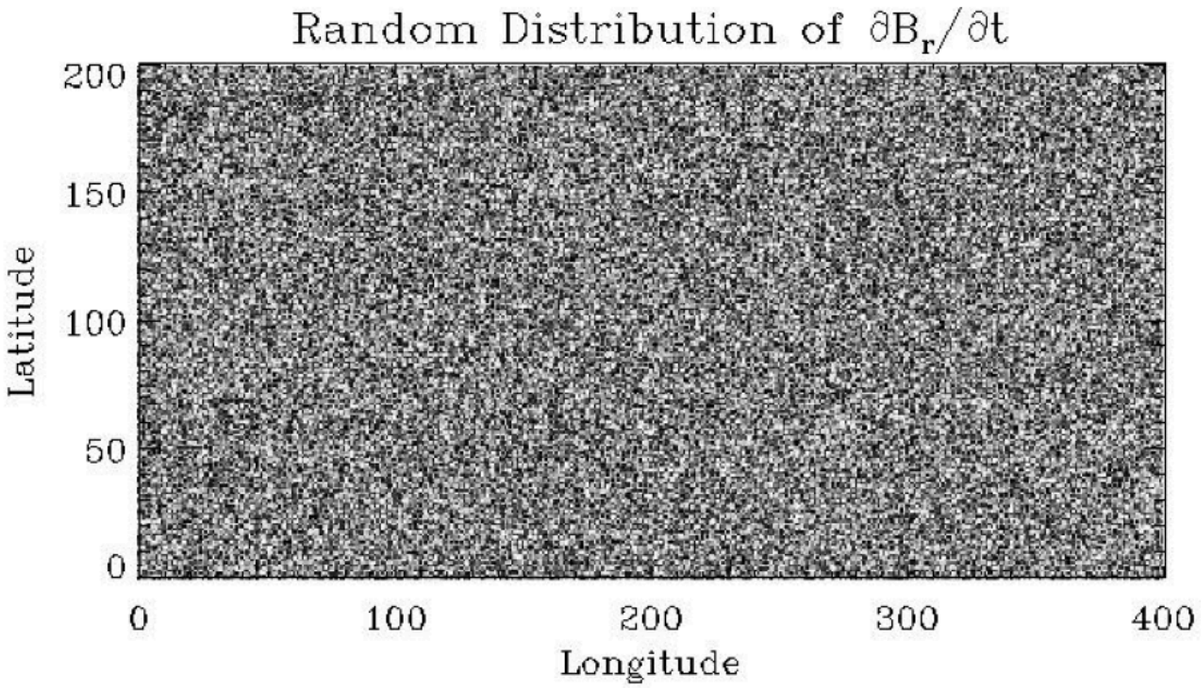

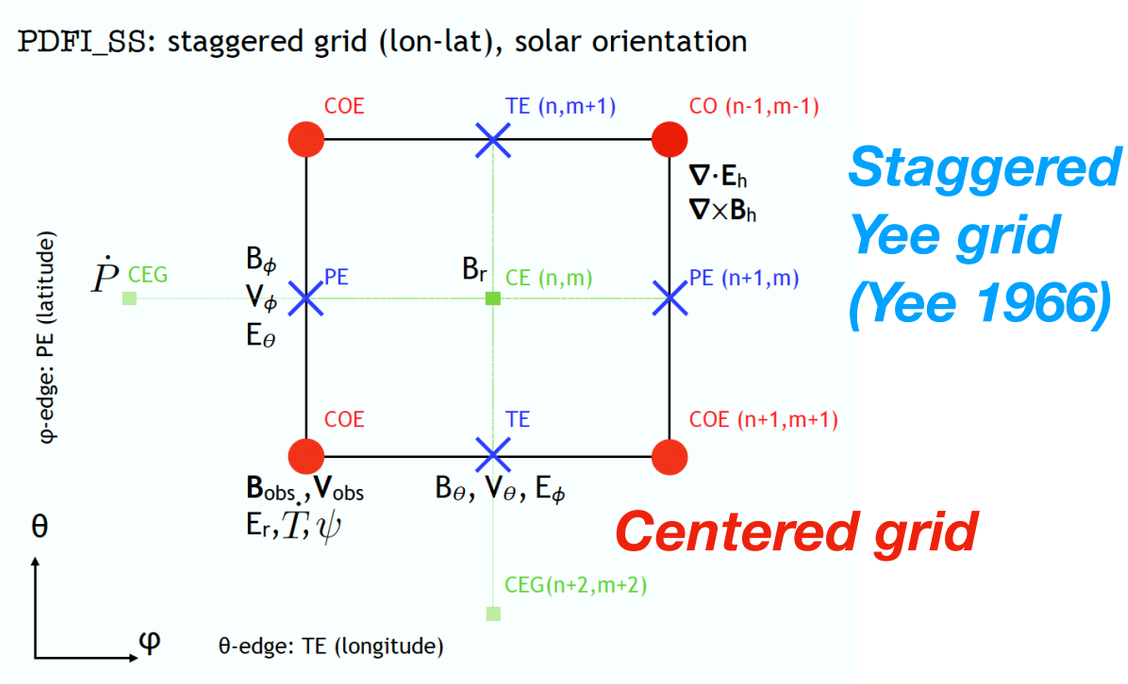

Staggered Yee grid (Yee 1966)

Centered grid

*Centered grid (**red dots**): Recovered dB/dt (from derived ∇ x E) vs. original dB/dt*

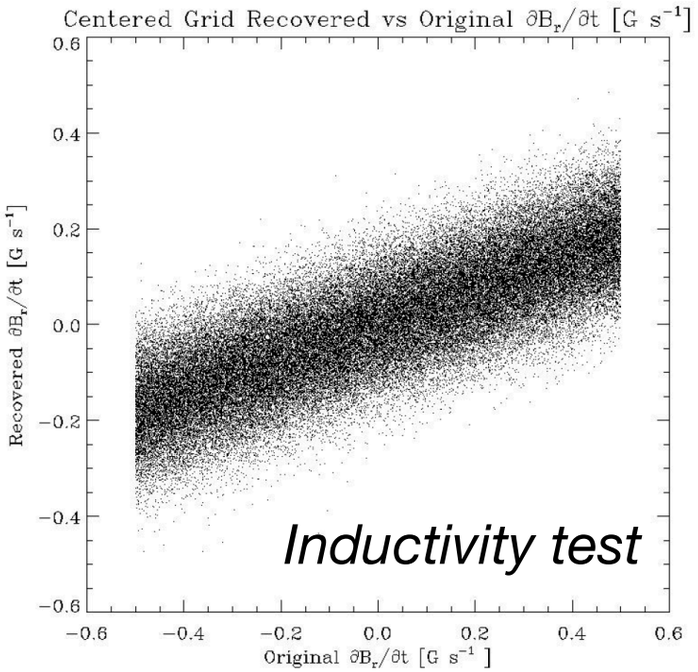

Should be a straight line for perfectly inductive E.

*Staggered grid (**blue crosses**) Recovered dB/dt (from derived ∇ x E) vs. original dB/dt*

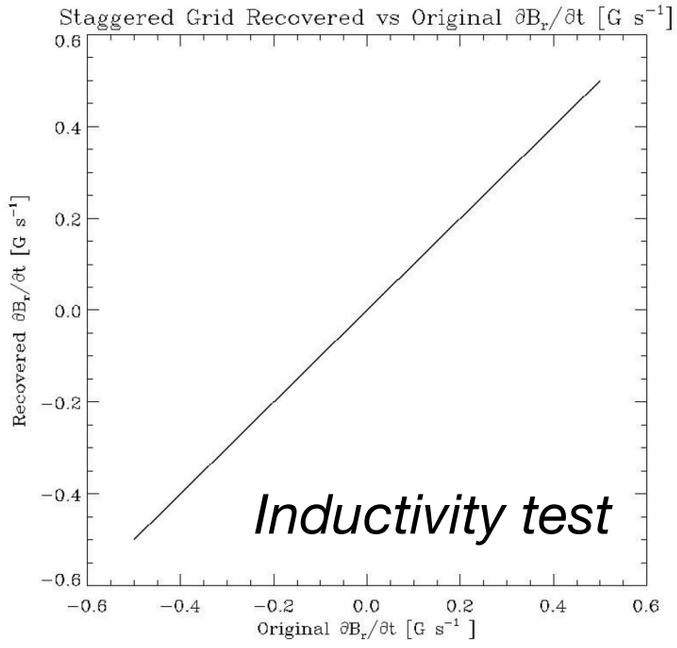

Fisher et al. 2020

Current status of PDFI

- Summary: Physics-based method to derive E from B and Doppler V.
- Validation: Tested using ANMHD test simulations; Excellent performance compared to other methods. Need additional tests with more realistic datasets, ANMHD is too simplified.
- Advantages: Currently the only method that uses both Doppler V and B (important for emergence); Solves induction equation precisely without minimization. Good for data-driving applications.
- Coordinates system: Works for spherical/Cartesian coordinates
- Grid: Could be used with centered or staggered grids.
- Open source: Since 2019, available for public use. PDFI Electric fields for HMI/SDO B-fields HARPs are available through JSOC.
- Language: Fortran-90. Python wrappers are still being tests.
- More details: Fisher et al. 2020 paper, ApJS (just accepted).

Lately a completely new approach has been used to derive velocity fields

Machine Learning approaches to find plasma flows from intensity maps

Main idea: Instead of solving equations, train a V-solver on intensity maps from simulations (**note:** use I to get V, not B);

Asensio-Ramos, 2017: introduced DeepVel;

- Construct a convolutional deep neural network DeepVel.
- Train DeepVel on Stein & Nordlund (2012) magneto-convection simulations continuum intensity (Ic) output: V, Ic known; dt=30s, ds=48km;
- Validate DeepVel on MANCHA Ic simulation output - good agreement.
- Apply trained network to IMaX/Sunrise Ic data (2009 9 June): ds= 39.9km; dt=33.25s to get Vh
- Compare with DeepVel and FLCT flows for IMaX Ic.

DeepVel: network validation

- Train network on one simulation (Stein & Nordlund, 2012) at τ=1.
- Apply trained network to other simulation (MANCHA) output;
- Pearson correlation coefficient varies from 0.75 to 0.85 for velocity field vector magnitude.

Validation at different heights

τ=1 τ=0.1 τ=0.01

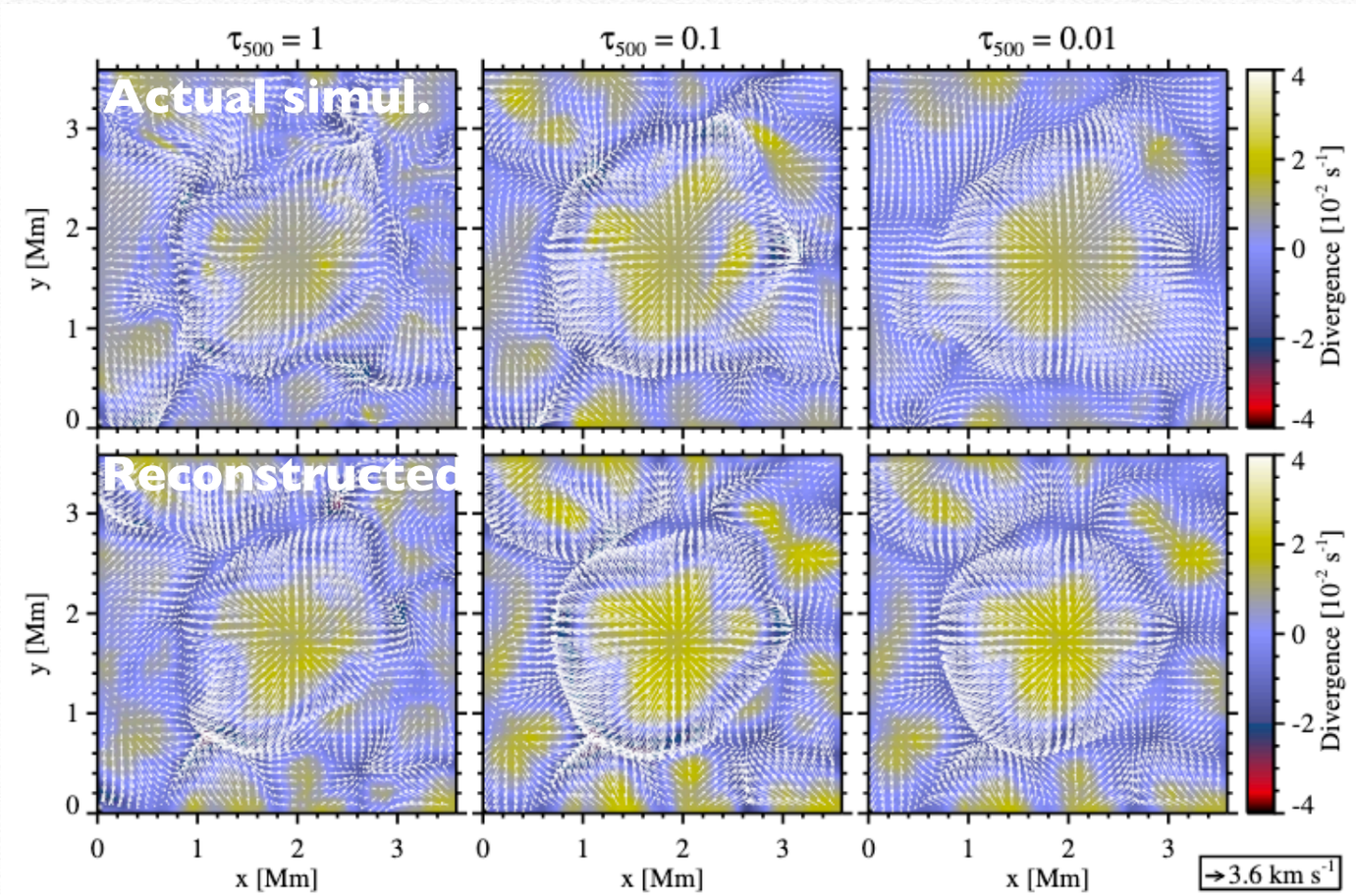

Fig. 2. Instantaneous horizontal velocity field (white arrows) and divergence maps (background images) at three heights in the atmosphere, corresponding to $\tau_{500} = 1, 0.1, 0.01$, for `MANCHA` (*upper row*) and `DeepVel` (*lower row*) velocities.

DeepVel Results: Reconstructed velocities for IMaX Ic observations

Obs. Ic

Reconstructed velocities at different heights

τ=1 **τ=0.1** **τ=0.01**

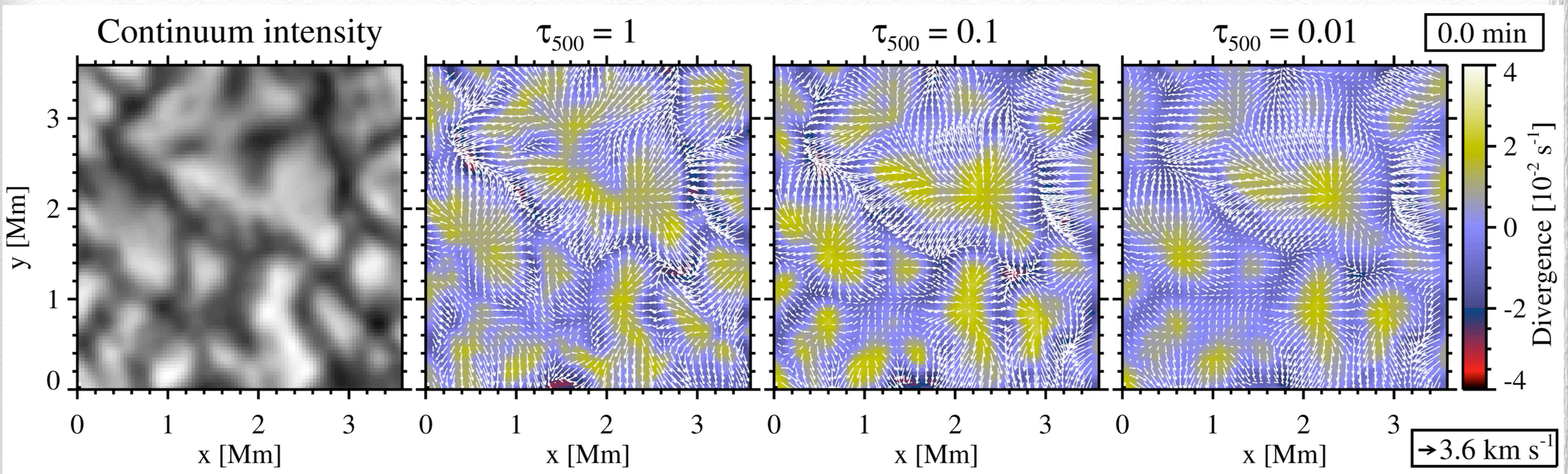

DeepVel Results: Reconstructed velocities for IMaX Ic observations

Obs. Ic

Reconstructed velocities

τ=1 **τ=0.1** **τ=0.01**

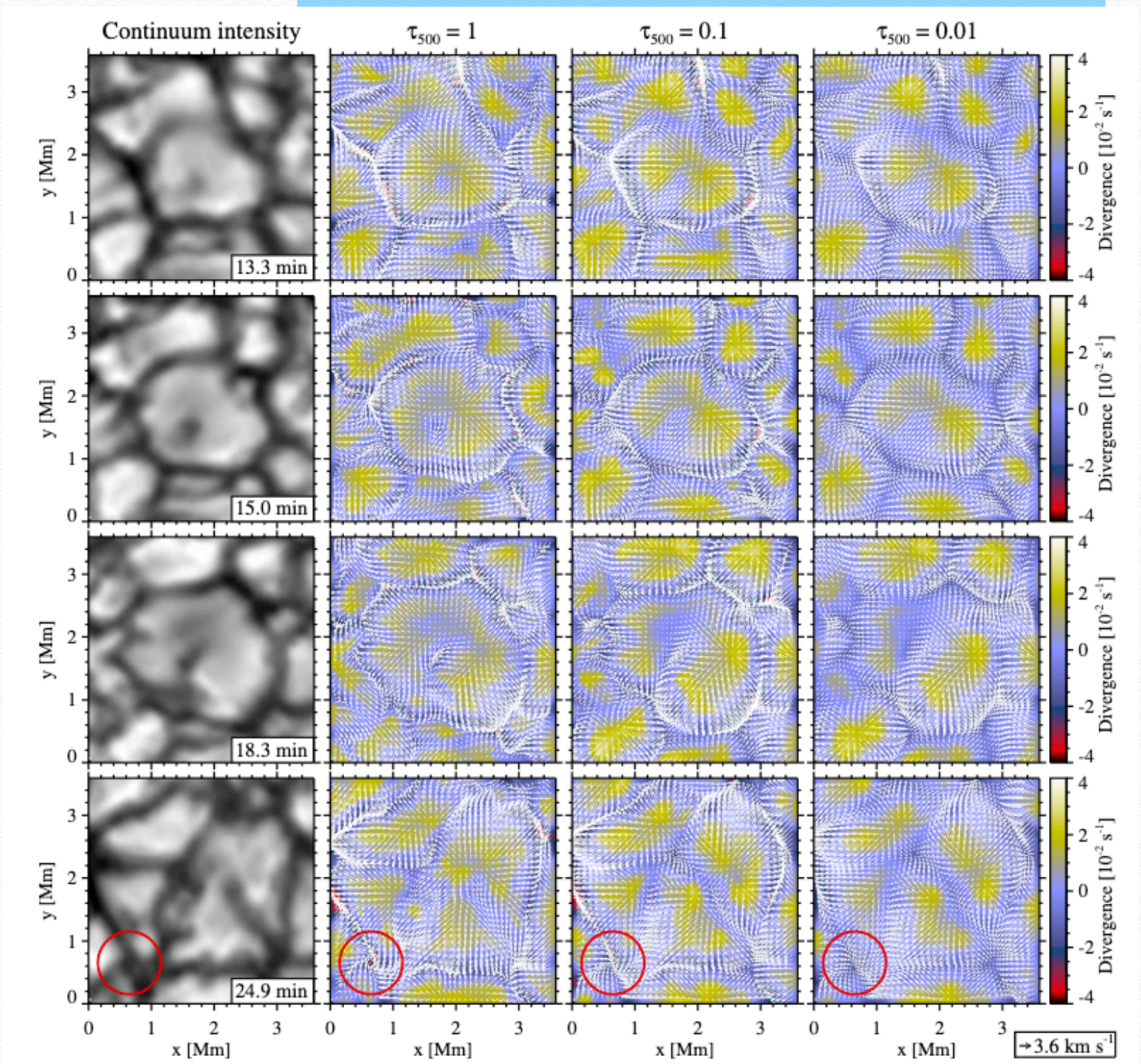

DeepVel: Reconstructed velocities for IMaX Ic observations: DeepVel vs. LCT

DeepVel: Vh

LCT: Vh

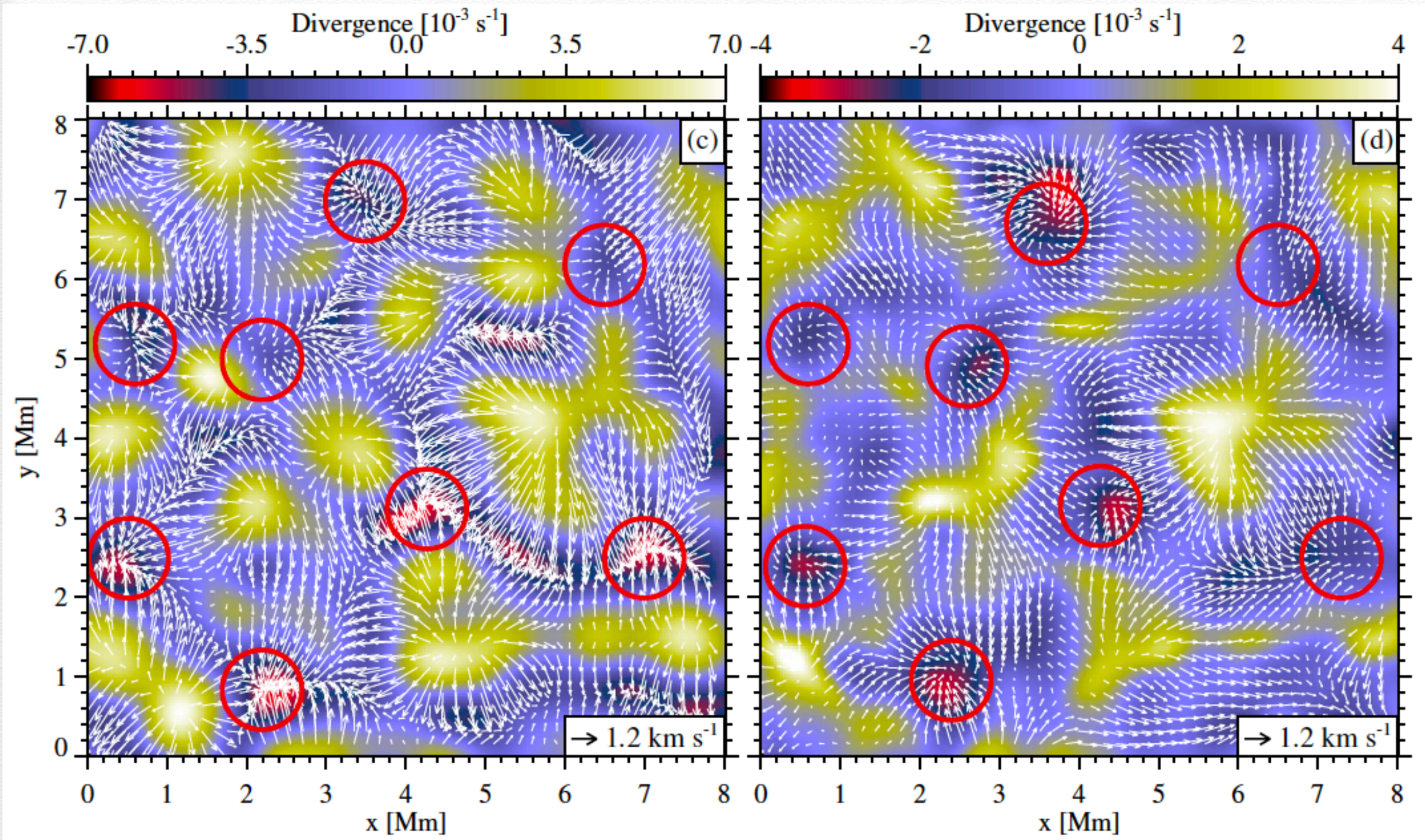

Conclusion: similar Vh from LCT and DeepVel: $|V_{h,DV}| > |V_{h,LCT}|$

Comparison of LCT, FLCT, CST and DeepVel horizontal velocity using intensity maps from simulations

- Tremblay et al. 2018: use outputs from Stein & Nordlund (2012) to train DeepVel
- Compare Vh from DeepVel with velocities derived with other methods

- Photosphere Ic from simulation

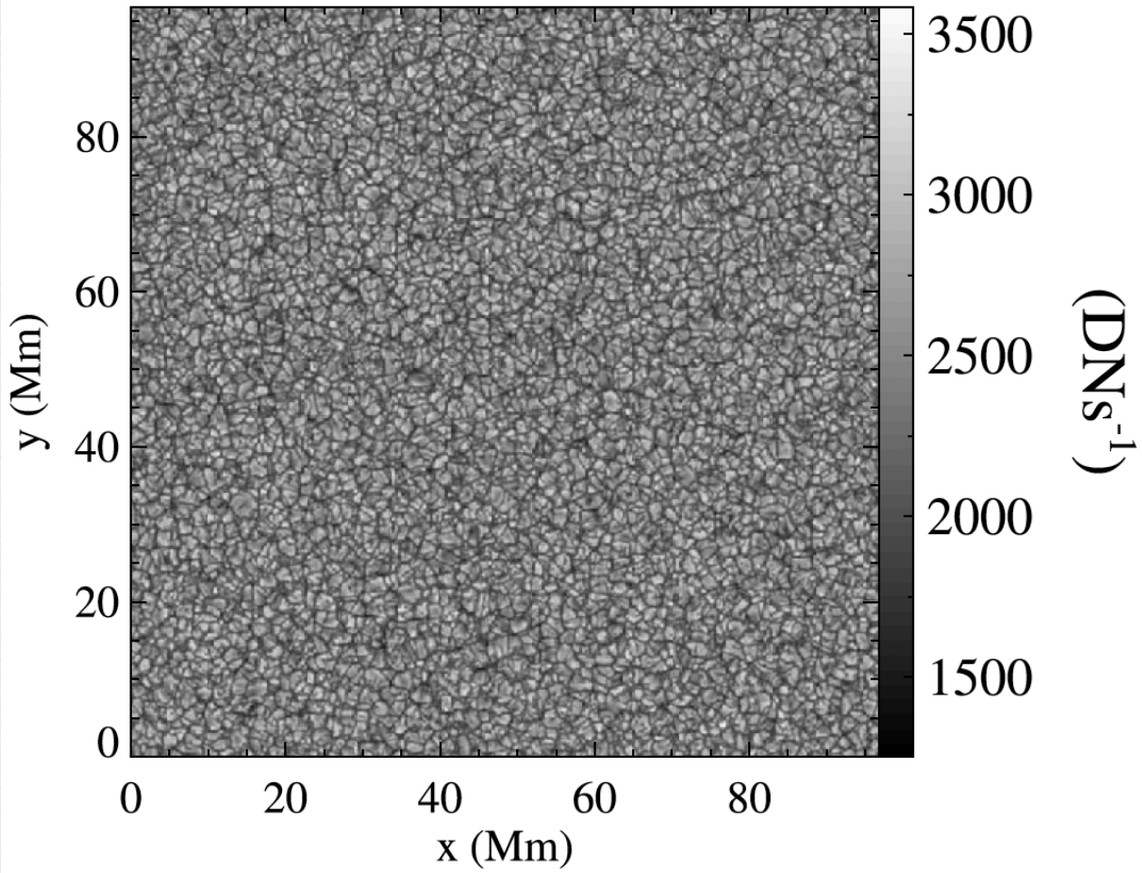

- Photosphere Vh from simulation

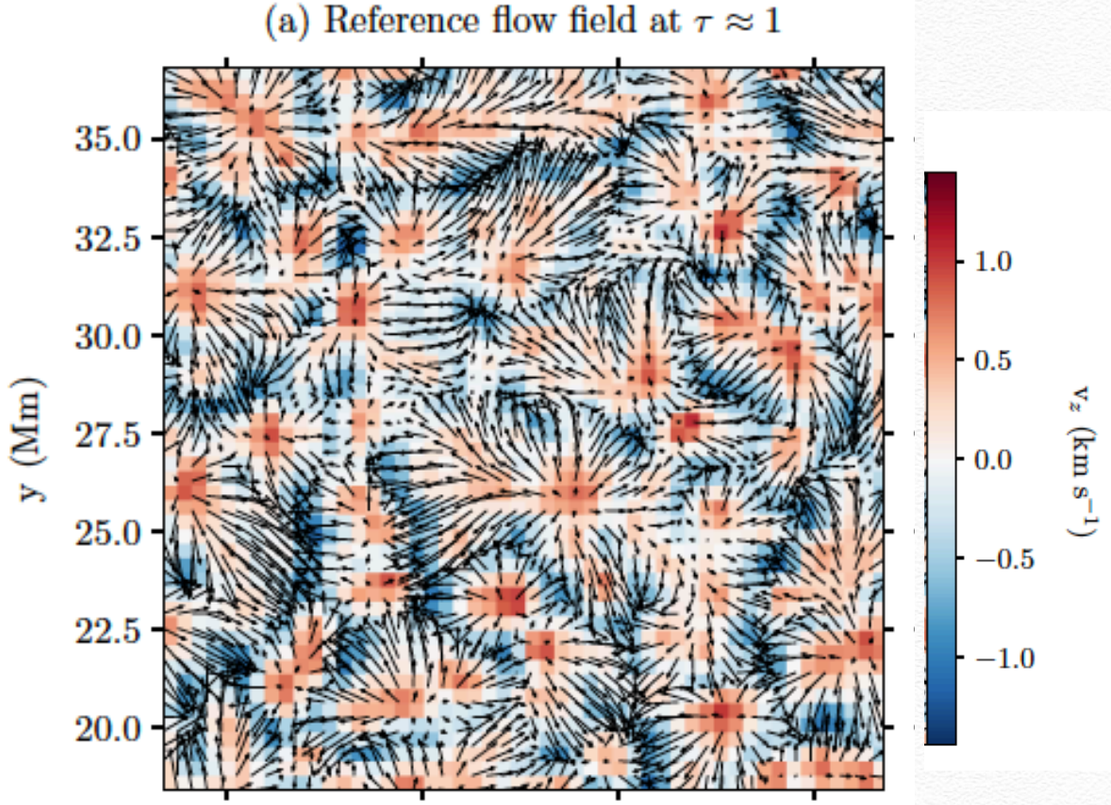

Courtesy Benoit Tremblay

Comparison of LCT, FLCT, CST and DeepVel horizontal velocity using intensity maps from simulations

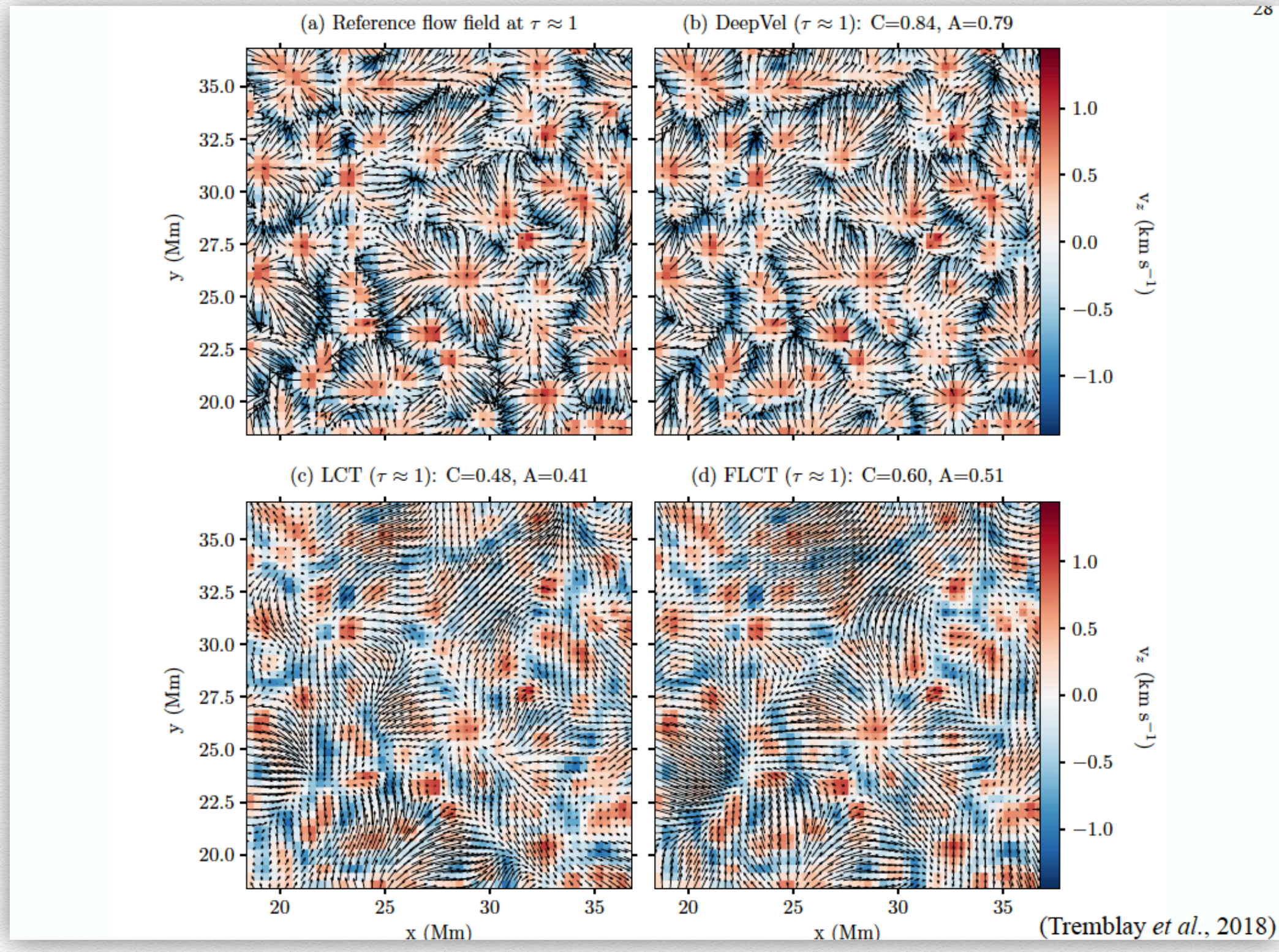

(Tremblay *et al.*, 2018)

Courtesy Benoit Tremblay

Test Set: Simulation Data

- **Kinetic energy E(k) power spectra:** $\frac{1}{2}\langle v_x^2 + v_y^2 \rangle = \int_0^\infty \mathrm{E(k)dk}\,.$

Spatial scales:

Granular (G),

Mesogranular (MG),

Supergranular (SG).

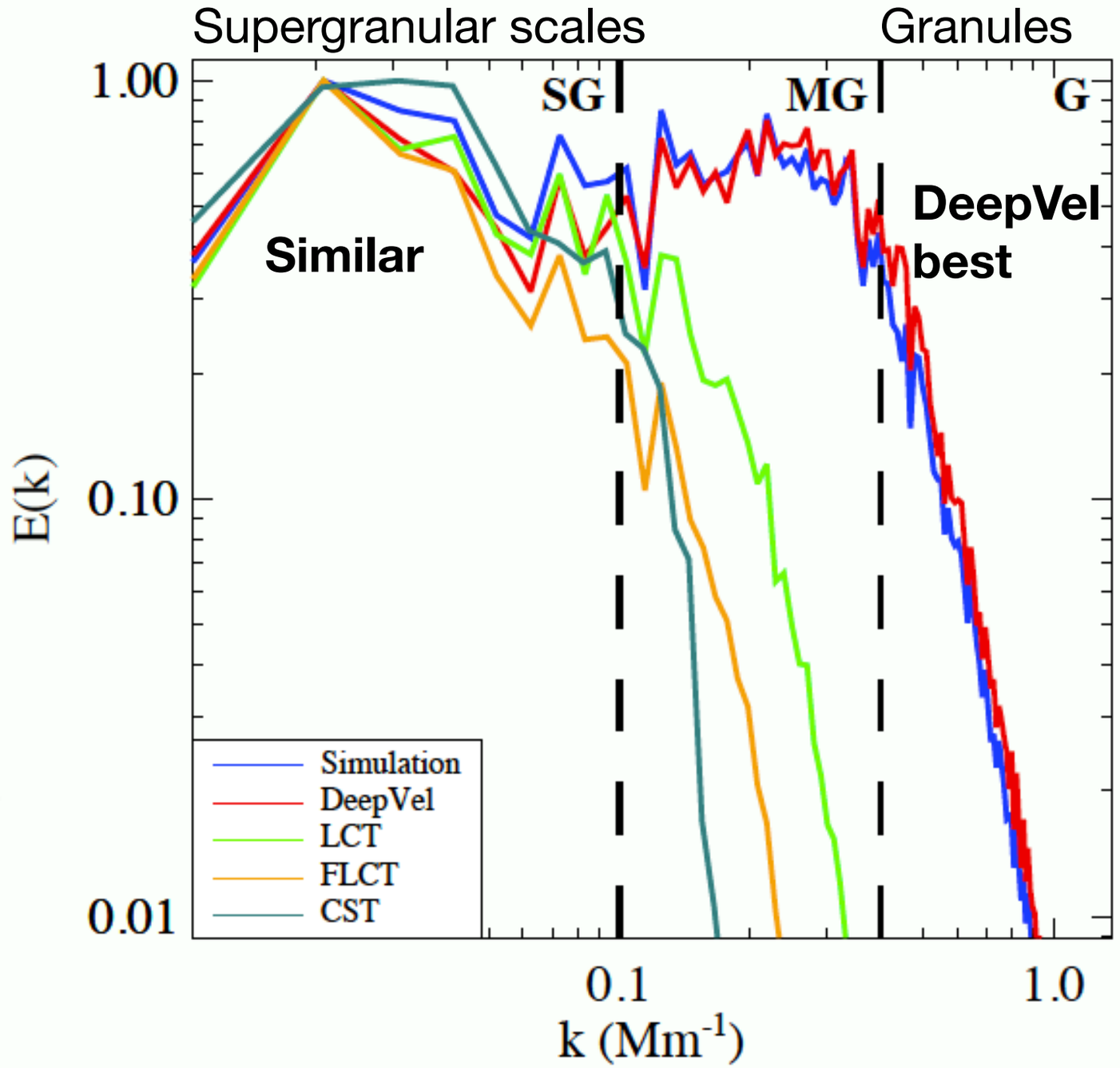

FLCT and DeepVel perform similarly at large spatial scales

DeepVel performs best at smaller scales

(Tremblay *et al.*, 2018)

Some examples of where magnetic fields could be useful using HMI as a example

Quantitative studies based on HMI Low-Cadence (12 min) Vector Magnetograms

- Electric fields & Poynting Fluxes
- Reconnection fluxes

Quantitative studies based on HMI High-Cadence (135s) Vector Magnetograms

- Magnetic imprints
- Lorentz forces
- Electric Currents

Data-driven models

HMI Low-Cadence Vector Data

The Helioseismic and Magnetic Imager (HMI)

- **B** & $\mathbf{V_{dopp}}$ since May 1 2010
- Full disk 24 hrs/day
- dt=12 minutes, ds=360 km

Why low-cadence vector magnetograms?

- Active-regions: v~[0.1-0.3] km/s
- Photospheric magnetic evolution is well-resolved

Hoeksema et. al 2014, Scherrer et al. 2012

Using Vector Magnetograms to Derive Vertical Energy Flux

Vertical magnetic field

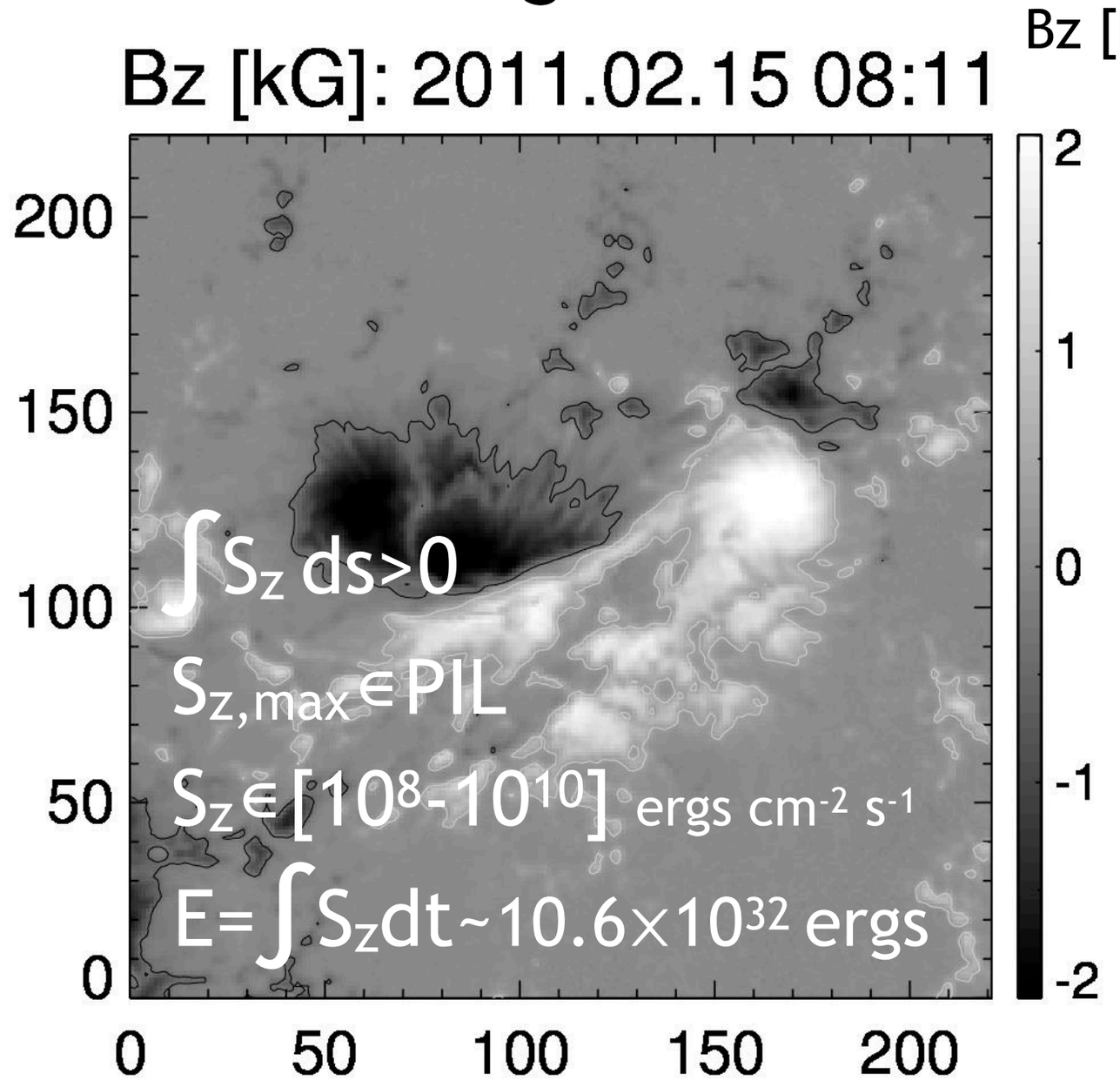

Vertical Poynting flux

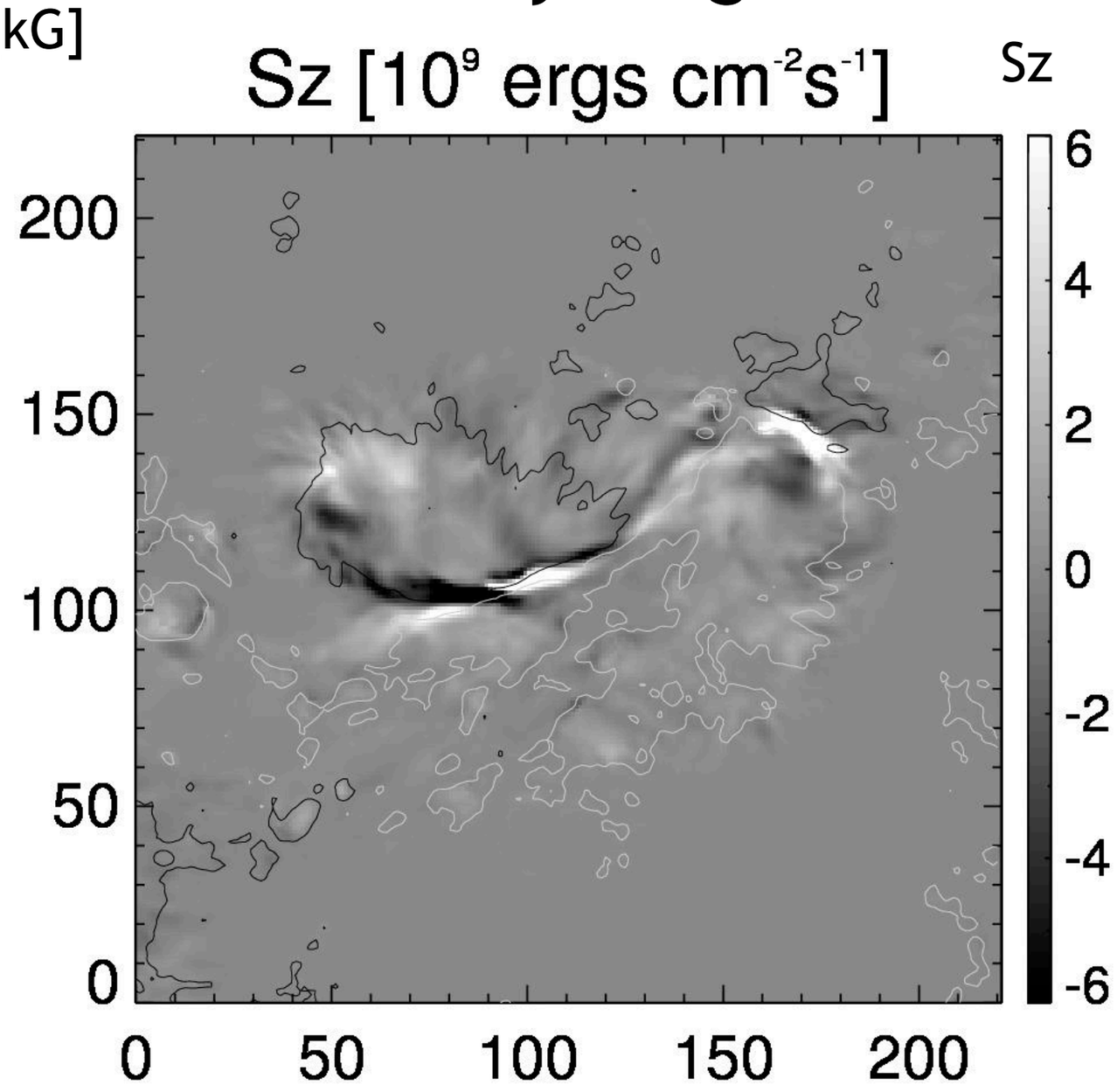

Kazachenko et al. 2015

Using B to Find Properties of Reconnecting Magnetic Fields

Flare ribbons are the footpoints of reconnected field lines!

M6.5 flare, AIA 171

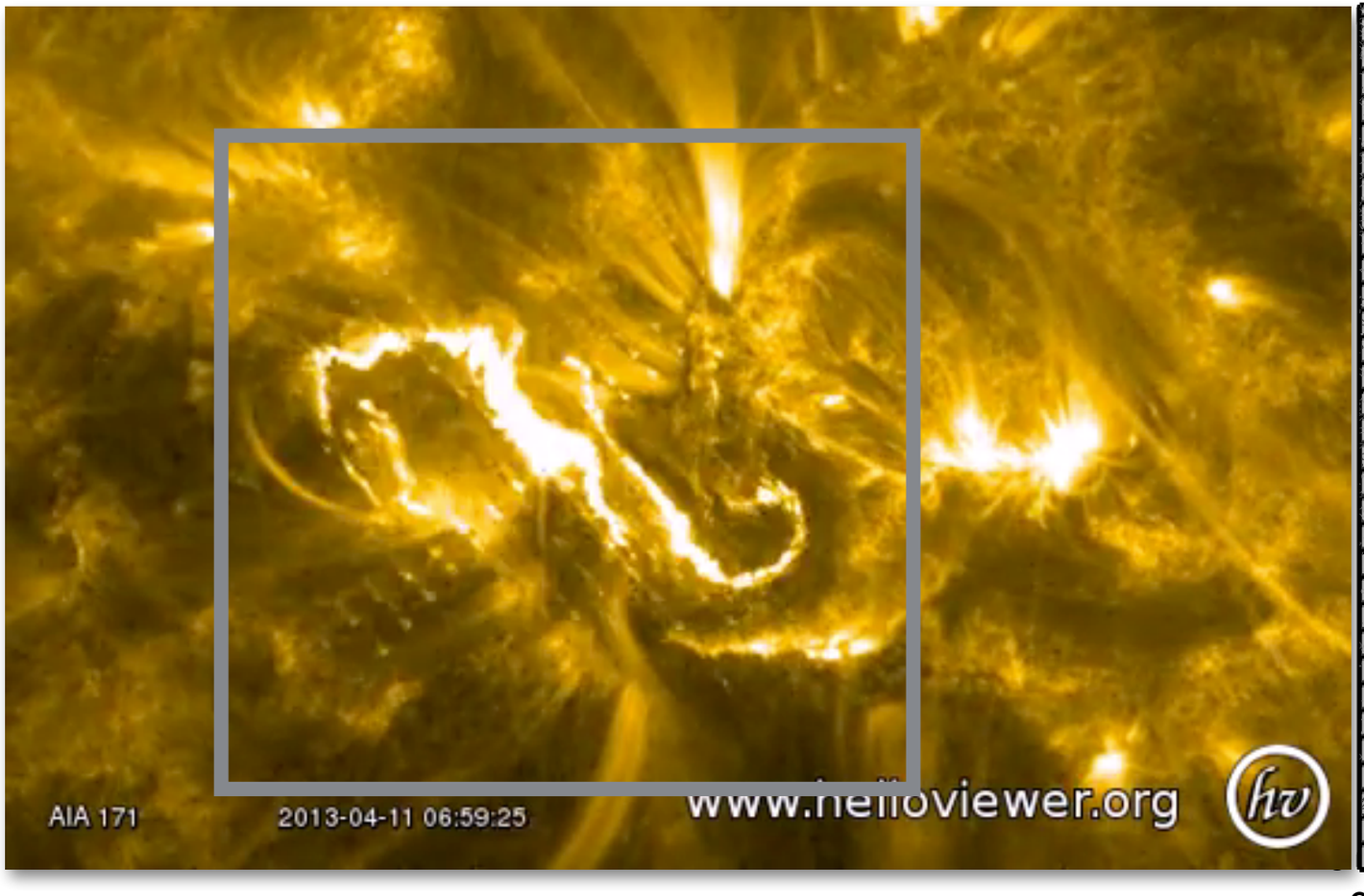

Ribbon evolution over Br contour

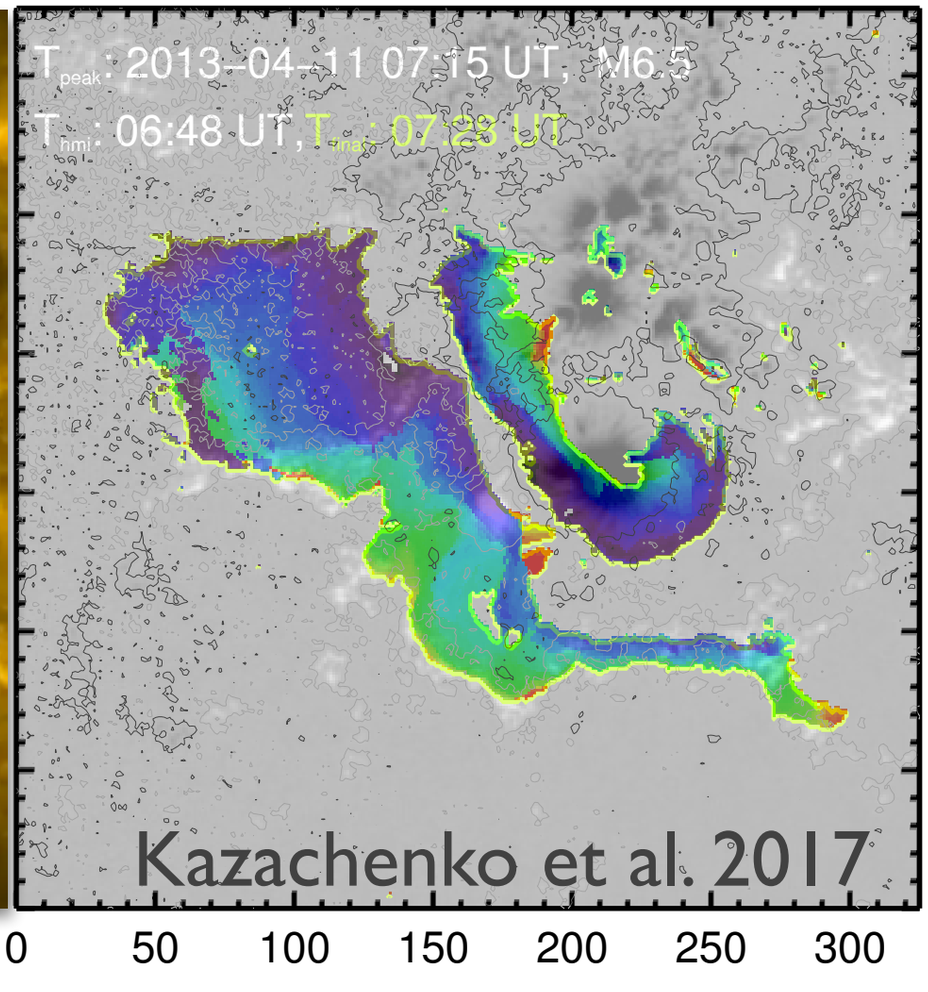

Using B to Find Properties of Reconnecting Magnetic Fields

Flare ribbons are the footpoints of reconnected field lines!

Reconnected Flux $$\Phi_{\text{ribbon}} = \int |B_n| dS_{\text{ribbon}},$$

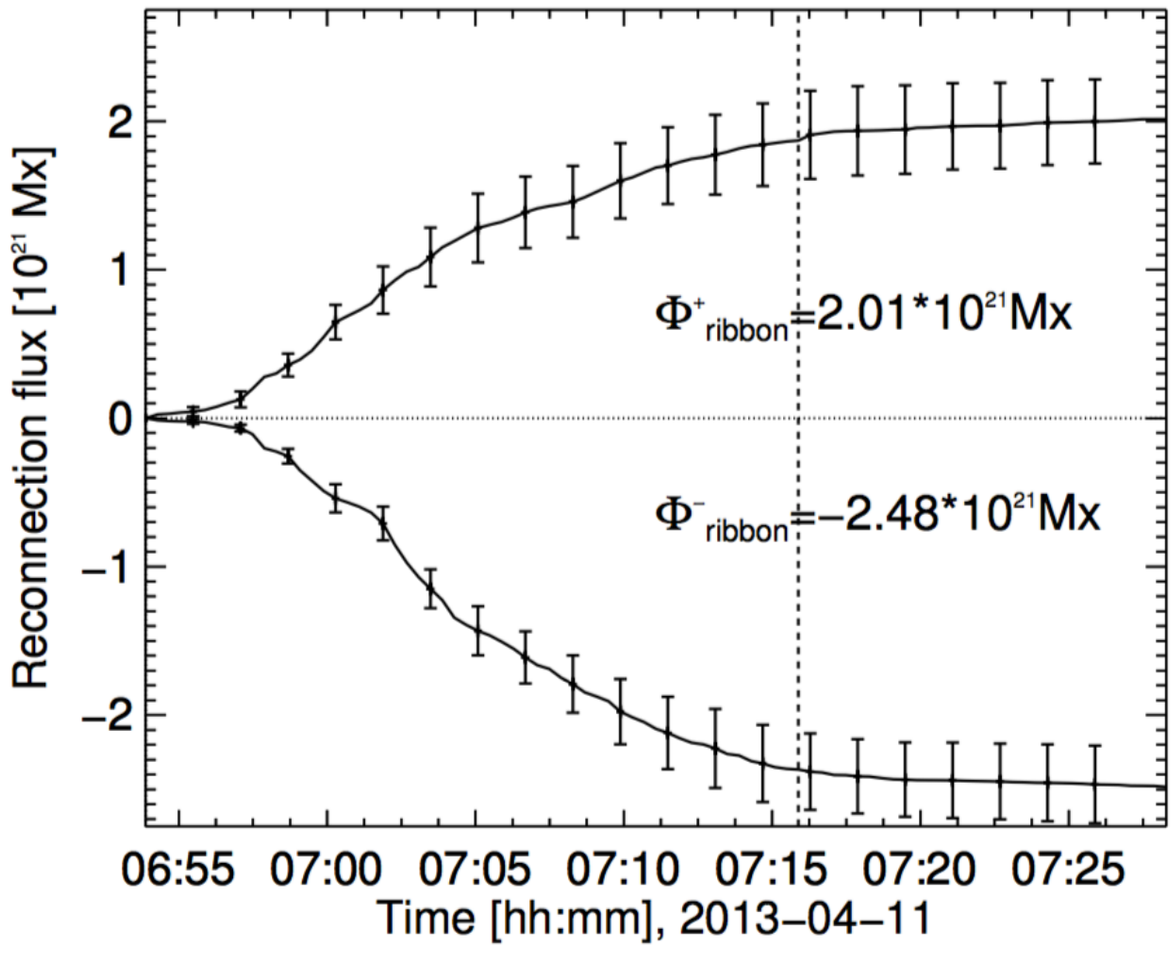

Ribbon evolution over Br contour

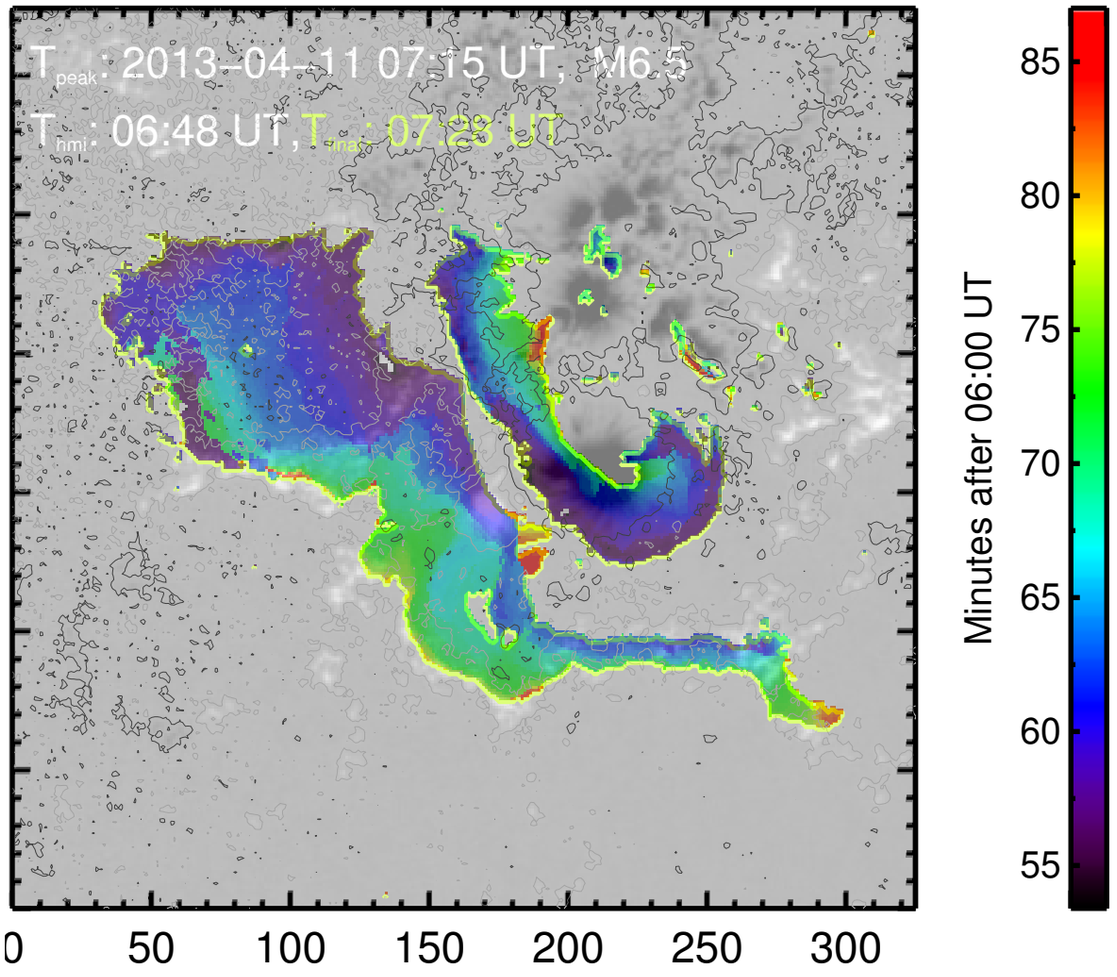

Kazachenko et al. 2017

Properties of Reconnecting Magnetic Fields

RibbonDB: ~3000 solar flares

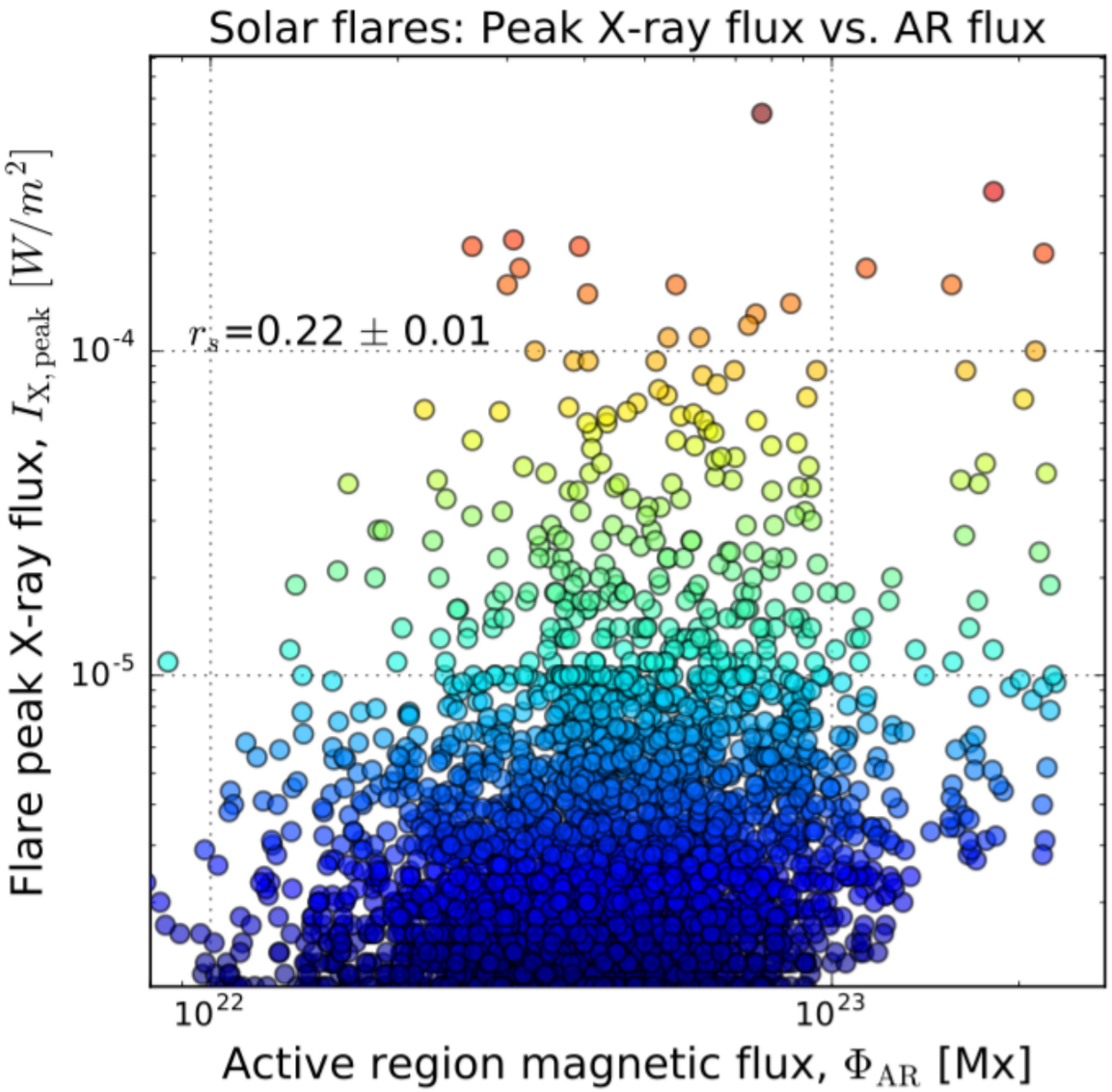

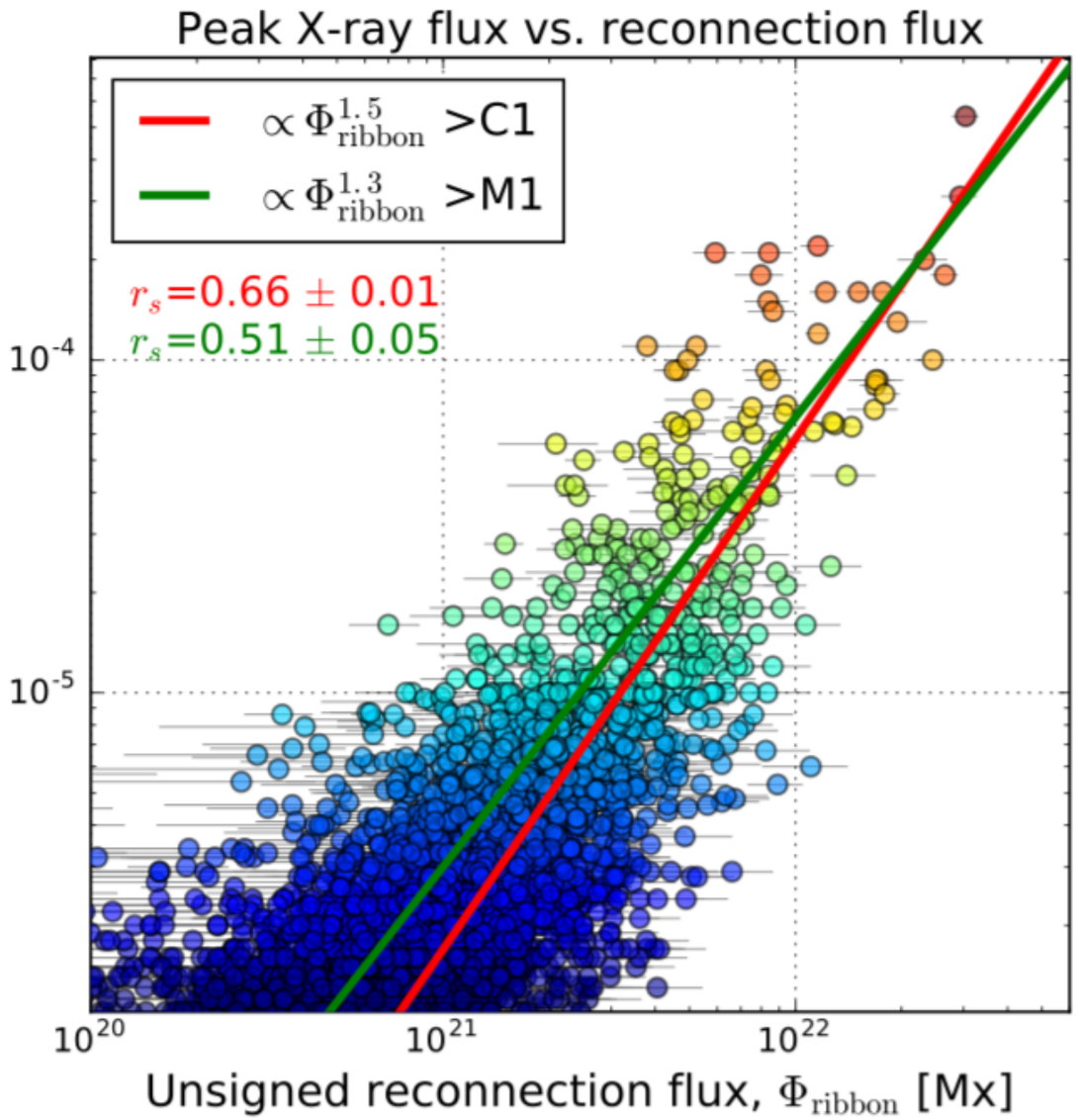

Kazachenko et al. 2017

HMI High-Cadence Vector Data

- dt=135 s (dt=90 s after Apr 2016); ds=360 km;
- Data already available for selective periods (360 h); but could be requested for any time during SDO mission.

Why high-cadence vector magnetograms?

- Some types of rapid photospheric magnetic evolution is under-resolved at 12-min
- **Example**: major eruption; flux emergence

Sun et al., 2017, *ApJ*, **839**, 67

Comparison Between High- and Low-Cadence Vector Data

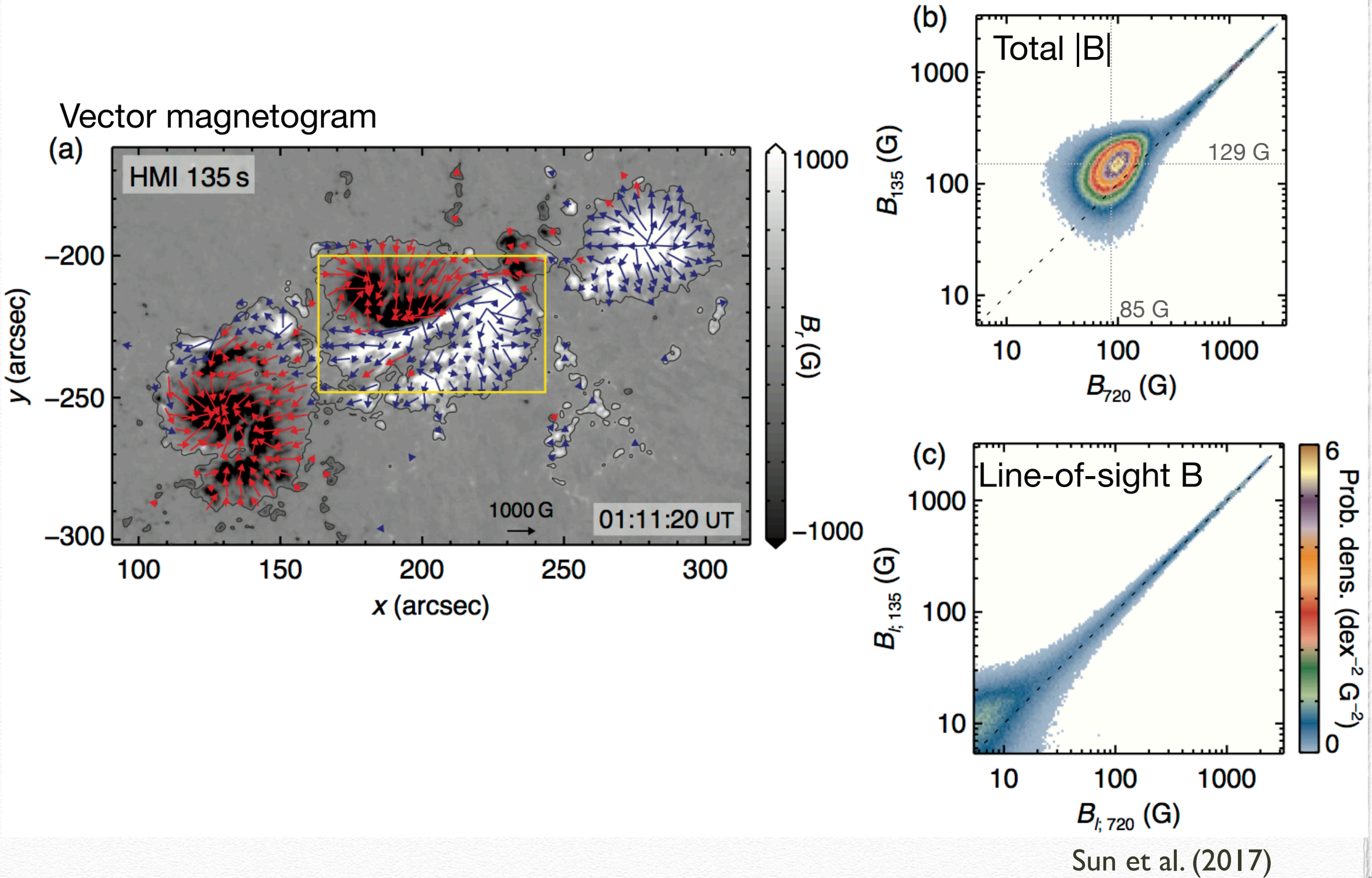

Sun et al. (2017)

Magnetic "Imprint" & "Transient"

During eruption photospheric field changes during minutes

<u>Field changes</u>: → "imprints" (permanent)

→ "transients" (temporary)

<u>Before high-cadence HMI data:</u>

B_{los} observations: good temporal cadence, but no vector

B observations: low temporal cadence

<u>High-cadence HMI data</u>: can clarify ambiguities

Sun et al. (2017)

Magnetic "Imprint" in AR 11158

Differenced **horizontal** B

Differenced **radial** B

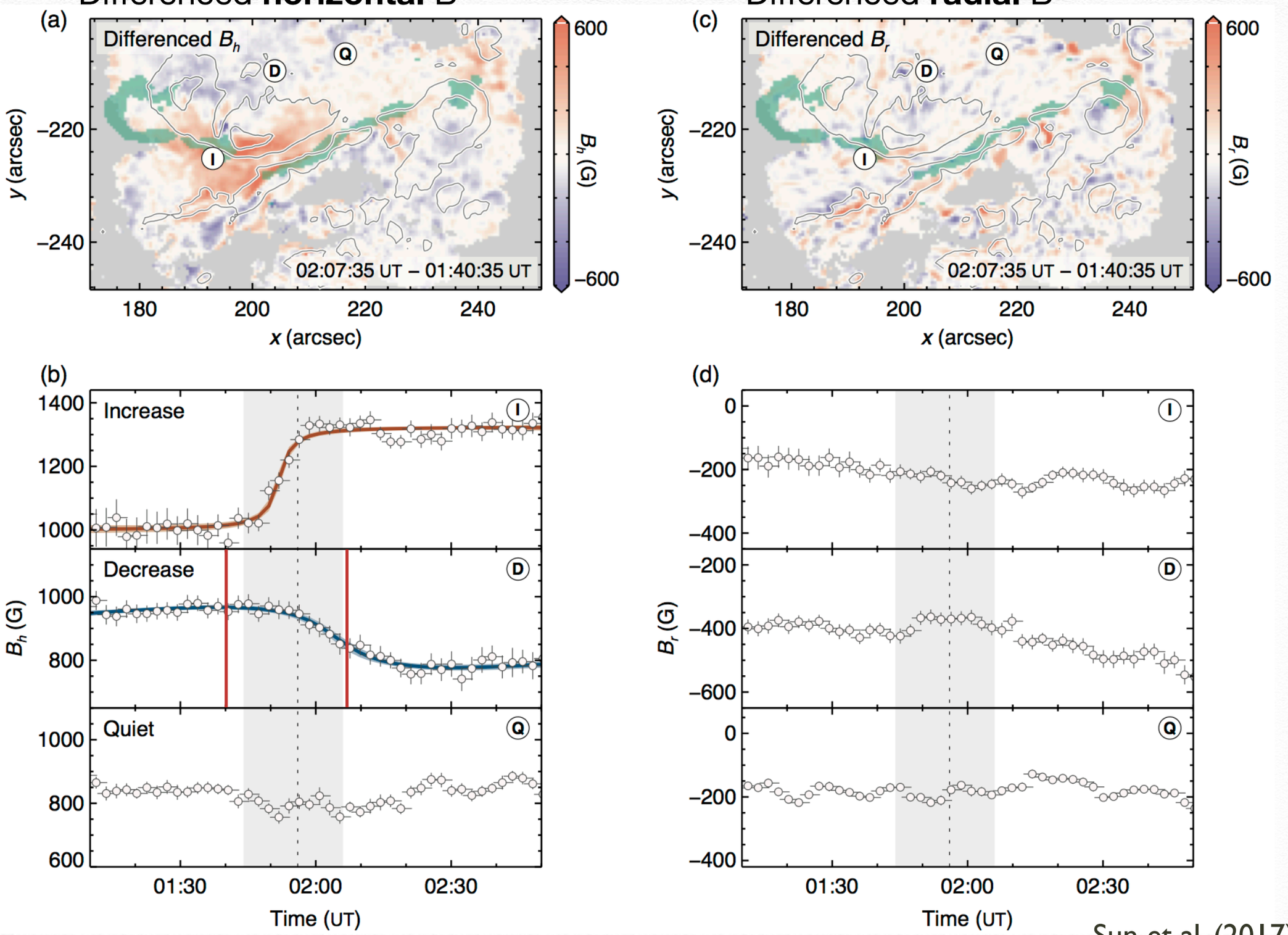

Sun et al. (2017)

Magnetic "Imprint" in AR 11158: Temporal Evolution

Differenced Bh

Sun et al. (2017)

increase

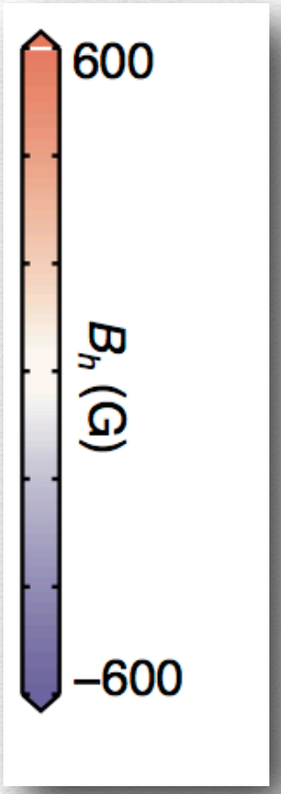

decrease

Lorentz Force Change in AR 11158

$$F_z = \frac{1}{8\pi} \int_{\text{photosph}} (B_h^2 - B_z^2) dA.$$

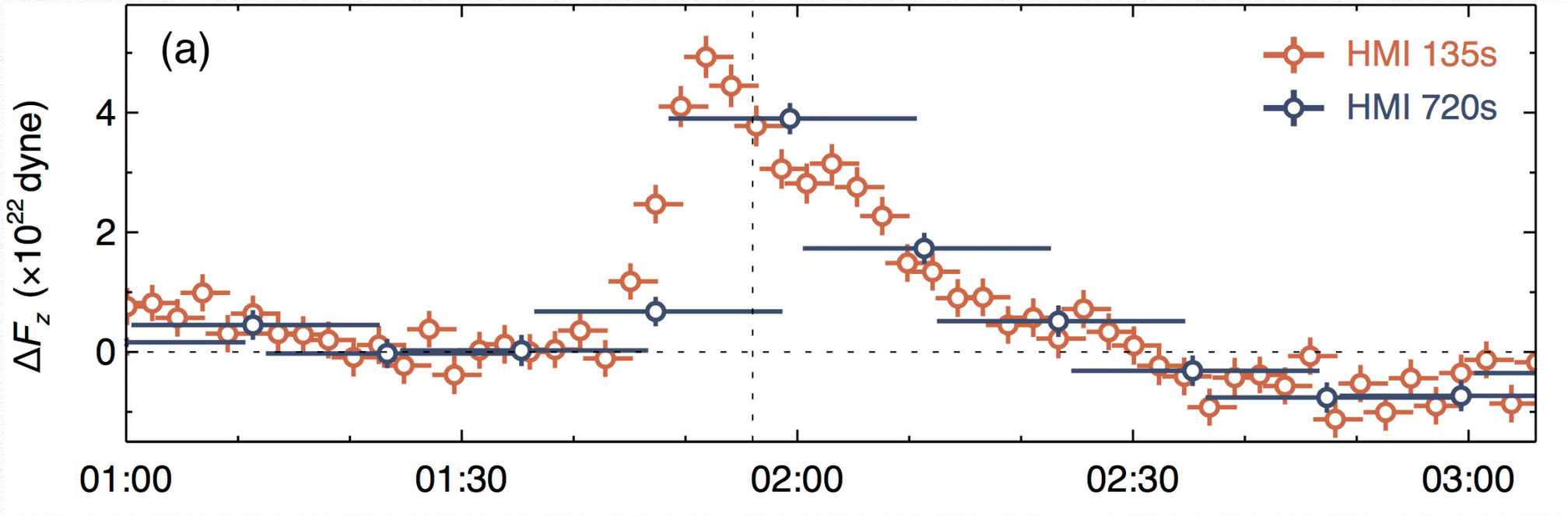

Sun et al. (2017)

Flare Ribbons Vs. Vertical Currents

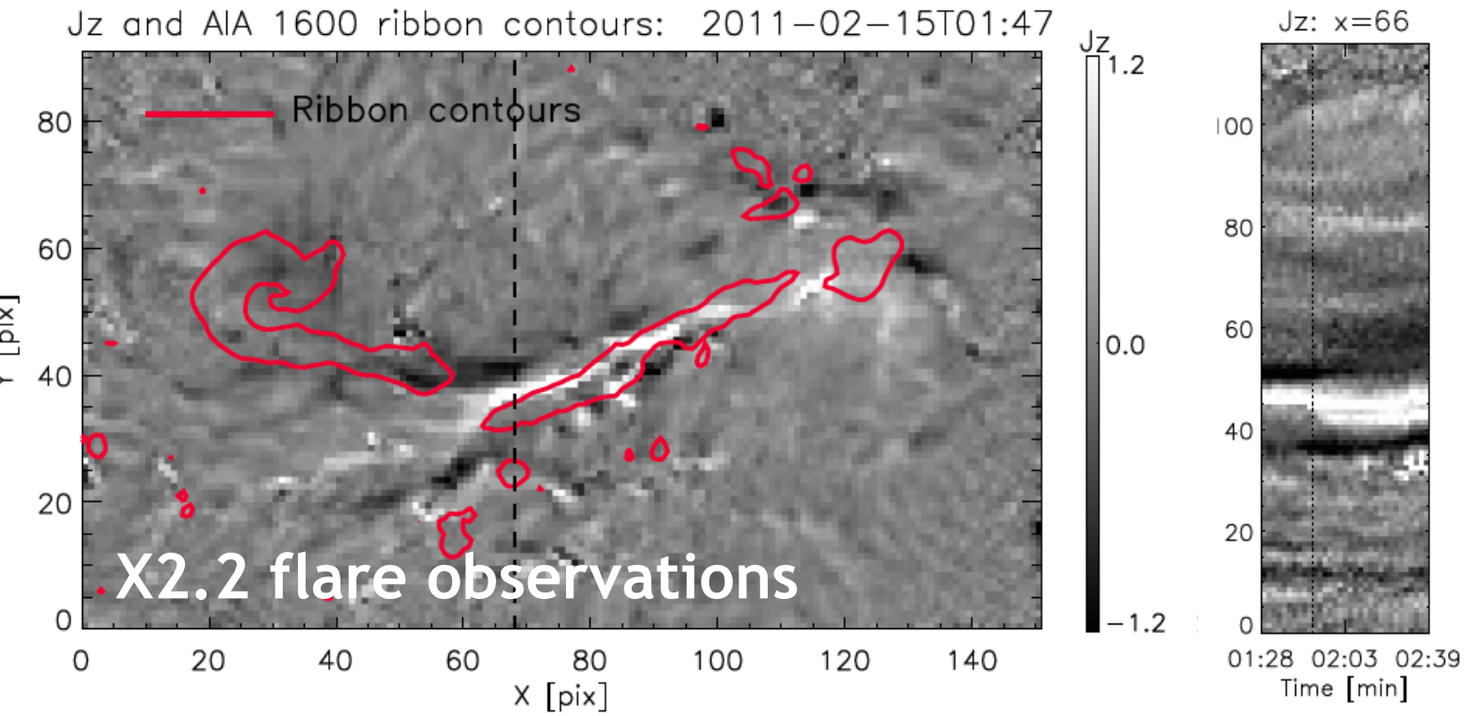

Jz (**Black**) and ribbons (**Red**) spatial (left) and temporal (right) distribution

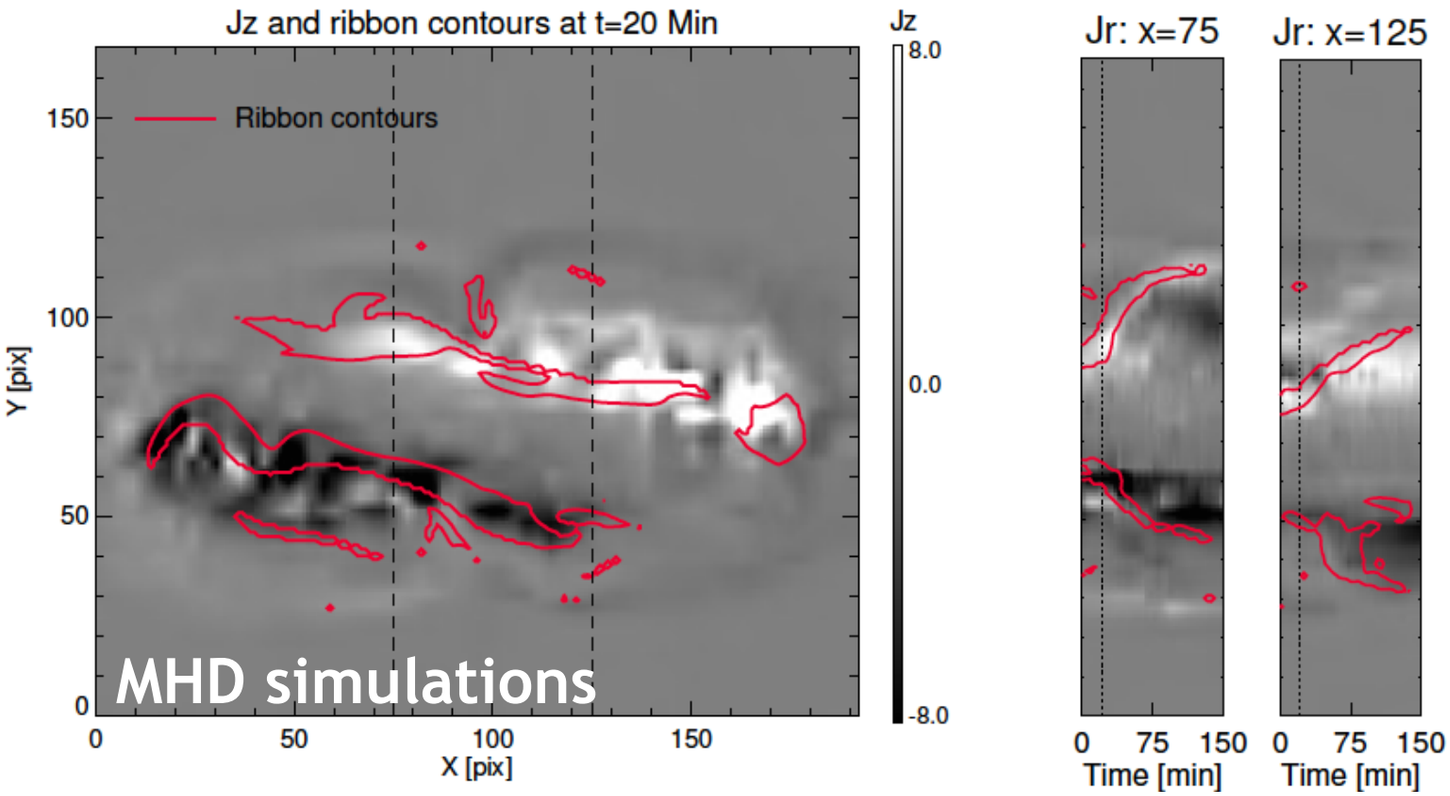

Spatio-temporal correlation between locations of strong Jz and ribbons

Kazachenko & Lynch in prep.

Data-Driven Models: How Are Data-driven Models Affected By a Finite Observation Cadence?

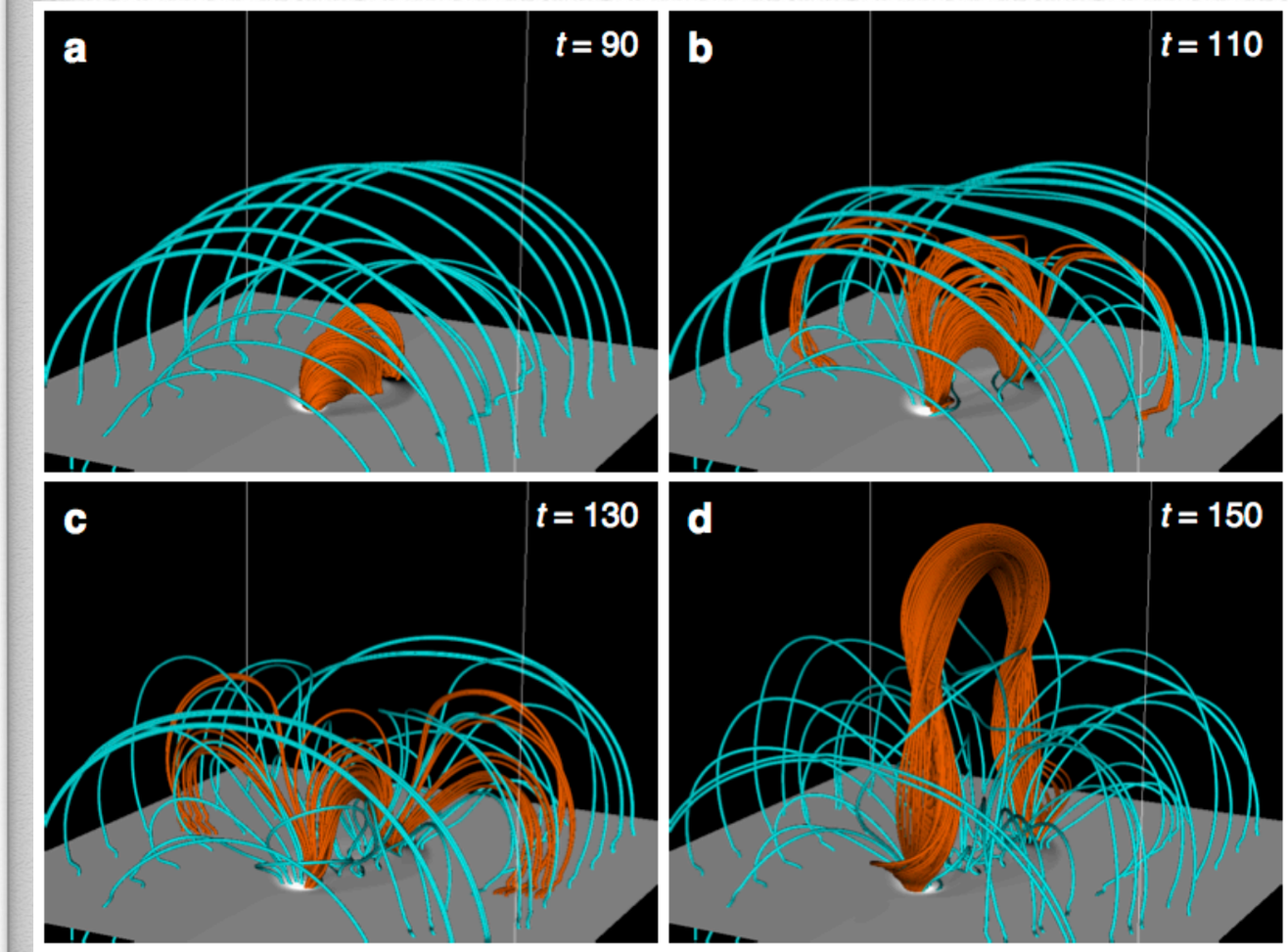

Error in the magnetic free energy as a function of the input-data cadence for a **fast emergence**

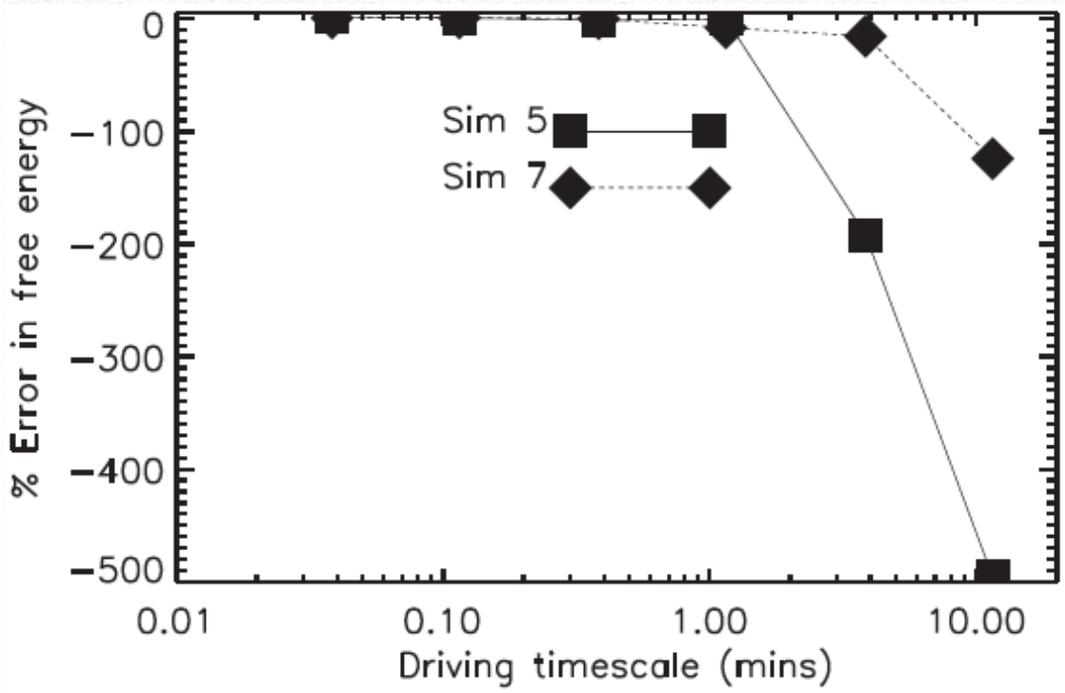

Leake et al. 2014, 2017

Properties From **B**-Observations For Data-Driven Models' Validation

- Magnetic energy (free and potential)
- Magnetic helicity
- Reconnection flux (during eruptions)
- Change in Lorentz force

Conclusions: use of vector magnetic fields

- HMI/SDO: first routine high-quality full disk measurements of the solar vector magnetic field
- Vector magnetic fields allow us to estimate:
    - Electric fields (e.g. DAVE4VM, PDFI, ML methods)
    - Poynting fluxes
    - Electric currents
    - Lorentz forces
    - Magnetic energy & helicity etc.
  - Drive coronal magnetic field models and validate them
  - HMI/SDO: dt=135s vs dt=720s: Temporal cadence is important! With DKIST even better!
- Vector magnetic fields observations are key to quantitative studies of Sun's activity.

Outline for three classes

- Last Thursday: magnetic fields in the photosphere; early methods to find magnetic field flows (velocity, electric fields) from these measurements.

- Today: deriving velocity fields in the solar photosphere using more recent methods: DAVE4VM, PDFI, some ML methods; examples of their application to solar data; examples of other **B**-use.

- Thursday: hands-on activity: applying FLCT to a sequence of HMI/SDO magnetograms to derive horizontal velocities, magnetic fluxes, helicity and energy fluxes.